

## 1 **How much inundation occurs in the Amazon River basin?**

2 Ayan Santos Fleischmann<sup>1,2</sup>, Fabrice Papa<sup>3,4</sup>, Alice Fassoni-Andrade<sup>3,4</sup>, John M. Melack<sup>5</sup>, Sly  
3 Wongchuig<sup>6</sup>, Rodrigo Cauduro Dias de Paiva<sup>2</sup>, Stephen K. Hamilton<sup>7</sup>, Etienne Fluet-Chouinard<sup>8</sup>,  
4 Rafael Barbedo<sup>2</sup>, Filipe Aires<sup>9</sup>, Ahmad Al Bitar<sup>10</sup>, Marie-Paule Bonnet<sup>11</sup>, Michael Coe<sup>12</sup>,  
5 Jefferson Ferreira-Ferreira<sup>1</sup>, Laura Hess<sup>5</sup>, Katherine Jensen<sup>13,14</sup>, Kyle McDonald<sup>13,14</sup>, Alex  
6 Ovando<sup>15</sup>, Edward Park<sup>16</sup>, Marie Parrens<sup>17,18</sup>, Sébastien Pinel<sup>19</sup>, Catherine Prigent<sup>20</sup>, Angélica F.  
7 Resende<sup>21</sup>, Menaka Revel<sup>22</sup>, Ake Rosenqvist<sup>23</sup>, Jessica Rosenqvist<sup>23</sup>, Conrado Rudorff<sup>15</sup>, Thiago  
8 S. F. Silva<sup>24</sup>, Dai Yamazaki<sup>22</sup>, Walter Collischonn<sup>2</sup>

9 <sup>1</sup> Mamirauá Institute for Sustainable Development, Tefé, AM, Brazil

10 <sup>2</sup> Institute of Hydraulic Research, Universidade Federal do Rio Grande do Sul (UFRGS), Porto Alegre, RS, Brazil

11 <sup>3</sup> Laboratoire d'Etudes en Géophysique et Océanographie Spatiales (LEGOS), Université de Toulouse, IRD, CNRS, CNES, USP, Toulouse,  
12 France

13 <sup>4</sup> Institut de Recherche pour le Développement (IRD), Universidade de Brasília (UnB), Institute of Geosciences, Campus Universitário Darcy  
14 Ribeiro, 70910-900, Brasília, Brazil

15 <sup>5</sup> Earth Research Institute, University of California, Santa Barbara

16 <sup>6</sup> Univ. Grenoble Alpes, IRD, CNRS, Grenoble INP, Institut des Géosciences de l'Environnement (IGE, UMR 5001), 38000, Grenoble, France

17 <sup>7</sup> Kellogg Biological Station, Michigan State University, Hickory Corners, MI 49060, USA and Cary Institute of Ecosystem Studies, Millbrook,  
18 NY 12545 USA

19 <sup>8</sup>Department of Earth System Science, Stanford University, Stanford, California, CA

20 <sup>9</sup> Laboratoire d'Etudes du Rayonnement et de la Matière en Astrophysique et Atmosphères, Observatoire de Paris, UMR 8112, Paris, France.

21 <sup>10</sup> Centre d'Etudes Spatiales de la Biosphère (CESBIO), Toulouse University (CNES, CNRS, INRAe, IRD, UPS), Toulouse, France

22 <sup>11</sup> Espace-DEV, Univ Montpellier, Institute of Research for Development, Univ Guyane, Univ Reunion, Montpellier, France

23 <sup>12</sup>Woodwell Climate Research Center, Falmouth, MA

24 <sup>13</sup> Department of Earth and Atmospheric Sciences, City College of New York, City University of New York, New York, NY 10031, USA

25 <sup>14</sup> Department of Earth and Environmental Science, The Graduate Center, City University of New York, New York, NY 10031, USA

- 26 <sup>15</sup> Centro Nacional de Monitoramento de Desastres Naturais (CEMADEN), São José dos Campos, São Paulo, Brazil
- 27 <sup>16</sup> National Institute of Education, Earth Observatory of Singapore and Asian School of the Environment, Nanyang Technological University,  
28 Singapore
- 29 <sup>17</sup> Centre d'Etudes Spatiales de la Biosphère (CESBIO), CNES, Université de Toulouse (UPS), France
- 30 <sup>18</sup> Dynafor, Université de Toulouse, INRAE, INPT, INP-PURPAN, Castanet-Tolosan, France
- 31 <sup>19</sup> CEFREM, University of Perpignan Via Domitia, Perpignan, France
- 32 <sup>20</sup> CNRS, Sorbonne Université, Observatoire de Paris, Université PSL, Lerma, Paris, France
- 33 <sup>21</sup> Universidade de São Paulo, Departamento de Ciências Florestais (ESALQ), Piracicaba, SP, Brazil
- 34 <sup>22</sup> Institute of Industrial Science, The University of Tokyo, Tokyo, Japan.
- 35 <sup>23</sup> solo Earth Observation (soloEO), Tokyo 104-0054, Japan
- 36 <sup>24</sup> Biological and Environmental Sciences, Faculty of Natural Sciences, University of Stirling, Stirling, UK Fk9 4LA.
- 37
- 38 Corresponding author: Ayan Santos Fleischmann ([ayan.fleischmann@gmail.com](mailto:ayan.fleischmann@gmail.com))
- 39

## 40 **Abstract**

41 The Amazon River basin harbors some of the world's largest wetland complexes, which are of major  
42 importance for biodiversity, the water cycle and climate, and human activities. Accurate estimates of  
43 inundation extent and its variations across spatial and temporal scales are therefore fundamental to  
44 understand and manage the basin's resources. More than fifty inundation estimates have been generated for  
45 this region, yet major differences exist among the datasets, and a comprehensive assessment of them is  
46 lacking. Here we present an intercomparison of 29 inundation datasets for the Amazon basin, based on  
47 remote sensing only, hydrological modeling, or multi-source datasets, with 18 covering the lowland  
48 Amazon basin (elevation < 500 m, which includes most Amazon wetlands), and 11 covering individual  
49 wetland complexes (subregional datasets). Spatial resolutions range from 12.5 m to 25 km, and temporal  
50 resolution from static to monthly, spanning up to a few decades. Overall, 31% of the lowland basin is

51 estimated as subject to inundation by at least one dataset. The long-term maximum inundated area across  
52 the lowland basin is estimated at  $599,700 \pm 81,800$  km<sup>2</sup> if considering the three higher quality SAR-based  
53 datasets, and  $490,300 \pm 204,800$  km<sup>2</sup> if considering all 18 datasets. However, even the highest resolution  
54 SAR-based dataset underestimates the maximum values for individual wetland complexes, suggesting a  
55 basin-scale underestimation of ~10%. The minimum inundation extent shows greater disagreements among  
56 datasets than the maximum extent:  $139,300 \pm 127,800$  km<sup>2</sup> for SAR-based ones and  $112,392 \pm 79,300$  km<sup>2</sup>  
57 for all datasets. Discrepancies arise from differences among sensors, time periods, dates of acquisition,  
58 spatial resolution, and data processing algorithms. The median total area subject to inundation in medium  
59 to large river floodplains (drainage area > 1,000 km<sup>2</sup>) is 323,700 km<sup>2</sup>. The highest spatial agreement is  
60 observed for floodplains dominated by open water such as along the lower Amazon River, whereas  
61 intermediate agreement is found along major vegetated floodplains fringing larger rivers (e.g., Amazon  
62 mainstem floodplain). Especially large disagreements exist among estimates for interfluvial wetlands  
63 (Llanos de Moxos, Pacaya-Samiria, Negro, Roraima), where inundation tends to be shallower and more  
64 variable in time. Our data intercomparison helps identify the current major knowledge gaps regarding  
65 inundation mapping in the Amazon and their implications for multiple applications. In the context of  
66 forthcoming hydrology-oriented satellite missions, we make recommendations for future developments of  
67 inundation estimates in the Amazon and present a WebGIS application ([https://amazon-](https://amazon-inundation.herokuapp.com/)  
68 [inundation.herokuapp.com/](https://amazon-inundation.herokuapp.com/)) we developed to provide user-friendly visualization and data acquisition of  
69 current Amazon inundation datasets.

70 **Key words:** flooding, surface water, floodplains, interfluvial wetlands

71

## 72 **1. Introduction**

73 Aquatic ecosystems cover extensive areas of the Amazon basin, and are associated with temporally  
74 and spatially dynamic habitats such as floodable forests, savannas, grasslands, large and small  
75 rivers, and lakes (Hess et al., 2015; Junk et al., 2011; Melack and Coe, 2021; Reis et al., 2019a).  
76 These systems, hereafter called wetlands, support plants and animals that are adapted to the flood  
77 pulse (Junk et al., 1989), play key roles in regional and global biogeochemical cycles, especially  
78 the carbon cycle (Richey et al 1990; Dunne et al., 1998; Abril et al., 2014; Melack et al., 2004;  
79 Pangala et al., 2017; Martínez-Espinosa et al., 2020), and regulate the riverine transport of  
80 dissolved and particulate material, including sediment and organic matter (Armijos et al., 2020;  
81 Fassoni-Andrade and Paiva, 2019; Melack and Forsberg, 2001; Ward et al., 2017). Additionally,  
82 human settlements along Amazon wetlands (Blatrix et al., 2018; Denevan, 1996) benefit from  
83 ecosystem services, including food provision from native plants and animals as well as crop and  
84 livestock production (Coomes et al., 2016; Jardim et al., 2020).

85 Many of the wetlands of the Amazon basin are considered floodplain because they are subject to  
86 seasonal or periodic inundation by river overflow (i.e., the flood pulse; Junk et al., 1989). The  
87 region also hosts large interfluvial wetlands, which unlike fringing floodplains along large rivers,  
88 are flooded mainly by local rainfall and runoff and characterized by shallow water (Belger et al.,  
89 2011; Bourrel et al., 2009; Junk et al., 2011). Water sources, inundation patterns, and  
90 geomorphology interact to determine the structure and function of these biodiverse ecosystems  
91 (Junk et al., 2011; Latrubesse, 2012; Park and Latrubesse, 2017).

92 The extent of inundated land (also called flooded land or surface water extent), and its temporal  
93 variation, are core variables to understand wetland processes and are of interest for multiple  
94 scientific disciplines, including ecology (Silva et al., 2013; Hawes et al., 2012; Luize et al. 2015),  
95 land-atmosphere interactions (Prigent et al., 2011; Santos et al., 2019; Taylor et al., 2018), carbon

96 cycling and greenhouse gas emissions (Guilhen et al., 2020; Melack et al., 2004; Richey et al.,  
97 2002), and natural hazard management (Restrepo et al., 2020; Trigg et al., 2016). The Amazon  
98 basin has been a focus for remote sensing developments and applications in hydrology (Fassoni-  
99 Andrade et al., 2021), especially for inundation estimation, given the basin's large scale and global  
100 environmental relevance, relatively pristine landscape, and technical challenges posed by  
101 persistent cloud cover (Asner, 2001) and dense vegetation. This resulted in the development of  
102 more than 50 inundation maps and datasets for this region in recent decades. Tables 1 (datasets  
103 used in this study) and S1 (datasets not used due to redundancy or unavailability) summarize most  
104 of the datasets developed for mapping inundation in the Amazon basin.

105 Digital wetland maps were first produced for the Amazon basin by Matthews and Fung (1987)  
106 from aeronautical charts. Optical remote sensing systems in the visible or thermal spectral range,  
107 such as Landsat, are of limited value for most Amazon wetlands, since inundation under persistent  
108 cloud cover and dense vegetation canopies can be difficult to detect. Because of this, microwave  
109 systems have been employed. Large-scale inundation mapping was pioneered in the region through  
110 analysis of Scanning Multi-channel Microwave Radiometer (SMMR) and Special Sensor  
111 Microwave/Imager (SSM/I) passive microwave observations, which provided all-weather  
112 capability and sensitivity to inundation even in the presence of partial vegetative cover (Hamilton  
113 et al., 2002; Prigent et al., 2001; Sippel et al., 1998). Meanwhile, research demonstrated the all-  
114 weather capability and superior spatial resolution of synthetic aperture radar (SAR) systems. L-  
115 band SAR that can penetrate forest canopies and reveal underlying water through the "double  
116 bounce" effect was shown to be promising for mapping inundation in the Amazon (Hess et al.,  
117 2003). More specifically, the high-resolution, dual-season classification of the Japanese Earth  
118 Resources Satellite-1 (JERS-1) L-band SAR data for the entire lowland Amazon basin by Hess et

119 al. (2015), validated with airborne videography images, has been used as a benchmark for the  
120 inundation extent of Amazon wetlands. Since these initial studies, and with the availability of other  
121 imagery (e.g., Advanced Land Observing Satellite (ALOS) 1 and 2 missions), the remote sensing  
122 community seeking to map and characterize inundation employed various combinations of active  
123 and passive microwave data to benefit from the higher spatial resolution of the former and the  
124 higher temporal resolution of the latter (Aires et al., 2013; Jensen and McDonald, 2019; Papa et  
125 al., 2010; Parrens et al., 2019, 2017; Prigent et al., 2007, 2020; Schroeder et al., 2015).

126 Besides the basin-scale mappings (which, in our context, refer to both basin-scale datasets and  
127 those that cover only the lowland areas below 500 m.a.s.l. elevation) of annual maximum and  
128 minimum inundation (Chapman et al., 2015; Hess et al., 2015; Rosenqvist et al., 2020), dynamic  
129 datasets with high spatial and temporal resolution are mainly based on satellite passive microwave  
130 observations of coarse spatial resolution (Global Inundation Extent Multi-Satellite – GIEMS),  
131 Surface Water Microwave Product Series (SWAMPS), Surface Water Fraction (SWAF), Wetland  
132 Area and Dynamics for Methane Modeling (WAD2M) datasets; see Table 1), which can be  
133 downscaled using ancillary data (Aires et al., 2017, 2013; Parrens et al., 2019). Basin-scale,  
134 dynamic inundation estimates based on the ALOS satellite are limited given its low temporal  
135 resolution (repeat cycle of 46 days). Thus, some studies have analyzed time series of ALOS-  
136 Phased Array L-band Synthetic Aperture Radar (PALSAR) (Arnesen et al., 2013; Ferreira-Ferreira  
137 et al., 2015) and ALOS-2 PALSAR-2 backscatter retrievals (Jensen et al., 2018) for subsets of  
138 Amazon wetlands. However, with a few exceptions using subregional datasets (Arnesen et al.,  
139 2013; Ferreira-Ferreira et al., 2015; Hess et al., 2003; Jensen et al., 2018; Resende et al., 2019), in  
140 situ validation of the basin-scale estimates has seldom been performed, given the remoteness of

141 much of the Amazon basin and the often dense forest cover, which hampers airborne monitoring  
142 of below-canopy inundation.

143 Complementary to the remotely sensed datasets, process-based hydrological models estimating  
144 variables such as river discharge and flood extent have been developed and assessed from basin to  
145 local scales in the major rivers of the basin (Beighley et al., 2009; Coe et al., 2008; Getirana et al.,  
146 2017, 2012; Hoch et al., 2017; Luo et al., 2017; Miguez-Macho and Fan, 2012; Paiva et al., 2013;  
147 Yamazaki et al., 2011), thanks to the advent of new computational and modeling capabilities.  
148 Local-scale hydraulic models with coarse (Trigg et al., 2009; Wilson et al., 2007; Fleischmann et  
149 al., 2020) and detailed input data (Ji et al., 2019; Pinel et al., 2019; Rudorff et al., 2014; Fassoni-  
150 Andrade, 2020) have further developed model capabilities for mapping inundation dynamics,  
151 especially for the floodplains fringing the Amazon mainstem. These models complement satellite-  
152 based flood mapping due to their higher temporal and spatial resolution, and capability to estimate  
153 long-term time series, for both past and future (e.g., due to climate change) scenarios. The  
154 understanding of their uncertainties can lead to optimal data fusion with satellite-based estimates,  
155 such as considering multiple constraints within the water cycle representation (Pellet et al., 2021).

156 Among these numerous inundation datasets for the Amazon basin (Tables 1 and S1), divergences  
157 can be substantial due to the differences in sensor systems, timing, and data processing algorithms  
158 (Aires et al., 2018; Fleischmann et al., 2020; Parrens et al., 2019; Pham-Duc et al., 2017;  
159 Rosenqvist et al., 2020), and a comprehensive assessment of inundation estimates for the Amazon  
160 is lacking. The need to compare different hydrological datasets for the Amazon has been recently  
161 highlighted in the context of river discharge (Towner et al., 2019), precipitation (Wongchuig et al.,  
162 2017; Zubieta et al., 2019) and evapotranspiration (Paca et al., 2019; Wu et al., 2020). Meanwhile,  
163 rapid environmental changes in the basin underscore the urgency for a better understanding of

164 Amazon water resources (Fassoni-Andrade et al., 2021), for which management and planning can  
165 be hindered by the discrepancies among datasets. These questions regarding current data  
166 limitations in the largest basin in the world are also timely in anticipation of forthcoming  
167 hydrological satellite missions such as Surface Water and Ocean Topography (SWOT) and NASA-  
168 ISRO SAR (NISAR).

169 To better understand and quantify the state of understanding of inundation patterns in the Amazon  
170 wetlands, we address the following questions: 1) How much Amazon land area is subject to  
171 seasonal or permanent flooding, and how accurate are the estimates? 2) Which areas are in  
172 particular disagreement and thus deserve further attention? 3) How do basin-scale estimates with  
173 coarser resolution and less calibrated classification methods differ from those for individual  
174 wetland complexes, with independent validation? 4) How do the various inundation estimation  
175 approaches (optical imagery, SAR, passive microwave, hydrologic models) differ in terms of  
176 inundation mapping and for different wetland types (e.g., floodplains and interfluvial areas)? In  
177 order to answer these questions, we gathered 29 inundation datasets for the Amazon basin,  
178 spanning a wide range of spatial (12.5 m to 25 km) and temporal (static, dual-season, monthly,  
179 daily) resolutions, and coverages from the whole basin to individual wetland complexes (Table 1),  
180 into a framework that provides a comprehensive assessment of current knowledge of Amazon  
181 inundation.

182

183 Table 1. List of 29 studies that mapped inundation over areas ranging from the entire Amazon basin to individual  
184 wetland complexes. These data sources were selected based on data availability and relevance for this intercomparison.  
185 In the case of hydrological models, time resolutions are the values assessed or provided by the models, which can be  
186 provided at finer time resolution if necessary, since many of them compute flood maps at daily or sub-daily time steps



187 and report time-integrated results. The column “Data type” refers to: OS: optical sensor; SAR: synthetic aperture  
 188 radar; HM: hydrological model; HR: multiple datasets at high resolution; CR: multiple datasets at coarse resolution.  
 189 The column “Type of inundation estimated” has three classes: “All”, meaning both open water and vegetated wetlands,  
 190 “Open water”, and “Wetland only (no open water)”.

Data type	Dataset name and main mission/ model associated (if applicable)	Spatial resolution	Temporal resolution	Time period	Region	Type of inundation estimated	Reference
CR	GIEMS-2	25 km	Monthly	1992-2015	Basin	All	Prigent et al., 2020
CR	SWAMPS	25 km	Monthly	1992-2020	Basin	All	Jensen and McDonald, 2019
CR	WAD2M	25 km	Monthly	2000-2018	Basin	Wetland only (no open water)	Zhang et al., 2020
HR	GIEMS-D3	90 m	Monthly	1993-2007	Basin	All	Aires et al., 2017
HR	CIFOR	232 m	Static (max inundation)	1950-2000	Basin	All	Gumbrecht et al., 2017
HR	ESA-CCI	300 m	Annual	1992-2015	Basin	All	Bontemps et al., 2013
HR	GIEMS-D15	500 m	Monthly climatology	1993-2004	Basin	All	Fluet-Chouinard et al., 2015
HR	GLWD	1 km	Static	1992-2004	Basin	All	Lehner and Döll, 2004

HR	SWAF-HR / SMOS mission	1 km	Weekly to monthly	2010-2020	Basin	All	Parrens et al., 2019
HM	THMB model	5-min	Monthly	1961-2010	Basin	All	Coe et al., 2008
HM	CaMa-Flood model	500 m	Monthly	1980-2014	Basin	All	Yamazaki et al., 2011
HM	MGB model	500 m	Monthly	1980-2015	Basin	All	Siqueira et al., 2018
HM	Bonnet model	180 m	Monthly	2006-2019	Janauacá	All	Bonnet et al., 2017
HM	TELEMAC-2D model	30 m	Monthly	2006-2015	Janauacá	All	Pinel et al., 2019
HM	LISFLOOD-FP model	90 m	Monthly	1994-2015	Curuai	All	Rudorff et al., 2014
OS	G3WBM / Landsat mission	30 m	Static (open water areas)	1990-2010	Basin	Open water	Yamazaki et al., 2015
OS	GLAD / Landsat mission	30 m	Annual and monthly climatology	1999-2018	Basin	Open water	Pickens et al., 2020
OS	GSWO / Landsat mission	30 m	Monthly (cloud cover may occur)	1984-2019	Basin	Open water	Pekel et al., 2016
OS	Ovando / MODIS mission	500 m	8 days	2001-2014	Llanos de Moxos	Open water	Ovando et al., 2016
OS	Park / MODIS mission	230 m	Monthly climatology	2000-2015	Amazon River down-	Open water	Park and Latrubesse, 2019

					stream of Manaus		
SAR	Hess / JERS-1 mission	90 m	Max. and min. annual inundation (dual season)	1995- 1996	Basin (lowlands)	All	Hess et al., 2003, 2015
SAR	Chapman / ALOS- PALSAR mission	90 m	Monthly	2006- 2011	Basin	All	Chapman et al., 2015
SAR	Rosenqvist / ALOS-2 PALSAR- 2	50 m	Max. and min. annual inundation (dual season)	2014- 2017	Basin	All	Rosenqvist et al., 2020
SAR	Jensen / ALOS-2 PALSAR-2 mission	50 m	Irregular (26 images)	2014- 2018	Pacaya- Samiria	All	Jensen et al., 2018
SAR	Arnesen / ALOS- PALSAR mission	90 m	Irregular (12 images)	2006- 2010	Curuai	All	Arnesen et al., 2013
SAR	Ferreira-Ferreira / ALOS-PALSAR mission	12.5 m	Flood frequency only	2007- 2010	Mamirauá	All	Ferreira-Ferreira et al., 2015
SAR	Ovando-2 / ALOS- PALSAR mission	100 m	Irregular (6 images)	2006- 2010	Llanos de Moxos	All	Ovando et al., 2016
SAR	Pinel-2 / ALOS- PALSAR mission	30 m	Irregular (16 images)	2007- 2011	Janauacá	All	Pinel et al., 2019
SAR	Resende / ALOS- PALSAR mission	25 m	Static (max inundation)	2006- 2011	Uatumã	All	Resende et al., 2019

191

192

## 193 **2. Methodology**

### 194 **2.1 Study area**

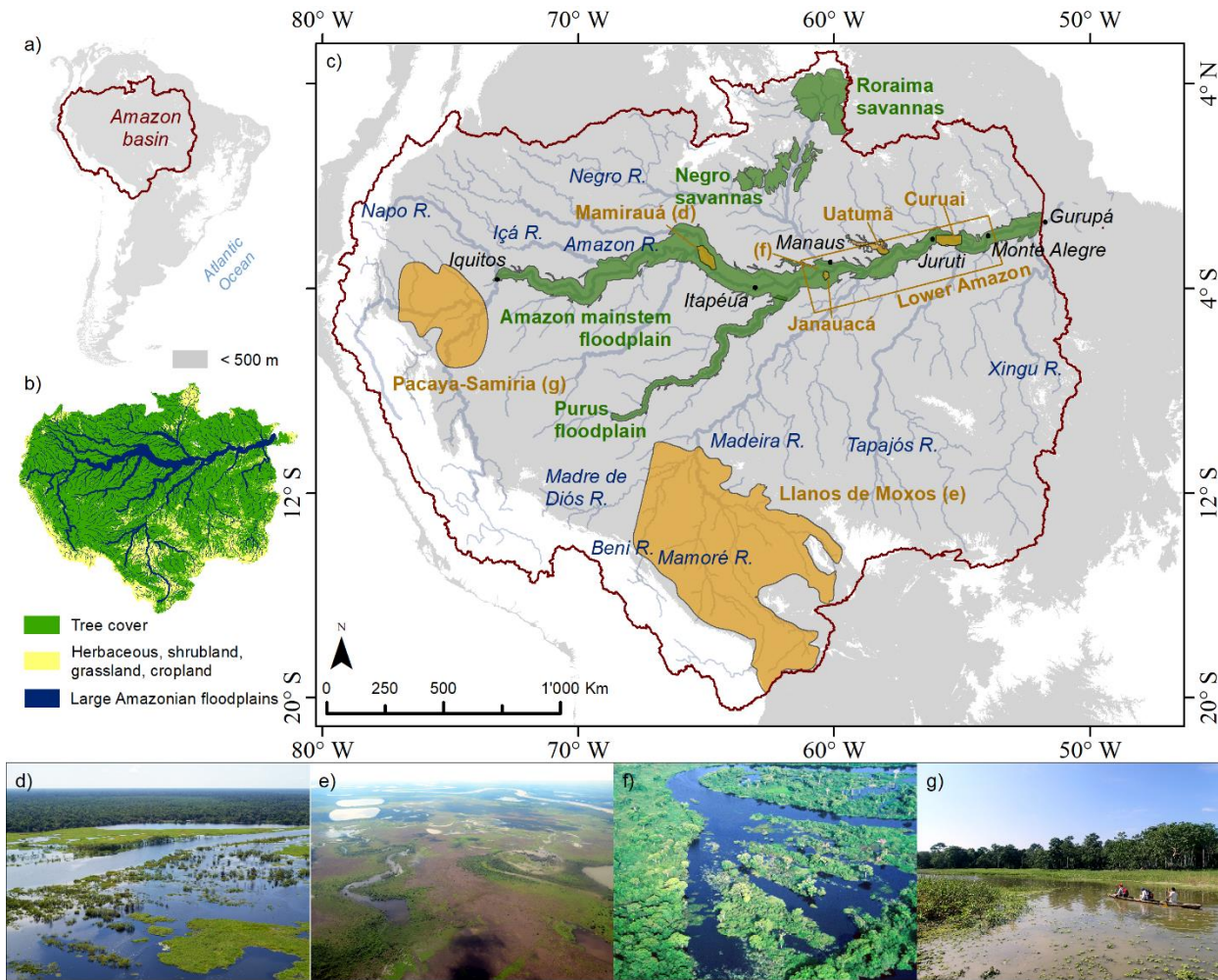
195 The Amazon basin spans around 6 million km<sup>2</sup> in nine South American countries (Figure 1), with  
196 high annual rainfall ( $\sim 2,200$  mm year<sup>-1</sup>), and the Amazon River discharge makes a major  
197 contribution to global freshwater and sediment exports to the ocean (Fassoni-Andrade et al., 2021).  
198 We delineated the catchment area upstream from Gurupá city, within the tidal river  $\sim 390$  km from  
199 the ocean; hence not including the Tocantins-Araguaia basin and parts of the Amazon estuary and  
200 Marajó Island. We selected the  $5.11 \times 10^6$  km<sup>2</sup> of Amazon lowlands defined as areas lower than  
201 500 m elevation based on the Shuttle Radar Topography Mission Digital Elevation Model (SRTM  
202 DEM) for the area of dataset comparisons in our study. This decision is consistent with several  
203 studies limited to lowlands because of the limitations of certain methods in estimating flooding in  
204 mountainous terrain (Hess et al., 2015).

205 In addition to basin-scale datasets, estimates of inundated areas for 11 individual wetland  
206 complexes (also referred to as “subregional”) in the Amazon basin were analyzed, including seven  
207 areas for which more detailed estimates were available. This was performed to understand how the  
208 basin-scale datasets may vary in accuracy across different wetland types (Figure 1): Curuai  
209 floodplain lake (Arnesen et al., 2013; Rudorff et al., 2014), Janauacá floodplain lake (Bonnet et  
210 al., 2017; Pinel et al., 2019), Uatumã river floodplain (Resende et al., 2019), Mamirauá Reserve  
211 (Ferreira-Ferreira et al., 2015), Pacaya-Samiria wetlands (Jensen et al., 2018), Llanos de Moxos

212 wetlands (Ovando et al., 2016), lower Amazon floodplain (Park and Latrubesse, 2019), Amazon  
213 mainstem floodplain (from Iquitos to Gurupá), Purus floodplain, Roraima savannas, and Negro  
214 savannas. A brief summary of these wetlands is provided in supplementary Table S2, and their  
215 main features are summarized in the following. Curuai is representative of the shallow lakes in the  
216 lower Amazon floodplain. It is separated from the river by narrow levees (Rudorff et al., 2014)  
217 and has a high suspended sediment concentration. Janauacá is typical of the middle Amazon River  
218 floodplain, and is composed of a ria lake (i.e., a blocked valley lake with relatively sediment-free  
219 waters; Latrubesse (2012)) and “várzea” environments (white-water floodplains) in its northern  
220 part (Pinel et al., 2019). Uatumã River is an Amazon tributary with black-water floodplain  
221 (“igapó”), and includes the Balbina hydroelectric reservoir, operating since 1987, which affects  
222 the river’s hydrological regime (Schöngart et al., 2021). The Uatumã floodplain reach assessed  
223 here is the 300-km reach between Balbina dam and the confluence with the Amazon River. The  
224 Mamirauá Sustainable Development Reserve is located in the confluence between Solimões and  
225 Japurá rivers, and is characterized by a mosaic of “chavascal”, herbaceous, and low and high  
226 várzea vegetation (Ferreira-Ferreira et al., 2015). The Purus River is a major tributary, and its  
227 floodplain was chosen because of its large floodplain to river width ratio. Pacaya-Samiria wetlands  
228 are composed of flooded forests, palm swamps and peatlands in the upper Solimões River (Draper  
229 et al., 2014; Lähteenoja et al., 2012). The Llanos de Moxos floodable savannas occupy the  
230 interfluvial areas between the Beni, Mamoré and Madre de Dios rivers in the upper Madeira basin  
231 (Hamilton et al., 2004). The Negro savannas, locally known as “campina wetlands” and  
232 “campinarana wetlands”, depending on the vegetation density, are thought to have formed from  
233 regional neotectonic depressions and were called the “Septentrional Pantanal” given their large  
234 area (Rossetti et al., 2017a, 2017b; Santos et al., 1993). The Roraima floodable savannas extend

235 from Roraima State in Brazil to the Rupununi savannas in Guyana, and comprise mainly smaller  
 236 river floodplains interspersed with poorly drained interfluvial savannas subject to flooding by local  
 237 rainfall (Hamilton et al., 2002); here we only considered the Roraima wetlands in the upper Branco  
 238 River basin, which is within the Amazon basin.

239



240

241 Figure 1. The Amazon basin and its major wetland systems: (a) Amazon basin delineation (red lines) over the countries  
 242 of South America (black lines). (b) Land cover based on a 2010 map from the European Space Agency Climate Change  
 243 Initiative (ESA-CCI) (Bontemps et al., 2013), showing the distribution of forest and savanna across the basin, as well  
 244 as large floodplains (see methodology section 2.3). (c) Basin distribution of major wetland systems showing locations

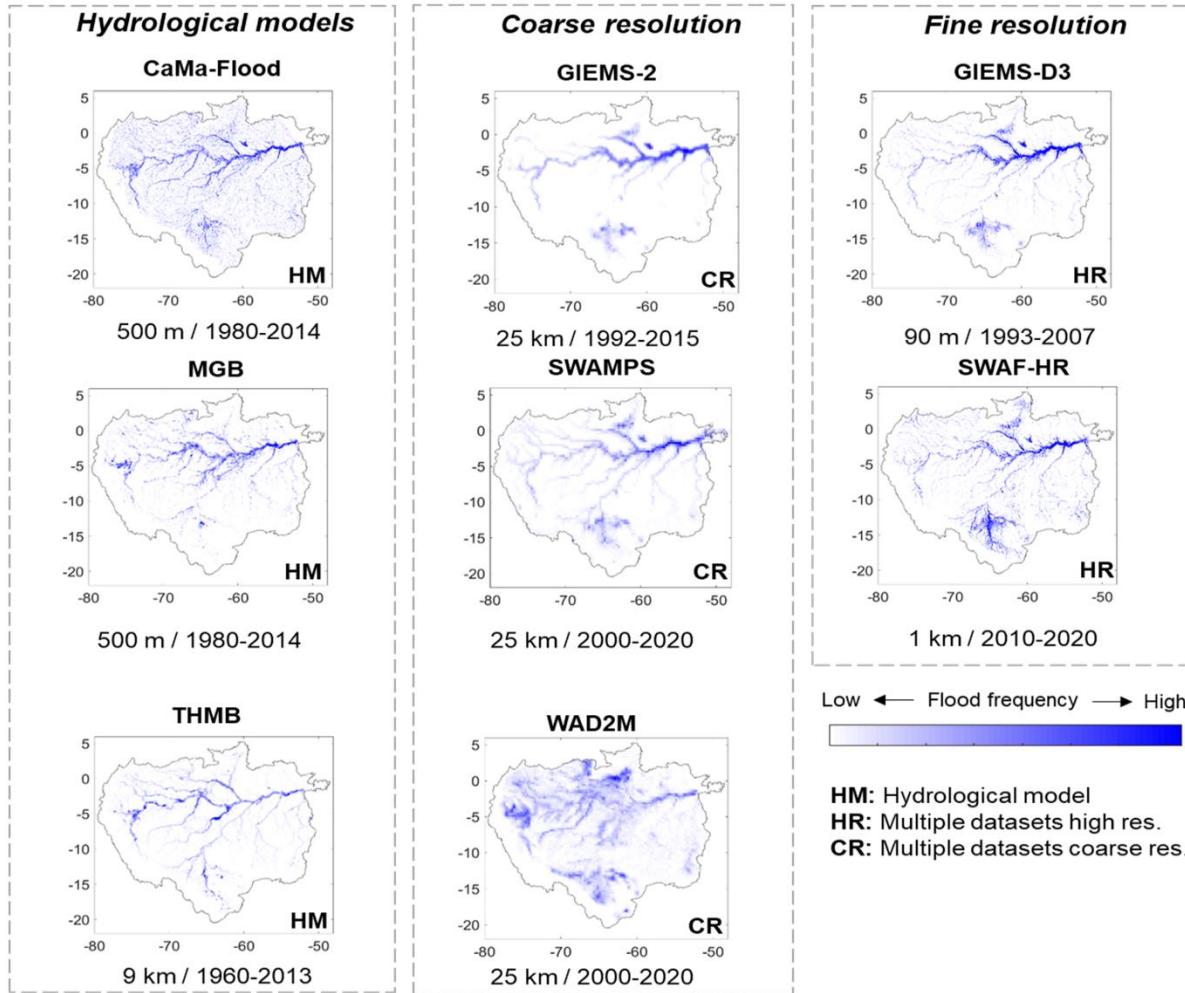
245 of interest for this study. Elevations lower than 500 m are shown in grey (based on SRTM DEM). The orange polygons  
246 show the areas for which a subregional dataset was available for this study (Figure 4), and the green ones show wetland  
247 areas of interest that do not have datasets specifically designed for these subregions. Photos depicting different wetland  
248 complexes for (d) Mamirauá (courtesy of João Paulo Borges Pedro), (e) Llanos de Moxos (courtesy of Alex Ovando),  
249 (f) Cabaliana floodplain lake close to Manacapuru (courtesy of Stephen Hamilton), and (g) Pacaya-Samiria (courtesy  
250 of Katherine Jensen) regions, respectively.

251

## 252 **2.2 Datasets**

253 Twenty-nine inundation datasets covering areas ranging from the whole-basin scale to individual  
254 wetland complexes, based on multiple data sources and spatiotemporal resolutions, were  
255 assembled for our comparison (Table 1). Most of these datasets are recent, with 18 out of the 29  
256 published since 2016, and 27 since 2011. They were chosen due to data availability and  
257 representativeness; other datasets that were either unavailable or methodologically redundant to  
258 those in our comparison were not used but are catalogued in Table S1. Overall, there are eight  
259 dynamic (weekly to monthly; Figure 2) and 10 static (which include long-term maximum, annual  
260 or dual-season categories; Figure 3) basin-scale datasets.

261

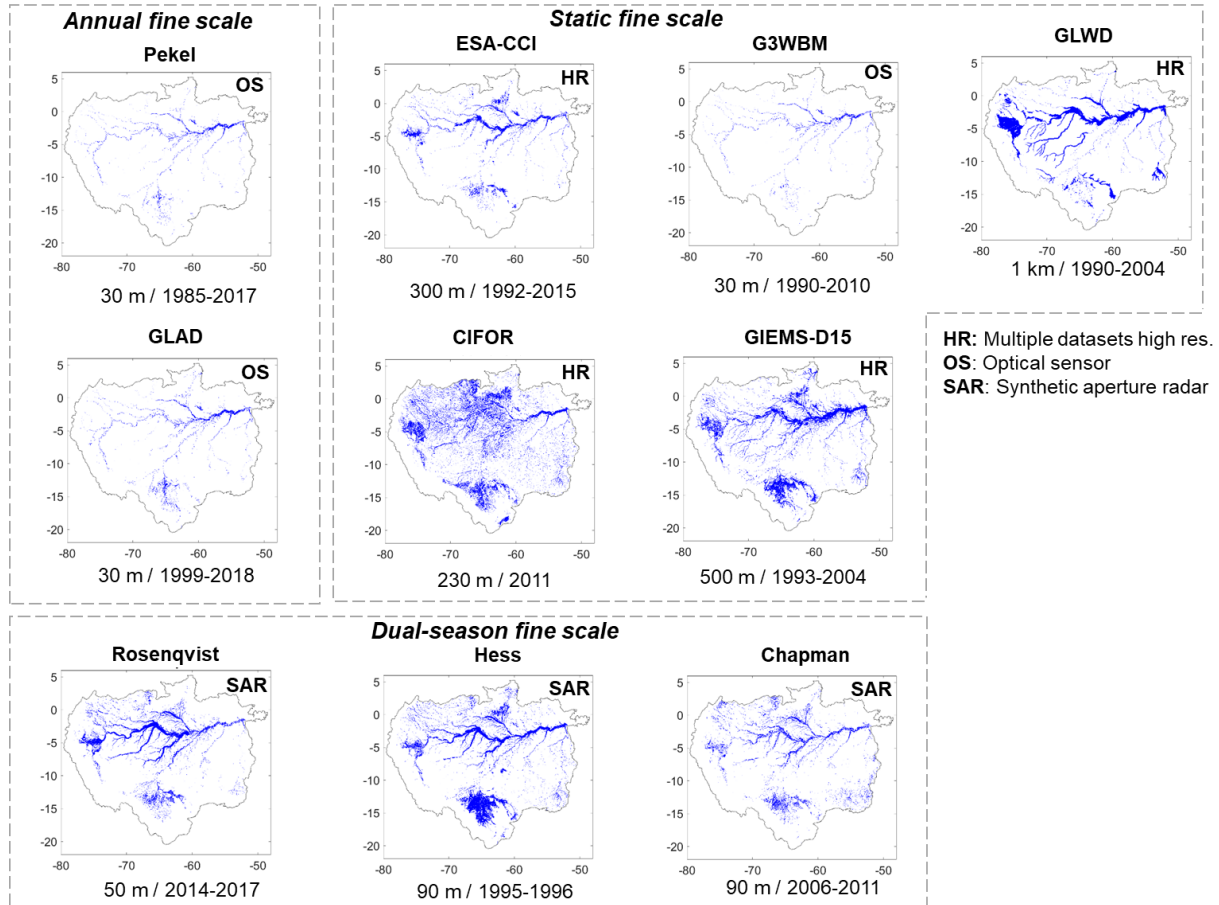


262

263 Figure 2. Basin-scale, dynamic inundation datasets used in this study, divided into three classes (hydrological models;  
 264 merging of multiple datasets at high resolution; merging of multiple datasets at coarse resolution). Long-term flood  
 265 frequency maps are provided for each dataset, calculated as the percentages of observations labelled as flooded  
 266 throughout the entire time-series.

267





268

269 Figure 3. Basin-scale, static or dual-season inundation datasets used in this study, divided into three classes (merging  
 270 of multiple datasets at high resolution; based on optical sensors; and based on SAR data). Flood frequency maps are  
 271 not provided because the datasets are mainly static or annual-based.

272

273 Passive microwave (PM) data are the basis of SWAF-HR, GIEMS family (GIEMS-D15, GIEMS-  
 274 D3, GIEMS-2), and SWAMPS, while ancillary data (i.e., optical imagery and microwave  
 275 scatterometry) are used to complement the PM signal. SWAF-HR data result from the  
 276 disaggregation of water surface fraction in a dataset at coarser spatial resolution (SWAF), based  
 277 on L-band passive microwave observations from the Soil Moisture and Ocean Salinity (SMOS)  
 278 satellite (Parrens et al. 2017). The disaggregation of SWAF relies on water occurrence maps from

279 GSWO and the Digital Elevation Model (DEM) Multi-Error-Removed-Improved-Terrain  
280 (MERIT) (Parrens et al., 2019). A global implementation of SWAF based on multi-angular and  
281 multi-polarization information has also been implemented (Al Bitar et al. 2020). GIEMS merges  
282 multiple satellite passive and active microwave observations, along with the optically-derived  
283 NDVI (Normalized Difference Vegetation Index), to detect the surface water and estimate the  
284 vegetation attenuation, for a monthly quantification of the surface water extent at ~25 km spatial  
285 resolution (Prigent et al., 2001, 2007, 2020; Papa et al., 2010). It is further disaggregated at 90-m  
286 resolution (GIEMS-D3) using a topographical downscaling methodology (Aires et al. 2017).

287 Three basin-scale datasets are based mainly on SAR data from JERS-1 (Hess et al., 2003, 2015),  
288 and its successor missions ALOS-PALSAR (Chapman et al., 2015) and ALOS-2 PALSAR-2  
289 (Rosenqvist et al., 2020). These three datasets cover different decades of observation but are  
290 methodologically similar.

291 Three of the optical-based datasets are based on Landsat data: GSWO (Pekel et al., 2016),  
292 G3WBM (Yamazaki et al., 2015) and GLAD (Pickens et al., 2020). Although GSWO and GLAD  
293 can provide monthly estimates for the Landsat archive (1984-today), given the inability of optical  
294 data to estimate flooding under cloud cover or dense vegetation canopies, only annual maximum  
295 and minimum values are used. For GLAD and GSWO, we consider a threshold of occurrence of  
296 surface water of 95% to estimate the minimum inundation (i.e., for the permanently inundated  
297 areas; Aires et al., 2018); otherwise, only a few isolated open water areas would be considered for  
298 the minimum extent.

299 The European Space Agency Climate Change Initiative dataset (ESA-CCI) is based on surface  
300 reflectance from MERIS, the Advanced Very High-Resolution Radiometer (AVHRR) and

301 PROBA-V data and Global Water Bodies from the Envisat Advanced Synthetic Aperture Radar  
302 (ASAR) (Bontemps et al., 2013). Since the wetland pixels in ESA-CCI varied negligibly  
303 throughout the years of observations, we use only the 2010 dataset as the ESA-CCI estimate for  
304 maximum inundation.

305 Another set of data is based on the merging of multiple global datasets: GLWD, GIEMS-D15 and  
306 WAD2M. GLWD is one of the first globally consistent databases of wetlands, which was based  
307 on a collection of wetland estimates from diverse institutions worldwide (Lehner and Döll, 2004).  
308 GIEMS-D15 combines GLWD, the Hydrosheds drainage network, and Global Land Cover 2000.  
309 WAD2M is based on SWAMPS and CIFOR within its merging framework. WAD2M is the only  
310 dataset to exclude open water areas (removal based on GSWO) due to its goal of estimating  
311 wetland methane emissions. SWAF-HR (Parrens et al., 2019) and GIEMS-D3 (Aires et al., 2017)  
312 use additional data and methodologies to downscale the original 25-km passive microwave-based  
313 SWAF (Parrens et al., 2017) and GIEMS (Papa et al., 2010; Prigent et al., 2007) datasets to 1 km  
314 and 90 m, respectively. While GIEMS-D3 has a different inundation magnitude than the original  
315 GIEMS due to merging with ancillary data, SWAF-HR conserves the same inundation magnitude  
316 across scales.

317 Among hydrological models, we selected representative datasets from each of the following broad  
318 modeling types: 1) process-based hydrologic models that use flood routing to represent inundation  
319 processes (i.e., from a simple kinematic wave model coupled to an inundation method to more  
320 complex flow routing methods); or 2) hydraulic (or hydrodynamic) models that consider the  
321 shallow water equations (or its simplifications) at any dimension (1D, 2D or 3D). For our analysis,  
322 we adopted two basin-scale models – one hydrologic (THMB; Coe et al. (2008)) and one  
323 hydrologic-hydrodynamic (MGB, Siqueira et al. (2018)), as well as a global-scale hydrodynamic

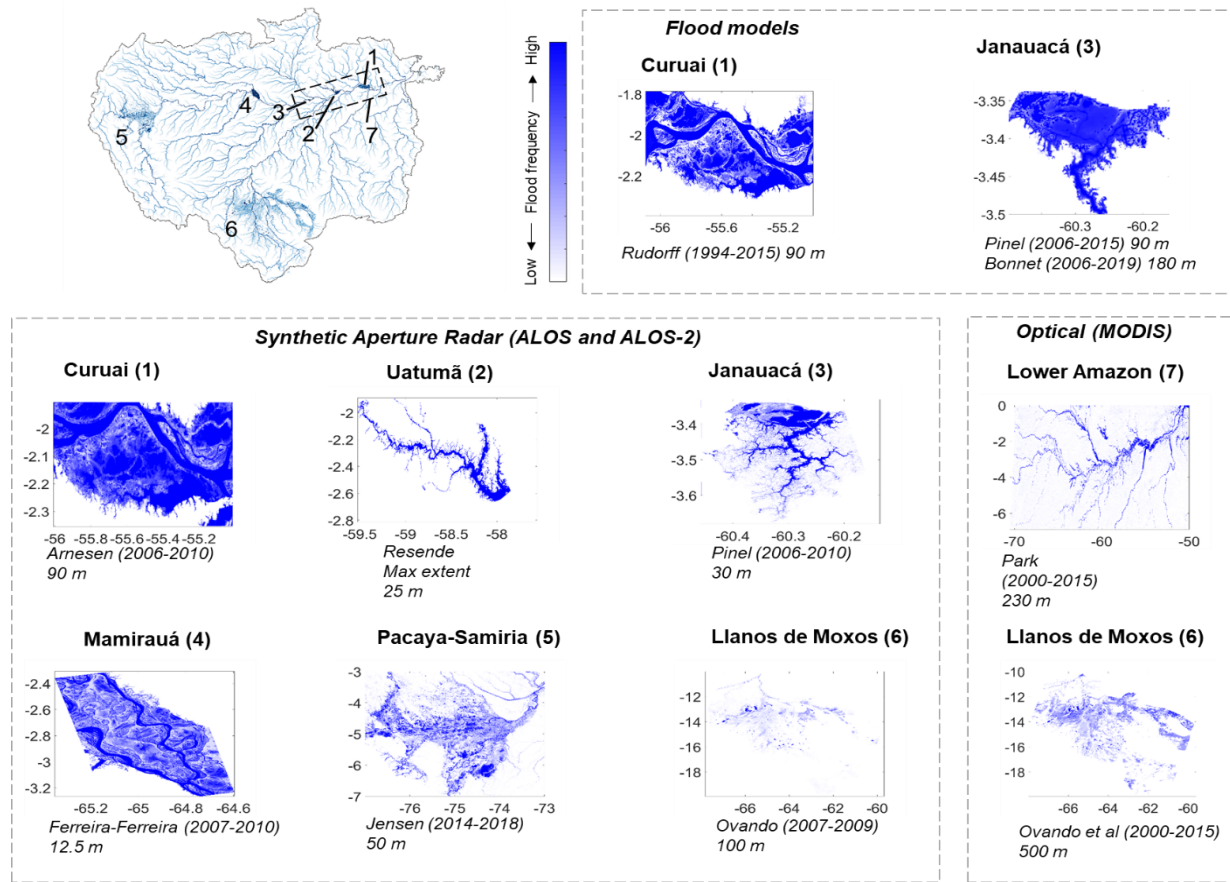
324 model (CaMa-Flood, Yamazaki et al. (2011)), in the Earth2Observe version available at  
325 <http://www.earth2observe.eu/>). The inundated area estimation is largely affected by the DEMs.  
326 The DEMs adopted in the model runs were: Bare-Earth (O’Loughlin et al., 2016) for MGB,  
327 MERIT (Yamazaki et al., 2017) for CaMa-Flood, and SRTM (Farr et al., 2007) for THMB. The  
328 rainfall/runoff input data are MSWEP v.1.1 daily precipitation (Beck et al., 2017) for MGB,  
329 HTESSEL daily runoff (Balsamo et al., 2009) for CaMa-Flood, and CRU TS v.3.2.1 monthly  
330 precipitation (Harris et al. 2014) for THMB. Although other hydrologic models have been applied  
331 to the Amazon basin (Tables 1 and S1), the models chosen here were selected as representative of  
332 global to local models, for having been well validated and applied over the Amazon basin, and for  
333 representing state-of-the-art Amazon hydrologic modeling. All basin-scale models represent one-  
334 dimensional (1D) flows only (i.e., floodplains are represented as storage units without active flow),  
335 and thus do not represent 2D surface flows that occur in wetlands (Alsdorf et al., 2007;  
336 Fleischmann et al., 2020). A detailed comparison of model capabilities and structural uncertainties  
337 is beyond our current scope. Hydrologic models have different temporal resolution depending on  
338 their numerical stability and forcing data. For instance, MGB and CaMa-Flood models run at an  
339 adaptive time step (sub-minute timestep in the case of MGB), but are assessed at daily resolution  
340 given their daily precipitation forcing. We aggregated the models’ estimates to monthly averages  
341 to make them comparable to the remote sensing dynamic datasets.

342 The datasets available for individual wetland complexes are presented in Figure 4. ALOS-2  
343 PALSAR-2 data were used for the Pacaya-Samiria region (Jensen et al., 2018), and the ScanSAR  
344 mode of ALOS/PALSAR for the following datasets: Curuai floodplain lake (Arnesen et al., 2013),  
345 Mamirauá Reserve (Ferreira-Ferreira et al., 2015), Uatumã river floodplain (Resende et al., 2019),  
346 and Janauacá floodplain lake (Pinel et al., 2019). MODIS optical data were used for the Llanos de

347 Moxos savannas in the upper Madeira River basin (Ovando et al., 2016) and the lower Amazon  
348 floodplain (Park and Latrubesse, 2019). Two local-scale 2D hydraulic models (LISFLOOD-FP for  
349 Curuai lake, Rudorff et al. (2014), and TELEMAC-2D for Janauacá lake, Pinel et al. (2019)), and  
350 one local-scale hydrologic model (for Janauacá lake; Bonnet et al. (2017)) were considered;  
351 together, these are representative of the state-of-the-art of hydrological modeling in Amazon  
352 wetlands.

353 The datasets were stored in various formats (i.e., raster and polygon shapefiles) and projections  
354 (mainly projected UTM and geographic coordinate system with WGS84 datum), and were  
355 converted to the WGS84 geographic coordinate system to compute areas. SWAMPS was provided  
356 at the Equal-Area Scalable Earth (EASE) Grid, which was used to estimate its flooded areas.  
357 Hydrologic model outputs were provided as either binary inundation maps or flood depth raster  
358 files, which were then converted into binary maps by assuming depth > 0 m as inundated pixels.

359



360

361 Figure 4. Long-term flood frequency maps from subregional inundation datasets (i.e., for individual wetland  
 362 complexes) used in this study. The Uatumã dataset (2) is static and is displayed as the maximum extent. Flood  
 363 frequency maps are produced by computing the long-term average of all inundation maps available for each dataset.

364

### 365 2.3 Comparison framework

366 The comparison framework involved the following analyses, considering the entire basin and 11  
 367 wetland complexes (seven areas with available subregional estimates, and four additional areas of  
 368 interest without subregional estimates; Figure 1):

- 369       ● Annual maximum and minimum inundation estimates for each of the 18 basin-scale  
370       datasets (section 3.1);
- 371       ● Basin-scale, long-term maximum and minimum inundation estimates for each of the 18  
372       basin-scale datasets (section 3.1);
- 373       ● Long-term maximum and minimum inundation estimates for each of the 18 basin-scale  
374       and 11 subregional datasets (section 3.2);
- 375       ● Comparison between basin-scale and subregional datasets with temporal (nRMSD and  
376       Pearson correlation) and spatial (Fit metric) assessment (section 3.2);
- 377       ● Assessment of spatial agreement among the 18 basin-scale datasets at 1 km, for both long-  
378       term maximum and minimum inundation maps (section 3.3);
- 379       ● Estimation of long-term maximum inundation for two classes of wetlands for the entire  
380       basin: (i) medium to large river floodplains and (ii) interfluvial wetlands and small  
381       floodplains (section 3.4).

382

383   The long-term maximum and minimum inundation extents were computed for each dataset as the  
384   area of all pixels that were inundated at least once in the whole monthly time series, for the  
385   maximum, and as those pixels that were always inundated, for the minimum. We stress that  
386   analyzing long-term changes in inundation patterns is beyond the scope of this study, and thus we  
387   assumed stationarity in our comparisons of long-term maximum and minimum inundation extents  
388   from different time-periods.

389   The agreement of all basin-scale, high-resolution datasets (i.e., all basin-scale ones except for  
390   THMB, GIEMS-2, SWAMPS and WAD2M, which have a coarse resolution between 9 and 25

391 km) was assessed for long-term maximum and minimum inundation at 1 km resolution, which is  
392 the resolution of SWAF-HR, the coarsest resolution among the high-resolution datasets. For each  
393 1 km pixel, the total number of datasets agreeing that it was inundated (either for maximum or  
394 minimum extent) was computed, following Trigg et al. (2016). Given the size of the Amazon basin,  
395 a 1 km resolution was considered adequate for the analysis. The analysis was done by aggregating  
396 all datasets to 1 km, and considering that a 1 km pixel is flooded if more than 50% of its area is  
397 flooded (following Hamilton et al., 2002). A sensitivity test was performed using a 25% threshold  
398 and led to similar conclusions at the whole basin scale (Figure S1).

399 The basin-scale and four additional subregional datasets were compared to seven subregional ones,  
400 which were used as independent validation datasets, and cover the following sites: Curuai  
401 (Arnesen et al., 2013), Uatumã (Resende et al., 2019), Janauacá (Pinel et al., 2019), Mamirauá  
402 (Ferreira-Ferreira et al., 2015), Pacaya-Samiria (Jensen et al., 2018), Llanos de Moxos MODIS  
403 (Ovando et al., 2016) and lower Amazon River (Park and Latrubesse, 2019). Varying degrees of  
404 validation exercises were performed for these validation datasets, with some being extensively  
405 validated with airborne videography (Hess et al., 2003) or local surveys (Arnesen et al., 2013;  
406 Ferreira-Ferreira et al., 2015; Jensen et al., 2018; Resende et al., 2019), while others were assessed  
407 through comparisons with other datasets (Pinel et al., 2019), or visually inspected, as in the large  
408 domains of the Llanos de Moxos (Ovando et al., 2016) and lower Amazon River (Park and  
409 Latrubesse, 2019) subregional datasets. The four additional subregional datasets are: Curuai  
410 LISFLOOD-FP model (Rudorff et al., 2014), Janauacá hydrological model (Bonnet et al., 2017),  
411 Janauacá TELEMAC-2D model (Pinel et al., 2019), and Llanos de Moxos ALOS-PALSAR  
412 (Ovando et al., 2016).



413 To use the subregional studies to assess the accuracy of the datasets covering broader areas, the  
414 basin-scale and four additional subregional datasets were compared to the subregional validation  
415 datasets at monthly temporal resolution, considering the total inundated area per wetland area (i.e.,  
416 the whole Curuai Lake domain, the whole Uatumã floodplain, and so forth). The polygons of each  
417 wetland area, which were used to extract the information from the basin-scale datasets, were  
418 delineated as a 1-km buffer around the maximum inundated area, according to each subregional  
419 dataset. For the four areas of interest without subregional datasets (Amazon mainstem and Purus  
420 floodplains, and Roraima and Negro wetlands), the polygons were created considering the  
421 maximum lateral extent in accordance with the MERIT DEM (Yamazaki et al., 2017) and ESA-  
422 CCI land cover for savannas. The time series were compared with Pearson linear correlation (R)  
423 and the normalized root mean square deviation (nRMSD), computed as the RMSD between a given  
424 inundation map and the subregional validation map (i.e., the individual wetland complexes)  
425 divided by the subregional long-term average inundation. The term ‘deviation’ was preferred over  
426 ‘error’ to stress the uncertainties inherent to all datasets, for both basin and subregional scales,  
427 although those derived for an individual wetland complex are considered as superior in accuracy  
428 for having a more dedicated data processing for that particular area, and being validated with  
429 ground surveys in some cases.

430 The ability of a particular dataset to estimate the local spatial patterns at maximum inundation was  
431 assessed with the Fit metric (Bates and De Roo, 2000), which has been successfully applied to  
432 compare inundation datasets (Bernhofen et al., 2018), and is computed as:

433 
$$Fit = 100\% * \frac{A \cap B}{A \cup B} (1)$$

434 Where  $A$  and  $B$  are the subregional validation dataset estimates (e.g., the subregional map that  
435 corresponds to maximum inundation) and the basin-scale maximum inundation maps.

436 To assess different wetland environments, we differentiate medium to large river floodplains from  
437 interfluvial wetlands and small floodplains. An estimation of the total flooded area of large river  
438 floodplains was computed, considering river reaches with upstream drainage area larger than 1,000  
439 km<sup>2</sup>, and a buffer mask around the river reaches (mask presented in Figure 1). The buffer was  
440 defined based on the Hydrosheds drainage network (Lehner and Grill, 2013), segmented into 15  
441 km-long reaches as in Siqueira et al. (2018). The buffer was proportional to the local reach drainage  
442 area and further manually adjusted to include the maximum floodplain lateral extent, as estimated  
443 from a visual inspection of the MERIT DEM (Yamazaki et al., 2017) and the three basin-scale  
444 SAR-based datasets (Hess, Chapman and Rosenqvist datasets). Buffer values varied from 4 km in  
445 upper reaches to 150 km on the Amazon mainstem close to the Mamirauá Reserve. Estimating  
446 floodplain total inundated area is relevant to differentiate the Amazon riverine fringing floodplains  
447 from non-floodplain wetlands (here referred to as interfluvial wetlands).

448 Finally, in order to assess the current capabilities of basin-scale mapping of inundation dynamics  
449 at high spatial and temporal resolution, a further assessment of the four high-resolution dynamic  
450 datasets (GIEMS-D3, CaMa-Flood, SWAF-HR and MGB) at their native resolutions was  
451 performed by computing their long-term flood frequency for the entire basin.

452

### 453 **3. Results and Discussion**

#### 454 **3.1 How much inundation is estimated to occur in the Amazon basin?**

### 455 *3.1.1 Overall assessment*

456 Comparisons among the various estimates of inundation area can begin with the maximum and  
457 minimum inundated area across the entire Amazon basin. We found wide variation in the annual  
458 maximum and minimum inundation estimates for the entire basin scale (Figure 5), as well as the  
459 long-term maxima and minima (Figure 6 and Table 2). The annual maximum inundation area  
460 represents the total area subject to inundation at some point over the year, whereas the annual  
461 minimum inundation area represents the area that remained inundated all year. SAR estimates,  
462 especially those based on L-band sensors and those having undergone validation (i.e., the Hess et  
463 al. (2003) dataset), are assumed to be the most accurate given their high spatial resolution and  
464 capability of mapping flooded areas under dense vegetation canopies and cloud cover. Given the  
465 lack of ground validation for most basin-scale datasets, we assess their accuracy by comparing  
466 them to subregional validation datasets in section 3.2.

467 By computing means and standard deviations of the long-term maximum area subject to inundation  
468 by type of data (Table 2), we obtain the following values:  $138,200 \pm 45,300 \text{ km}^2$  (mean  $\pm$  S.D.) for  
469 optical,  $533,500 \pm 217,800 \text{ km}^2$  for multiple datasets at high resolution,  $579,100 \pm 108,900 \text{ km}^2$   
470 for those at coarse resolution,  $542,800 \pm 80,600 \text{ km}^2$  for hydrological models, and  $599,700 \pm$   
471  $81,800 \text{ km}^2$  for SAR. The mean area for optical-based datasets is thus around 23% of the SAR-  
472 based estimate. If we assume that the ensemble of datasets could be a proxy of inundation  
473 uncertainty in the Amazon basin, and neglecting the optical and land cover-based data (G3WBM,  
474 GLAD, GSWO and ESA-CCI) and CIFOR datasets, given their lower capability to map inundation  
475 as discussed below, 13 datasets are left, yielding an estimation for the long-term maximum  
476 inundation of  $559,300 \pm 81,100 \text{ km}^2$ . This value is around  $40,000 \text{ km}^2$  lower than the mean of the  
477 maximum inundation area from the three SAR datasets. The mean of the maximum inundation

478 area considering all 18 datasets is  $490,300 \pm 204,800 \text{ km}^2$ . Compared to the maximum inundation  
479 area, the relative deviation among available estimates is higher for the long-term minimum area  
480 inundated —  $125,900 \pm 77,600 \text{ km}^2$  (mean  $\pm$  S.D.), with a coefficient of variation of 0.62, for the  
481 12 basin-scale datasets that provide minimum area, and  $139,300 \pm 127,800 \text{ km}^2$  for the three SAR-  
482 based datasets, with a coefficient of variation of 0.92.

483 None of the datasets can map small, narrow floodplains or riparian zones, for which only simple  
484 calculations are currently available (e.g., Junk et al., 1993), and whose total area can only be  
485 estimated through statistical extrapolation of observable rivers. These small zones contribute to  
486 the overall uncertainties of the inundation estimates. For instance, a wetland mask developed by  
487 Hess et al. (2015) for SAR-based wetland classification yielded a basin-scale estimation of wetland  
488 area including the smallest floodplains of  $840,000 \text{ km}^2$ . This estimate is much larger than the  
489 largest long-term maximum inundated area obtained with SAR data ( $659,100 \text{ km}^2$  with  
490 Rosenqvist’s dataset). In section 3.2, it will be shown that almost all datasets tend to underestimate  
491 the maximum inundation, when compared to subregional ones. The two SAR-based datasets with  
492 highest accuracy underestimate maximum inundation by 9% (Rosenqvist) and 13% (Hess), based  
493 on the average difference between these and the subregional estimates for the seven locations with  
494 available data. If this holds true for the whole basin, the basin-scale maximum inundation would  
495 be around 10% higher.

496

### 497 *3.1.2 Estimates based on SAR datasets*

498 At the basin scale, SAR-based estimates of maximum annual inundation range from  $424,600 \text{ km}^2$   
499 (Rosenqvist) to  $633,500 \text{ km}^2$  (Hess), and minimum inundation from  $53,900 \text{ km}^2$  (Rosenqvist) to

500 284,200 km<sup>2</sup> (Hess), as shown in Figure 5. By considering long-term maximum inundation (i.e.,  
501 all pixels that were inundated at least once in the entire available time series), instead of annual  
502 maxima, the SAR-based estimates range from 506,400 km<sup>2</sup> (Chapman) to 659,100 km<sup>2</sup>  
503 (Rosenqvist) for the entire basin (Table 2). The minima vary from 42,400 km<sup>2</sup> (Rosenqvist) to  
504 284,200 km<sup>2</sup> (Hess). This highlights the large differences that exist, especially for the minima,  
505 usually referred to as the “low-water period.” Chapman’s dataset, based on the 2006-2011 ALOS-  
506 PALSAR archive, has a smaller total maximum inundation area than the other two SAR datasets,  
507 as well as a smaller estimate for minimum inundation in relation to Hess’ estimate, which in turn  
508 was developed from SAR mosaics at two seasons spanning only one year (1995–1996).  
509 Differences among the three datasets may originate from differences in acquisition dates,  
510 interannual and seasonal inundation variability, algorithms, spatial resolutions, or inconsistencies  
511 regarding the data processing. For example, Chapman estimates long-term maxima and minima  
512 based on multiple years, while Hess and Rosenqvist provide annual values. The calibration  
513 uncertainty was also higher for the JERS-1 data used in Hess’ mapping than in the subsequent  
514 satellites (ALOS-PALSAR and ALOS-2 PALSAR-2) (Hess et al., 2003). For long-term minimum  
515 inundation, the interannual variability seems to be a minor factor since the Hess dataset, which  
516 estimated a larger figure than the other ones, was developed for a year with minimum water levels  
517 higher than those during Chapman’s acquisition dates, but lower than those during Rosenqvist’s  
518 ones (see Fig. 8 in Rosenqvist et al., 2020). Thus, the larger minimum inundation extent by Hess  
519 et al. (2015) seems to be more related to algorithm differences (Figure S2). For the maximum  
520 water levels, Hess’ period was associated with an average year, below the water levels in Chapman  
521 and Rosenqvist, and this may explain the relatively higher long-term maximum inundation by  
522 Rosenqvist, while Chapman’s smaller values are likely due to algorithm differences. For the

523 western basin, Hess' estimate is based on JERS-1 data mostly from June 1996 (Hess et al., 2015),  
524 which likely missed some of the inundation in this region as in the Pacaya-Samiria region, and  
525 may partly explain the larger value by Rosenqvist (see section 3.2.2). Spatial resolution is also an  
526 important factor: Rosenqvist's resolution is 50 m, and it is capable of representing smaller  
527 floodplains than the other two (Figure S3), as will be discussed in section 3.2.2.

528

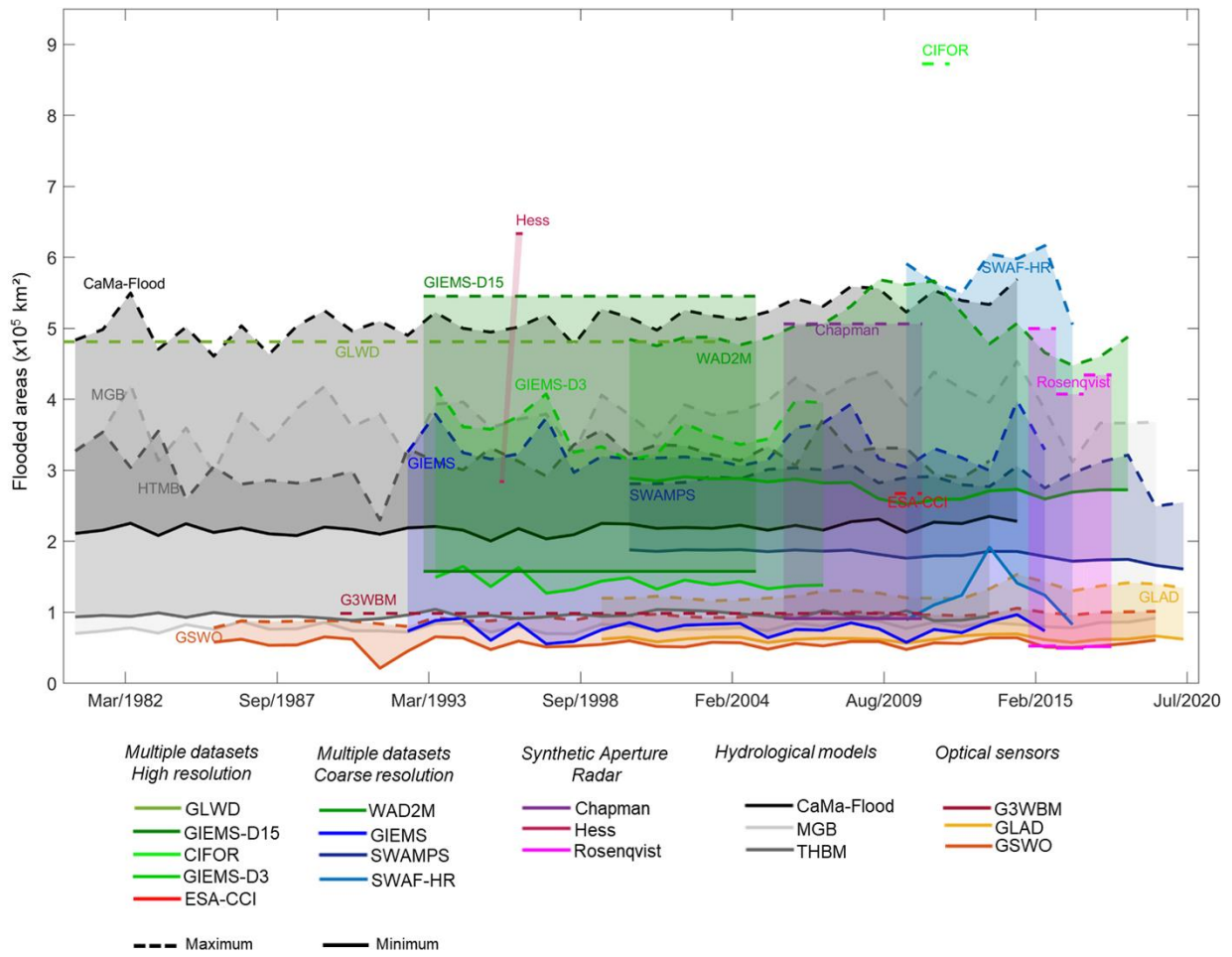
### 529 *3.1.3 Assessment of other datasets*

530 The coarse-resolution datasets and hydrologic models generally estimate smaller annual maximum  
531 inundation areas in comparison to the SAR datasets, with the exception of SWAF-HR, WAD2M  
532 and CaMa-Flood that yield similar annual maximum inundation. This results from the low  
533 sensitivity of the passive microwave signal, which underlies most coarse-resolution datasets, to  
534 detect small fractional flooded areas within the grid cells, flooding under particularly dense  
535 vegetation, and flooding of short duration (i.e., less than one month of consecutive inundation)  
536 (Hamilton et al., 2002). The higher sensitivity of the SWAF-HR may be associated with the use of  
537 L-band passive microwave emission. Given the long-term data availability from dynamic, coarse-  
538 resolution datasets, their long-term mean estimates are closer to the SAR ones, varying from  
539 450,800 km<sup>2</sup> (THMB) to 630,900 km<sup>2</sup> (SWAF-HR), when compared to the annual scale analysis.  
540 Therefore, no clear relationship between long-term minimum or maximum inundation and the  
541 spatial resolution of the datasets is observed (Figure 6), which could be expected when analyzing  
542 the annual values (Figure 5).

543 As expected, the optical-based datasets (GSWO, G3WBM, GLAD) cannot map inundation under  
544 dense vegetation canopies and thus lead to much lower estimates of basin-wide inundation area

545 (Aires et al., 2018; Parrens et al. 2017). Similarly, ESA-CCI, which is based on land cover  
546 classification of optical imagery with the addition of SAR inputs for delineation of wetland areas,  
547 yields low basin-wide inundation areas, although relatively higher than the purely optical-based  
548 estimates. In contrast, the multi-satellite-based CIFOR provides an unrealistically large estimate  
549 of maximum inundation area (872,700 km<sup>2</sup>), which may be due to overestimation of soil moisture  
550 by the topographic index used. This method is sensitive to rainfall overestimation, which may have  
551 occurred in 2011, the year for which CIFOR was developed (Gumbricht et al., 2017). While the  
552 dataset does represent well the spatial extent of peatlands across the Pacaya-Samiria region  
553 (Gumbricht et al., 2017), its estimation of widespread inundation across the basin has limitations  
554 to represent the large Amazon river floodplains, especially the forested ones, which are classified  
555 as “swamps (including bogs)” by this dataset together with extensive interfluvial areas (Figure S4).

556



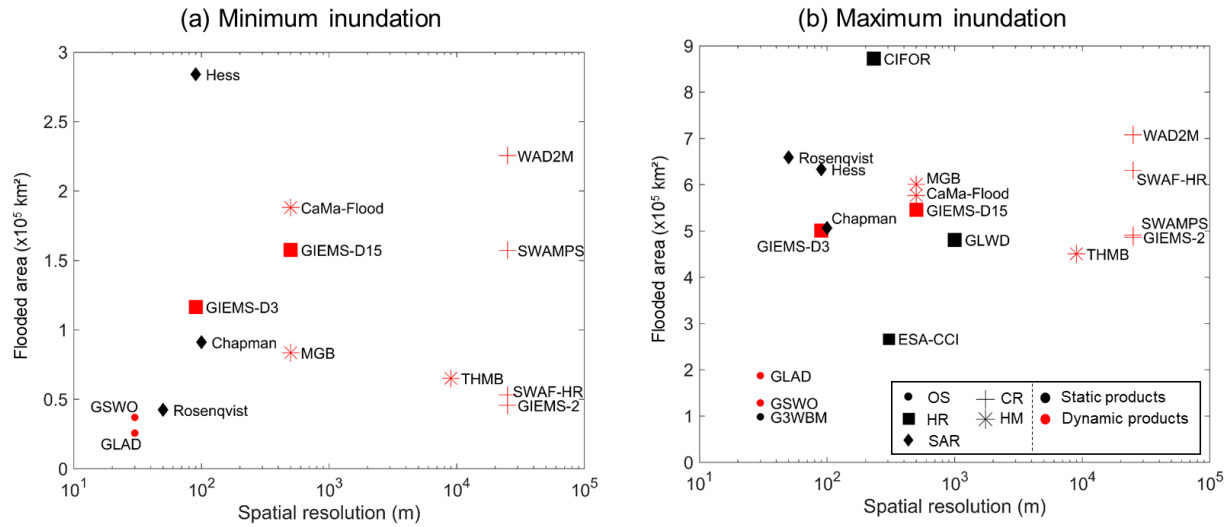
557

558 Figure 5. (a) Annual maximum and minimum flooded areas for the Amazon basin (< 500 m in elevation) for 18 basin-  
 559 scale datasets over their respective observation time periods. Note that some datasets provide only average estimates  
 560 based on multiple years of observation (e.g., GLWD, Chapman, G3WBM), and are marked as horizontal lines for the  
 561 period of observation.

562

563





564

565 Figure 6. Summary of long-term (a) minimum and (b) maximum inundation for the 18 basin-scale datasets, which are  
 566 categorized into five types (optical data; combination of datasets at high resolution; combination of datasets at low  
 567 resolution; synthetic aperture radar; and hydrological models). Estimates by dynamic datasets are not directly  
 568 comparable to the static ones; thus, each is colored differently: red (dynamic) and black (static). Legend for dataset  
 569 types: OS: Optical Sensor; SAR: Synthetic Aperture Radar; HM: Hydrological Model; HR: multiple datasets at High  
 570 Resolution; CR: multiple datasets at Coarse Resolution.

571 Table 2. Basin-scale, long-term minimum and maximum inundation estimates for 18 datasets.

	Dataset	Minimum (km <sup>2</sup> )	Maximum (km <sup>2</sup> )
Multiple datasets at coarse resolution	GIEMS-2	45,800	486,600
	SWAMPS	157,400	491,100
	WAD2M	225,500	707,900
Multiple datasets at high resolution	GIEMS-D3	116,600	500,700
	CIFOR	-	872,700
	ESA-CCI	-	267,400
	GIEMS-D15	157,700	545,400
	GLWD	-	481,200

	SWAF-HR	53,200	630,900
Hydrological model	THMB	65,200	450,800
	CaMa-Flood	188,100	576,700
	MGB	83,600	600,900
Optical sensor	G3WBM	-	98,500
	GLAD	25,700	187,600
	GSWO	37,000	128,500
Synthetic Aperture Radar	Hess	284,200	633,500
	Chapman	91,200	506,400
	Rosenqvist	42,400	659,100

572

### 573 **3.2 How much inundation is estimated to occur in individual wetland regions?**

#### 574 **3.2.1 Overall assessment**

575 The 18 basin-scale inundation datasets were compared with the 11 subregional ones through  
576 analysis of long-term means of annual maximum inundated areas (Table 3), long-term means of  
577 annual minimum areas (Supplementary Table S3), and multiple comparison metrics  
578 (Supplementary Table S4). The subregional datasets, covering individual wetland complexes, are  
579 considered as independent validation datasets, given the ground validation performed for most of  
580 them, as well as the use of a region-specific classification, and the often higher spatial resolution  
581 (e.g., 12.5 m for some based on ALOS-PALSAR imagery).

582 The Amazon River floodplains (from Iquitos to Gurupá) and the Llanos de Moxos regions are the  
583 largest Amazon wetland complexes:  $106,800 \pm 25,800 \text{ km}^2$  and  $113,500 \pm 53,400 \text{ km}^2$ , respectively  
584 when considering the three SAR-based datasets, and  $94,100 \pm 32,500 \text{ km}^2$  and  $85,300 \pm 52,400$

585 km<sup>2</sup> when considering all 18 basin-scale datasets. Besides these two areas, the third largest  
586 Amazon wetland region is Pacaya-Samiria, with 29,700 ± 20,600 km<sup>2</sup> (all datasets) and 40,000 ±  
587 4,200 km<sup>2</sup> (SAR datasets).

588 The comparison of the long-term means of annual maximum and minimum observed inundation  
589 over the available time periods indicates differences between basin-scale datasets and the  
590 subregional validation datasets. Overall, the subregional datasets had a larger maximum inundation  
591 extent than that estimated for the subregion from the basin-scale datasets. The underestimation by  
592 the basin-scale ones varied from 49% for the Pacaya-Samiria region to 5% for the lower Amazon  
593 River floodplain. Only three datasets overestimated the maximum extent of inundation: GIEMS-  
594 D3, GIEMS-D15 and GLWD. The basin-scale, SAR-based ones (Hess, Chapman and Rosenqvist)  
595 underestimated the maximum extent in the regions represented by all subregional datasets, except  
596 Rosenqvist for Janauacá Lake, and Hess for the Llanos de Moxos region. This is likely related to  
597 the higher resolution of many of the subregional datasets (e.g., 12.5 m original and 25 m final  
598 resolution for the Uatumã ALOS-PALSAR classification by Resende et al., 2019), differences in  
599 image acquisition period, and fine-tuning that may occur with dedicated processing for a particular  
600 region.

601 To investigate the depiction seasonal patterns of inundation by the various datasets, we assessed  
602 the correlation between the time series of absolute inundated areas from the dynamic ones and the  
603 estimates for individual wetland complexes (Table S3). Overall, all datasets agreed well (average  
604 Pearson correlation larger than 0.63 for the four wetland complexes with available time series),  
605 showing a similar depiction of the inundation seasonality. However, their ability to monitor high-  
606 resolution flood frequency is limited, as will be further discussed in section 4. A visual comparison  
607 of the time series (Figure S6) shows agreement on seasonal timing of flooding and drainage, but

608 disagreement in the extent of inundation. In particular, two datasets have a small overall annual  
609 amplitude (SWAMPS and WAD2M).

610 Overall, four datasets had the best overall representation of spatial patterns in inundation (Fit  
611 metric; see Equation 1), as analyzed at 1 km pixel resolution, in comparison to the subregional  
612 validation datasets: Hess, GLWD and the two hydrodynamic models (MGB and CaMa-Flood),  
613 which were associated with average Fit metric between 0.64 and 0.67 (Table S3). While hydrologic  
614 models such as MGB, CaMa-Flood and THMB have a satisfactory agreement basin wide, they are  
615 unable to represent wetlands not primarily inundated by rivers (Fleischmann et al., 2020; Zhou et  
616 al., 2021). For example, the Llanos de Moxos inundation is underestimated by both CaMa-Flood  
617 and MGB with low Fit metric values (0.19-0.28; Table S3). This is expected for interfluvial  
618 wetlands such as Llanos de Moxos and Roraima, where much of the flooding is caused by poor  
619 drainage of local rainfall and tends to be shallower, as opposed to overflow of large rivers onto  
620 adjacent floodplains. The four alternative subregional datasets assessed here - three hydrological  
621 models (one for Curuai and two for Janauacá) and one classification of ALOS-PALSAR data for  
622 the Llanos de Moxos area - were generally better or similar to some of the best-performing basin-  
623 scale ones, as could be expected given their fine tuning for the specific areas, which often includes  
624 local topographic surveys.

625 Some of the datasets merging multiple data sources overestimated the inundation area of individual  
626 wetland complexes the most, especially GIEMS-D15, GIEMS-D3 and GLWD. Furthermore,  
627 CIFOR was originally designed for peatland mapping in the tropics, and generally overestimates  
628 inundation, suggesting a widespread distribution of wetlands along interfluvial terraces across the  
629 whole basin that may include areas of poorly drained soils lacking surface water. For the individual  
630 wetland complexes, however, CIFOR generally underestimated inundation and had a poor

631 representation of spatial patterns of inundation (low Fit metric). WAD2M underestimated the  
632 maximum inundation the most, which is understandable given its removal of open water areas and  
633 because its main inputs (CIFOR and SWAMPS) also underestimated inundated areas as indicated  
634 by the subregional validation datasets.

635

### 636 *3.2.2 Individual inundation patterns based on SAR data*

637 Regarding the maximum inundation extent, the Janauacá case provides a representative  
638 example to understand the differences among multiple L-band SAR datasets: these estimated total  
639 inundated area as 209 km<sup>2</sup>, 184 km<sup>2</sup> and 446 km<sup>2</sup> for Hess, Chapman and Rosenqvist, respectively,  
640 in contrast to 404 km<sup>2</sup> with the subregional ALOS-PALSAR-based dataset (12.5 m resolution;  
641 Pinel et al., 2019). Part of these differences occur because of interannual variability, but other  
642 factors such as spatial resolution and algorithm differences seem relevant. Rosenqvist led to a more  
643 consistent estimation of the spatial inundation extent in terms of maximum inundation (Table 3)  
644 and inundation spatial patterns (Fit metric; Table S3), which can be a consequence of its higher  
645 spatial resolution (50 m) in contrast to the other two (90 m; Figure S3). Overall, Rosenqvist  
646 provided the largest inundation extent among SAR datasets across all areas along the Amazon  
647 mainstem floodplain, except for the Curuai floodplain and the savanna wetlands, as well as the  
648 closest agreement with subregional validation datasets ( $-9\% \pm 13\%$ ; average  $\pm$  S.D.). Hess  
649 estimated the largest inundation area in the savanna wetlands (Llanos de Moxos, Roraima and  
650 Negro). However, Hess' estimate is 39% larger than the subregional validation dataset for Llanos  
651 de Moxos, while the other two SAR estimates are lower ( $-26\%$  and  $-41\%$  for Chapman and  
652 Rosenqvist, respectively).

653 One important question remains about the low-water period, as discussed in the previous section  
654 for the basin-scale analysis. Hess suggests much more inundation for this period for the Amazon  
655 mainstem floodplains (54,500 km<sup>2</sup>), mainly for the upstream forested reaches, and for the whole  
656 basin in general (284,200 km<sup>2</sup>), than recent estimates with ALOS (28,500 and 91,200 km<sup>2</sup>) and  
657 ALOS-2 data (19,500 and 42,400 km<sup>2</sup>). An assessment with the subregional datasets along the  
658 Amazon floodplain suggests that Hess overestimates the minimum extent for Curuai, Mamirauá  
659 and lower Amazon River, and is accurate for the Janauacá floodplain lake. Rosenqvist generally  
660 underestimates the minimum inundation. For instance, for the Mamirauá dataset, the minimum  
661 extent (i.e., permanently flooded areas) sums up to 715 km<sup>2</sup>, which is increased to 1545 km<sup>2</sup> if  
662 considering all pixels flooded for more than 295 days per year. For this area, the SAR estimates  
663 are 1756 km<sup>2</sup> (Hess), 866 km<sup>2</sup> (Chapman) and 422 km<sup>2</sup> (Rosenqvist). Overall, this suggests that  
664 the actual value of minimum inundation across the central Amazon floodplains is somewhere  
665 between the Hess and Rosenqvist estimates.

666

### 667 *3.2.3 Challenges over floodable savannas*

668 Large discrepancies are observed for the Roraima and Negro floodable savannas. Roraima  
669 wetlands are small river floodplains interspersed with open savannas subject to flooding, which  
670 can be identified by optical data. In addition, the typical timing of high and low water in the  
671 Roraima region coincides approximately with the JERS-1 dual-season mosaics that were designed  
672 to reflect the seasonality of the central Amazon River floodplain (Hamilton et al. 2002). For these  
673 reasons, the JERS-1-based dataset by Hess et al. (2015) seems to satisfactorily represent most of  
674 the Roraima wetlands. However, it misses some small-scale riparian forests, given its 90 m spatial  
675 resolution and snapshot coverage that likely missed flooding events on smaller, flashier rivers

676 (Figure S5). Thus, the maximum inundation is likely higher than the Hess estimate (8,900 km<sup>2</sup>),  
677 which in turn is larger than the other ones based on SAR (1,900 - 4,100 km<sup>2</sup>). The only dataset to  
678 estimate a higher value is the coarse SWAF-HR (18,100 km<sup>2</sup>), which is similar to the value  
679 previously estimated by Hamilton et al. (2002) (16,500 km<sup>2</sup>), also with coarse data (SMMR passive  
680 microwave), though a part of the discrepancy may be due to interannual variability. More studies  
681 are necessary for this area to understand its actual inundation extent and dynamics. Similarly, the  
682 inundation estimates in the Negro interfluvial savannas are subject to large uncertainty, with the  
683 long-term maximum inundation varying between 95 (GLWD) and 20,700 km<sup>2</sup> (CIFOR),  
684 considering all basin-scale datasets. SAR-based estimates were between 5,900 and 15,800 km<sup>2</sup>. In  
685 contrast, for the Pacaya-Samiria interfluvial area, which includes a large complex of forested  
686 wetlands, peatlands and palm swamps, the discrepancies are smaller than for the savanna  
687 interfluvial regions, although still considerable. The basin-scale SAR ranged between 24,000 km<sup>2</sup>  
688 (Chapman) and 56,200 km<sup>2</sup> (Rosenqvist), with the subregional validation dataset yielding 57,900  
689 km<sup>2</sup>. The good agreement between Rosenqvist and the subregional dataset was already reported  
690 by Rosenqvist et al. (2020).

691

692 Table 3. Long-term maximum inundation areas (km<sup>2</sup>) for the 11 wetland complexes (up to three subregional datasets  
693 per complex) and the 18 basin-scale datasets. The subregional values refer to the following datasets, in this order  
694 (comma-separated values relate to areas with more than one dataset available): Curuai - ALOS (Arnesen et al., 2013)  
695 and LISFLOOD-FP model (Rudorff et al., 2014); Uatumã - ALOS (Resende et al., 2019); Janauacá - ALOS (Pinel et  
696 al., 2019), hydrologic model (Bonnet et al., 2017) and TELEMAC-2D model (Pinel et al., 2019); Mamirauá - ALOS  
697 (Ferreira-Ferreira et al., 2015); Pacaya-Samiria - ALOS-2 PALSAR-2 (Jensen et al., 2020); Llanos de Moxos -  
698 MODIS (Ovando et al., 2016) and ALOS (Ovando et al., 2016); and Lower Amazon River - MODIS (Park et al.,

699 2019). Average, standard deviation (S.D.) and coefficient of variation (CV) are presented for each area in the last  
700 rows.

	Dataset	Curuai	Uatumã	Janauacá	Mamirauá	Pacaya-Samiria	Llanos de Moxos	Lower Amazon	Amazon mainstem	Purus	Roraima savannas	Negro savannas
	Subregional	4162, 3720	1471	404, 336, 176	4476	57913	125422, 133470	56722	-	-	-	-
Multiple datasets at coarse resolution	GIEMS-2	3080	984	623	3344	23344	156176	79871	116379	7208	7173	12237
	SWAMPS	3359	722	280	1131	9929	88753	58626	72468	5618	4970	8819
	WAD2M	681	243	166	888	42635	102780	29276	49261	6698	3173	15450
Multiple datasets at high resolution	GIEMS-D3	4643	2732	505	3569	11562	150285	92908	127552	9045	12355	15123
	CIFOR	3796	994	177	1714	52590	116201	43509	86301	10844	3728	20712
	ESA-CCI	3236	855	260	3045	28727	39795	37475	84803	8883	510	12623
	GIEMS-D15	4635	2681	416	2444	44536	117979	86123	127150	11186	8129	14854
	GLWD	4275	2267	535	4259	79124	40661	67746	140921	14840	1048	95
	SWAF-HR	4439	2199	388	3205	16900	159712	69539	110468	10785	18146	15375
Hydrological model	THMB	2883	554	164	2840	27748	52693	39193	89658	19733	4307	3640
	CaMa-Flood	4246	1613	534	3208	34096	80725	63963	118577	20947	3454	6560
	MGB	4098	1549	474	3750	33344	21757	61997	115047	20394	240	3224
Optical sensors	G3WBM	2732	628	135	795	2694	9564	27451	37718	2351	352	1238
	GLAD	3479	832	204	1141	4196	38897	36930	53121	3903	3495	3885
	GSWO	3163	675	150	962	3637	19240	31191	44731	2982	1442	1880
Synthetic Aperture Radar	Chapman	2796	934	184	2694	24001	73710	39677	77632	12499	4077	5935
	Hess	3996	1045	209	3985	39741	174198	52156	115822	15155	8950	15758
	Rosenqvist	3055	1238	446	4362	56160	92693	55262	126806	20738	1867	9935
	Average	3477	1264	325	2630	29720	85323	54050	94134	11323	4856	9297
	S.D.	949	748	163	1226	20591	52387	19956	32503	6185	4666	6201
	CV	27%	59%	50%	47%	69%	61%	37%	35%	55%	96%	67%

701

### 702 3.3 How much do the datasets agree on the spatial distribution of inundation?

703 Agreement maps of the high resolution datasets ( $\leq 1$  km spatial resolution) were developed for  
704 both long-term maximum (14 datasets available) and minimum inundation areas (10 datasets),  
705 based on the number of inundation datasets coinciding over a 1 km pixel (Figures 7 and 8 and their  
706 categorization for specific regions in Figure 9). Overall, 31% of the Amazon lowlands area (i.e.,



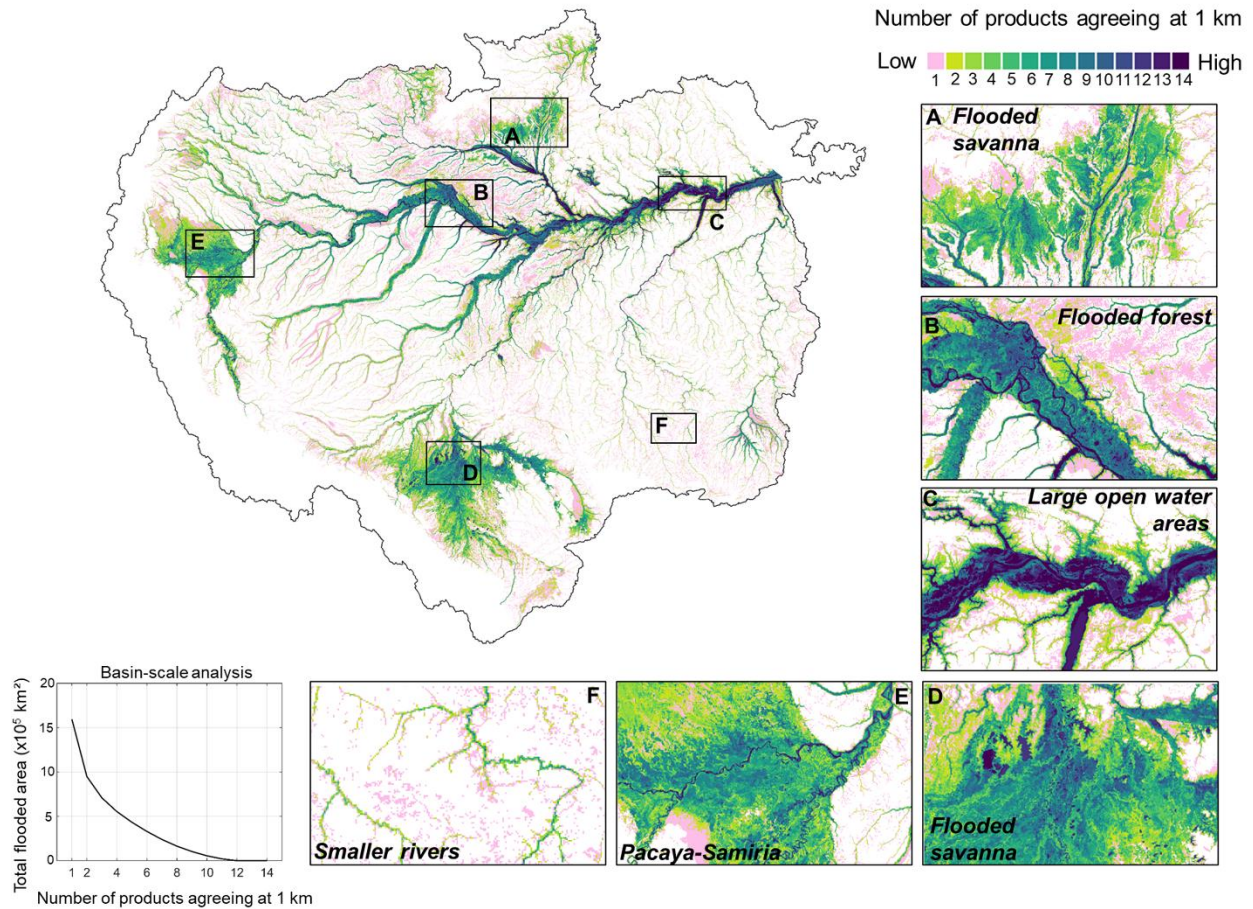
707 1.59 x 10<sup>6</sup> km<sup>2</sup> out of 5.11 x 10<sup>6</sup> km<sup>2</sup>) has been estimated as subject to inundation by at least one  
708 dataset (bottom left panel, Figure 7). Based on the agreement between two datasets, this value  
709 decreases to 948,300 km<sup>2</sup>, which is larger than the value estimated when there is agreement among  
710 four datasets (553,200 km<sup>2</sup>). This latter estimate is more similar to the average maximum  
711 inundation as estimated by the ensemble of datasets (559,300 km<sup>2</sup>) and the three SAR-based ones  
712 (599,700 km<sup>2</sup>). Furthermore, there is a lower agreement for the minimum inundation than for the  
713 maximum inundation among individual regions (Figure 9).

714 For specific regions, a high degree of agreement for floodplains dominated by open water areas is  
715 evident for the lower Amazon River reaches, followed by the forested floodplains fringing large  
716 rivers, especially along the Amazon mainstem, Purus and Negro rivers. The generally higher  
717 accuracies over central Amazon floodplains may also be related to the attention that dataset  
718 developers have devoted to it, in contrast to other regions. Furthermore, the maximum floodplain  
719 extent can be somewhat delineated with terrain elevation data (i.e., DEMs) using algorithms such  
720 as HAND (Rennó et al., 2008), which helps to explain the relatively small disagreement for  
721 floodplains fringing the largest rivers, and is particularly effective with vegetation bias-removed  
722 DEMs (O'Loughlin et al., 2016; Yamazaki et al., 2017). The best agreement (for both maximum  
723 and minimum inundation extent) occurred over the Curuai floodplain along the lower Amazon  
724 mainstem, with 37% of its area being estimated as subject to inundation by all 14 datasets (Figure  
725 9a). An agreement among all 14 datasets occurred, in part (i.e., more than 10% of the wetland  
726 area), for the central Amazon floodplains (Curuai, Uatumã, Janauacá and lower Amazon River)  
727 because of their relatively large fractions of open water areas.

728 In the interfluvial wetlands (Negro and Roraima savannas, Pacaya-Samiria and Llanos de Moxos),  
729 the inundation patterns are less dependent on riverine overflow and more dependent on local

730 rainfall, making them less predictable (Hess et al., 2003). The disagreement for both maximum  
731 and minimum inundation area is the largest across all regions, e.g., 65–78% of their flooded areas  
732 were mapped by only one model for the minimum inundation (Figure 9b). The Llanos de Moxos  
733 is conspicuous as a region of particular disagreement, perhaps because flooding is mainly shallow  
734 and in vegetated areas (mainly savannas/grasslands), and is highly variable from year to year. In  
735 general, the smaller the flooded patches the higher the challenge to map them, not only because of  
736 resolution but also due to small-scale variation in topography. Similar disagreement occurred in  
737 other interfluvial wetlands such as the Negro and Roraima savannas, and would be expected  
738 elsewhere in savanna floodplains of South America (e.g., Pantanal, Llanos de Orinoco and Bananal  
739 Island; Hamilton et al., 2002). The poor agreement over interfluvial areas, however, may also  
740 partly reflect the longer history of study of Amazon mainstem floodplains, for which there are  
741 river gage records that reflect floodplain water levels and inundation, while more remote areas  
742 such as the Negro savannas and Pacaya-Samiria regions are more challenging to represent with a  
743 few gages, and have received less attention. The challenges in estimating inundation over  
744 interfluvial areas also affect the SAR-based datasets, which disagreed the most over these regions  
745 (see section 3.5 and discussion in Rosenqvist et al., 2020).

746

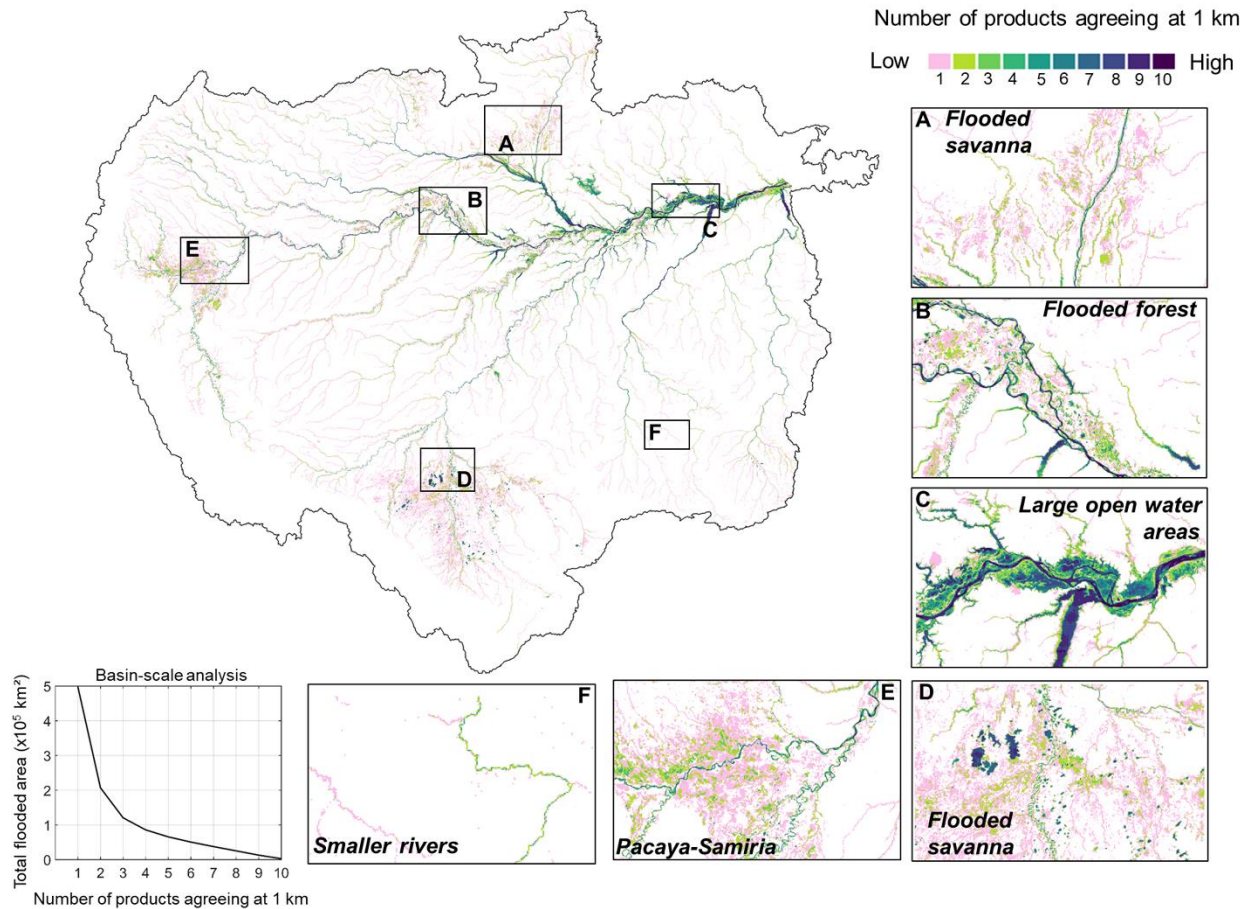


747

748 Figure 7. Agreement for maximum inundation area among 14 basin-scale datasets at high resolution ( $\leq 1$  km spatial  
 749 resolution): G3WBM, ESA-CCI, GLAD, GSWO, GLWD, CIFOR, GIEMS-D15, GIEMS-D3, Chapman, Hess,  
 750 Rosenqvist, SWAF-HR, CaMa-Flood and MGB. A given pixel of a dataset with resolution higher than 1 km that had  
 751 more than 50% of flooding at the maximum inundation extent is classified as inundated.

752

753



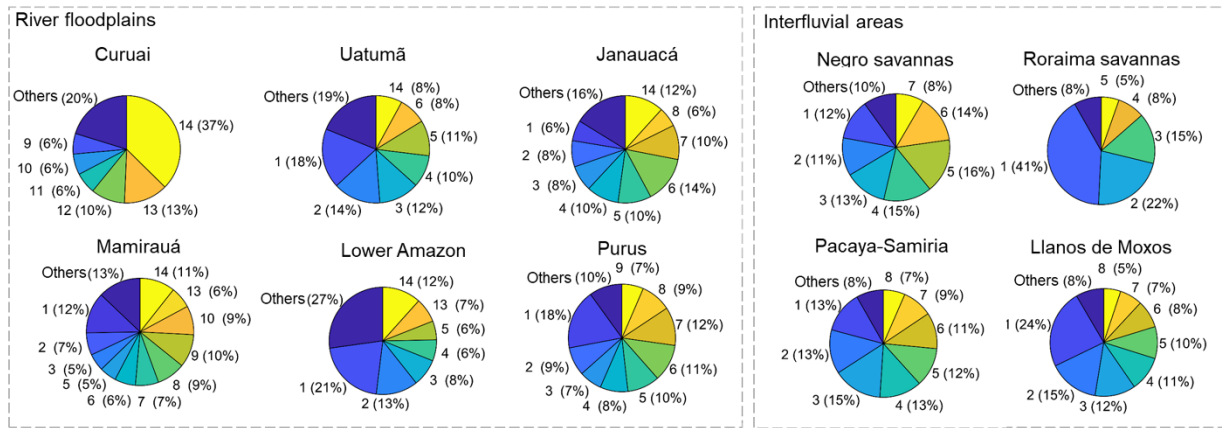
754

755 Figure 8. Agreement for minimum inundation area among 10 basin-scale datasets at high resolution ( $\leq 1$  km spatial  
 756 resolution): GIEMS-D15, Chapman, Hess, Rosenqvist, SWAF-HR, CaMa-Flood, MGB, GIEMS-D3, GSWO and  
 757 GLAD. A given pixel of a dataset with resolution higher than 1 km that had more than 50% of flooding at the minimum  
 758 inundation extent is classified as inundated.

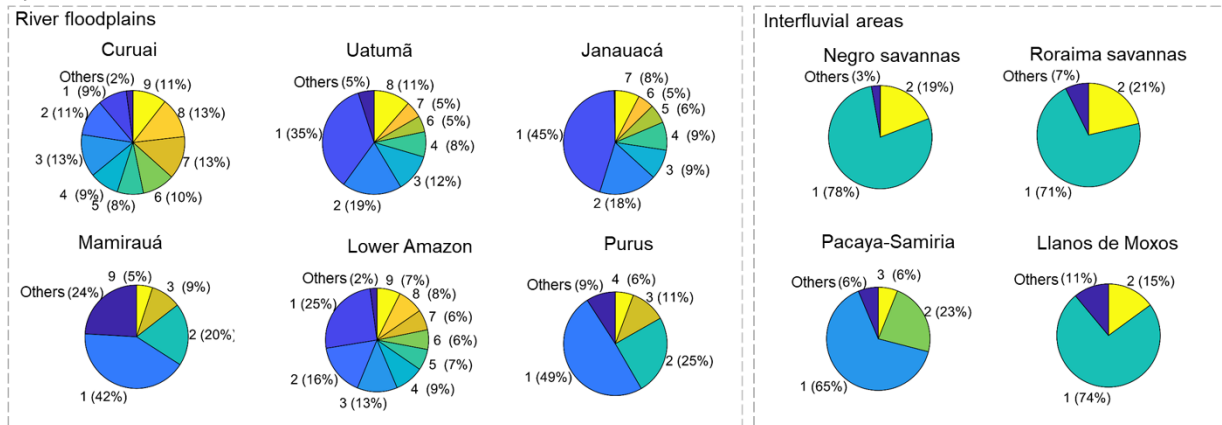
759

760

**a) Maximum inundation**



**b) Minimum inundation**



761

762 Figure 9. Degree of agreement for (a) maximum and (b) minimum inundation area for 10 individual wetland  
 763 complexes, based on the 1 km agreement map (Figures 7 and 8). The percentage values indicate the fraction of each  
 764 area where a given number of datasets agreed that it was flooded, e.g., 14 models agreed that 37% of the Curuai area  
 765 was flooded in the maximum inundation extent. The class with number 1 indicates the fraction of the area that only  
 766 one dataset estimated as being inundated. The class “others” refers to all classes that had less than 5% of pixels  
 767 estimated as being inundated.

768

769 **3.4 Quantifying the inundation extent of different wetland types**

770 Amazon wetlands include a myriad of ecosystems varying in geomorphology, hydrology, and  
771 vegetation cover. The classification system proposed by Junk et al. (2011) differentiated Amazon  
772 wetlands according to amplitude and range of water level change. Wetland types ranged from the  
773 forested swamps with stable water levels to river floodplains with oscillating water levels, and to  
774 interfluvial areas with small seasonal water level amplitude due to the main contribution of local  
775 rainfall and runoff (Fleischmann et al., 2020; Junk et al., 2011; Ovando et al., 2018).

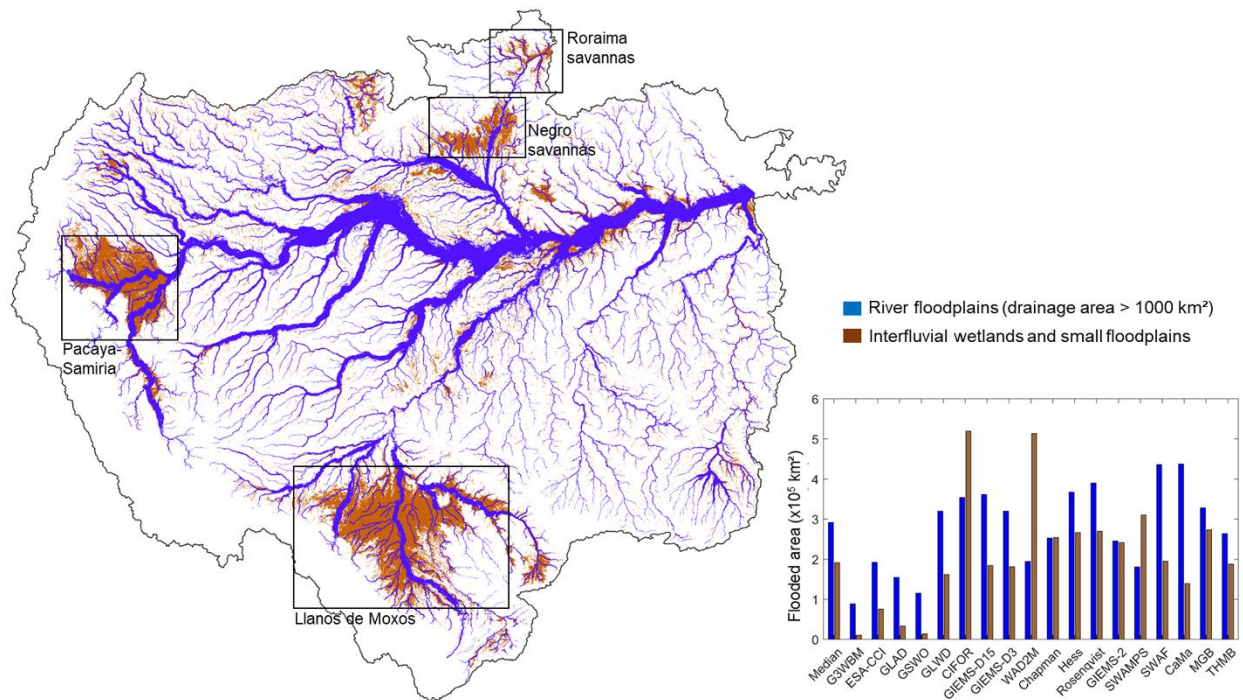
776 A simpler yet hydrologically meaningful classification is the categorization into river floodplains  
777 and interfluvial wetlands adopted here, since the former typically have a greater hydrological  
778 connection to the main river and thus are subject to a different control of inundation area by river  
779 levels (Reis et al., 2019a). We performed a quantitative analysis of the inundation area in these  
780 two main hydrological classes. All pixels considered flooded by at least two datasets, based on the  
781 1 km agreement map for maximum inundation extent (Figure 7), are presented in Figure 10.  
782 Overall, the medium to large river floodplains (upstream drainage area > 1000 km<sup>2</sup>) have a larger  
783 inundation extent than the category with small floodplains and interfluvial areas. An average total  
784 area subject to inundation of  $317,800 \pm 84,400$  km<sup>2</sup> (average  $\pm$  S.D.; median equal to 323,700 km<sup>2</sup>)  
785 was obtained for the medium to large floodplains, not including the optical and land cover datasets  
786 (G3WBM, GLAD, GSWO and ESA-CCI). A greater area for large floodplains was estimated by  
787 all except for CIFOR, SWAMPS and WAD2M. Two datasets estimated a similar value between  
788 the two classes (Chapman and GIEMS-2), which may be related to an overestimation of basin-  
789 scale isolated flooded patches.

790 Large floodplains fringing the main rivers, especially along the Amazon River, have been largely  
791 addressed by previous studies (Table 1 and Table S1). However, large river floodplains are also  
792 present in less studied reaches, e.g., in the upper Napo and Içá rivers in northwest Amazon basin,

793 and upper Xingu in the southeastern portion (see location in Figure 1). These upper reaches are  
794 subject to more sporadic, flashy river hydrological regimes (Hamilton et al., 2007), which make  
795 their inundation area difficult to map with current datasets of relatively low temporal resolution.  
796 In our analysis, the non-floodplain areas include mainly the large interfluvial areas (black  
797 rectangles in Figure 10), small river floodplains that are challenging to detect with currently  
798 available datasets, and some reservoirs, such as Balbina reservoir on the Uatumã River.

799 Besides the central Amazon floodplains, which have been widely studied, other wetland  
800 complexes require more attention, such as the Negro and Roraima savannas; the latter was only  
801 assessed by a single study to our knowledge (Hamilton et al., 2002). The inundation mapping of  
802 the Pacaya-Samiria region in the upper Amazon has received scientific attention recently (Jensen  
803 et al., 2018; Rodriguez-Alvarez et al., 2019), partially because of the region's role as a carbon sink  
804 via formation of peat (Draper et al., 2014; Lähteenoja et al., 2012). Regarding open water areas,  
805 Melack (2016) reported values ranging from 64,800 km<sup>2</sup> (Melack and Hess, 2010) to 72,000 km<sup>2</sup>  
806 (SRTM Water Body Data) and 92,000 km<sup>2</sup> (Hansen et al., 2013) for the Amazon basin (< 500 m  
807 in elevation). The three Landsat-based datasets assessed here, which are mainly capable of  
808 detecting open water areas, estimate 98,500 km<sup>2</sup> (G3WBM), 128,500 km<sup>2</sup> (GSWO) and 187,600  
809 km<sup>2</sup> (GLAD).

810



811

812 Figure 10. Quantification of maximum inundated areas over river floodplains with drainage area larger than 1,000  
 813 km<sup>2</sup>, and interfluvial wetlands and small floodplains (area < 1,000 km<sup>2</sup>) within the Amazon basin. The maximum  
 814 inundation map depicts all 1 km pixels with at least two datasets agreeing (i.e., a reclassification of Fig. 7), in order to  
 815 avoid overestimation caused by pixels with only one dataset classifying them as subject to inundation. The four large  
 816 areas of interfluvial wetlands are highlighted with black rectangles (Pacaya-Samiria, Llanos de Moxos, Negro and  
 817 Roraima savannas).

818

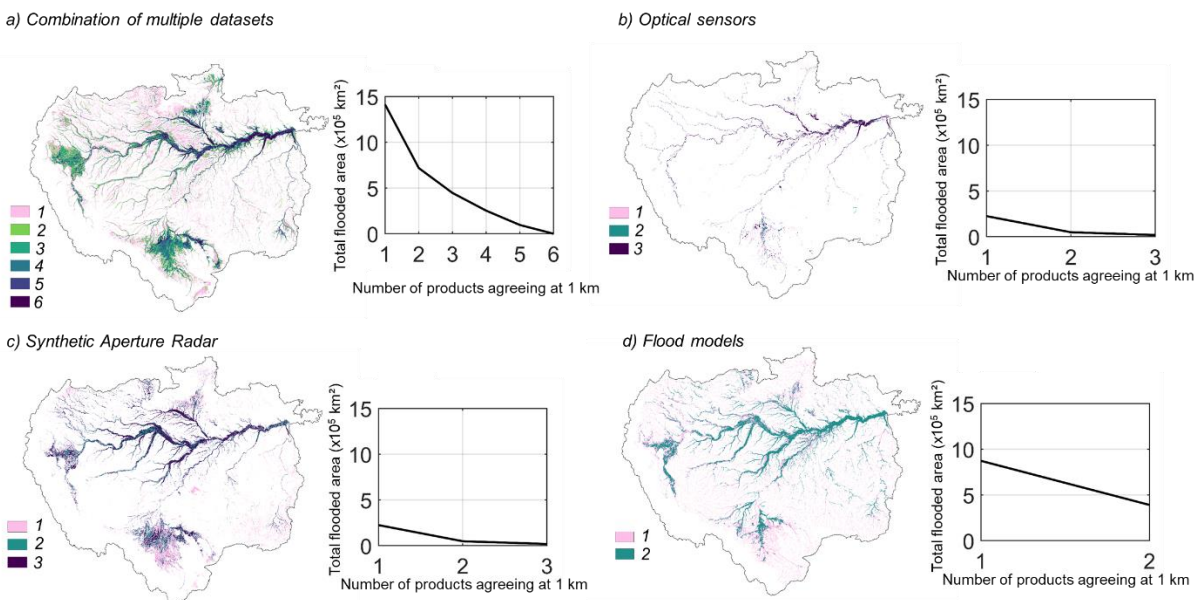
### 819 3.5 Limitations in comparing the inundation area datasets

820 Some of the differences in large-scale inundation mapping highlighted by our comparison occur  
 821 because distinct datasets map temporal variation in inundation in different ways, varying for  
 822 example in sensor type, post processing, and spatial resolution. Figure 11 shows the agreement  
 823 maps for maximum inundation for four classes of datasets, considering the 14 basin-scale high-



824 resolution datasets. Those based on multiple datasets (GLWD, CIFOR, GIEMS-D3, GIEMS-D15,  
 825 SWAF-HR) have the best agreement for the Llanos de Moxos area, and to a smaller degree, for  
 826 Pacaya-Samiria, Negro and Roraima wetlands. The L-band SAR datasets have less overall  
 827 agreement (Figure 11c), while the optical data are mainly applicable to open water areas in the  
 828 Amazon mainstem floodplain (Figure 11b). The 1D hydrological models cannot represent  
 829 interfluvial wetlands where flooding is not controlled by river level and discharge (Figure 11d).

830



831

832 Figure 11. Amazon basin (< 500 m elevation) agreement maps at 1 km resolution, for maximum inundation and for  
 833 each type of dataset, considering only the high-resolution datasets ( $\leq 1 \text{ km}$  spatial resolution): (a) six datasets based  
 834 on merging of multiple datasets (GLWD, CIFOR, GIEMS-D3, GIEMS-D15, SWAF-HR, ESA-CCI), (b) three datasets  
 835 based on optical sensors (G3WBM, GLAD, GSWO), (c) three datasets based on synthetic aperture radar (Hess,  
 836 Chapman, Rosenqvist), and (d) two hydrological models (MGB and CaMa-Flood). The right column graphs present  
 837 the total inundation area in the Amazon basin for a given number of datasets agreeing, e.g., the basin area where the  
 838 two hydrological models (Fig. d) agree to be flooded is 390,900  $\text{km}^2$ .

839 The different methodologies used to produce each dataset complicate their direct comparison  
840 (Rosenqvist et al., 2020), and some methodological differences produce systematic differences and  
841 bias among the data sources included in our comparison. Here we used datasets covering long-  
842 term dynamics (e.g., GIEMS or hydrologic models), short-term dual-season (e.g., Rosenqvist,  
843 spanning four years), and a particular year (e.g., Hess). Some datasets use alternative approaches  
844 to derive long-term maximum inundation area, such as GIEMS-D15, which generated estimates  
845 by merging 3-year moving-window maximum values of GIEMS with the GLWD dataset.  
846 Therefore, a comparison of all these datasets must be performed with consideration of their  
847 methodology. For instance, the comparison of dual-season datasets against monthly datasets can  
848 yield erroneous conclusions, although it has been a common practice to directly compare such  
849 datasets. Some datasets also consider a “high-water assumption” (Ferreira-Ferreira et al., 2015;  
850 Hess et al., 2003), whereby the high-water maps are forced to contain all flooded pixels from the  
851 low-water map.

852 In addition to methodological differences, each dataset was developed for different periods (Table  
853 1), and thus interannual and seasonal variability accounts for some of the differences among them.  
854 To address this, we performed an annual analysis (Figure 5), which suggests that the long-term  
855 inundation estimate is fairly stable for each dataset despite some interannual differences. In fact,  
856 the temporal variability of each dataset is generally smaller than the differences in comparison  
857 with the other estimates. However, the Amazon hydrological cycle has been shifting over decades  
858 (Barichivich et al., 2018; Gloor et al., 2013), and a recent increase in maximum water levels in the  
859 central Amazon suggests a new hydroclimatic state (Espinoza et al., 2019). Some wetlands have  
860 also been subject to forest loss, and so the detectability of inundation by remote sensing may have  
861 increased over time, e.g., major deforestation has occurred along the lower Amazon River

862 floodplain (Renó et al., 2011). Similarly, widespread burning might be converting black-water  
863 floodplain forests into savanna vegetation (Flores and Holmgren, 2021). In addition, in some  
864 regions, such as the southern Amazon, an increase in the dry-season length has been observed,  
865 which is a major climatic constraint for forest sustainability (Fu et al. 2013; Staver et al., 2011).  
866 However, analyzing long-term change in inundation patterns is beyond the scope of this study, and  
867 thus we assumed stationarity in our comparison framework.

868 Another important challenge is to find a common definition of wetlands among datasets. Here we  
869 focused on inundation extent, however some datasets (e.g., CIFOR) represent peatland locations  
870 instead of inundated areas, although their areas of peat formation often include inundated areas.  
871 Estimates based on SAR or passive microwave emission may also be sensitive to saturated soil  
872 without standing water above it, and thus the observed inundation estimates can have some  
873 ambiguity. Hydrologic models provide simulated surface water extent, and we mapped inundation  
874 accounting for pixels with water depth greater than zero. While hydrologic models have  
875 uncertainties related to model structure (e.g., inadequate representation of inundation processes),  
876 input data (e.g., DEM and climate forcing) and parameterization (e.g., soil water capacity and river  
877 channel width and depth; assumptions of level water surfaces between rivers and their floodplains),  
878 remote sensing-based datasets have uncertainties related to spatial and temporal resolutions (e.g.,  
879 coarse spatial resolution not capable of detecting small patches), and detection uncertainty (e.g.,  
880 dense vegetation canopies can obscure passive microwave emission from underlying surfaces).  
881 Thus, a comparative framework provides an opportunity to highlight and stress the uncertainties  
882 and limitations of each dataset.

883 Hydrologic models currently available at the Amazon basin scale are one-dimensional, and thus  
884 are capable of simulating flooding mainly along river floodplains, as corroborated by various

885 validation exercises in the Amazon that have relied on the Hess, GIEMS and SWAF-HR datasets  
886 (Fleischmann et al., 2020; Luo et al., 2017; Paiva et al., 2013; Zhou et al., 2021). These models  
887 are also largely dependent upon accurate DEMs, which are still challenging to obtain over tropical  
888 forested floodplains. Furthermore, given that a 500 m elevation mask (Amazon lowlands) has been  
889 used for some SAR datasets (Hess et al., 2015), and the difficulty of some radar and passive  
890 microwave ones to detect inundation at high elevations due to slope and snow effects, for instance  
891 (Parrens et al., 2017), we have adopted the same 500 m threshold in our lowland mask to improve  
892 the comparability among datasets. However, even though higher elevation wetlands amount to  
893 much less total area compared to lowland wetlands, understanding their flooding dynamics is  
894 important for some parts of the Amazon basin. Although some datasets, especially the hydrological  
895 models (MGB, CaMa-Flood and THMB), are capable of estimating inundation in higher elevation  
896 parts of the basin, in this case uncertainties may also be large given errors in precipitation (low  
897 density of in situ gauges and high rainfall spatial heterogeneity) and thus runoff fields over  
898 mountainous areas, as well as the tendency for river flows to vary over short time scales (Espinoza  
899 Villar et al., 2009; Zubieta et al., 2015). Furthermore, the availability of in situ river discharge  
900 measurements for model calibration and validation is lower in the Andean Amazon (Feng et al.,  
901 2020; Wongchuig et al., 2019; Zubieta et al., 2017).

902 Our analyses were performed at 1 km resolution and at regional scales, which avoids geolocation  
903 problems that affect analyses at higher resolutions (e.g., 30 or 90 m). Small disagreements among  
904 our estimates and the values presented in the original publications may also arise from the use of  
905 the WGS84 datum with a geographical coordinate system for all datasets (except for SWAMPS  
906 which was provided in the EASE-Grid format). Also, the coarse-resolution datasets, especially  
907 GIEMS-2 and SWAMPS with 25 km spatial resolution, can be difficult to compare with estimates

908 for individual wetland complexes (e.g., Curuai and Janauacá), since only a few 25-km pixels may  
909 be located within the wetland boundaries.

910 The quantification of inundation over larger river floodplains (Figure 10) is also subject to  
911 uncertainties. The maximum floodplain lateral extent was estimated based on an automatic buffer  
912 procedure around the Hydrosheds drainage network, further manually edited by considering the  
913 three SAR-based, basin-scale datasets and the MERIT DEM-based topography. Although it  
914 captures the basin-scale geomorphological differences along major floodplains, some uncertainties  
915 remain regarding the true lateral extent for areas where rain-fed savanna floodplains are present  
916 (e.g., Llanos de Moxos, Roraima), and where flooding extend far from the main rivers (e.g.,  
917 Pacaya-Samiria). For these areas in particular, we assumed buffer values similar to adjacent  
918 upstream and downstream floodplains (e.g., the Amazon River downstream of Pacaya-Samiria),  
919 which is reasonable but should undergo future scrutiny, including local ground-based surveys.

920

#### 921 **4. Perspectives and recommendations**

922 Considerable advances have been achieved in recent decades in the mapping of inundation extent  
923 across the Amazon basin. Here, we have presented an analysis of 29 inundation datasets for the  
924 basin, covering multiple scales, spatial and temporal resolutions, and data sources. We showed  
925 that large discrepancies persist, and this is especially true at local scales. Below we present some  
926 perspectives and recommendations for future development of inundation mapping in the world's  
927 largest river basin.

928

929 *4.1 Which are the most reliable data sources for inundation mapping in the Amazon River*  
930 *basin?*

931 At basin scale, the Rosenqvist ALOS-2 PALSAR-2 dataset is available at 50 m, and shows a good  
932 overall agreement with the 90 m Hess one over the large river floodplains, while the latter seems  
933 more accurate for interfluvial savanna floodplains (e.g., Negro and Roraima). The high agreement  
934 is observed mainly for the maximum inundation estimates, while for the minimum inundation area,  
935 important disagreements persist and more studies should be performed to understand them.  
936 Overall, the Hess' dataset has been the Amazon inundation benchmark for many years, and still  
937 provides satisfactory estimates. Detection of inundation by L-band SAR has a sound theoretical  
938 and empirical basis that has been validated for the Amazon (Rosenqvist et al., 2002; Hess et al.,  
939 2003). Optical datasets with resolution higher than 30 m are available, but detection of inundation  
940 is restricted to non-vegetated wetlands and clear-sky periods, and is most applicable in the lower  
941 Amazon River floodplains. ALOS-PALSAR at 12.5 m resolution and Sentinel SAR at 10 m  
942 resolution (with C-band and limited vegetation penetration) can be applied to specific regions.  
943 Time series of these datasets can estimate seasonal variations in inundation, but are limited by the  
944 length of the acquisitions. Weekly to monthly, spatially coarser data (25 km) are available from  
945 passive microwave-based datasets such as GIEMS, SWAF and SWAMPS. Downscaling  
946 techniques have improved their spatial resolution to 90 m (GIEMS-D3) and 1 km (SWAF-HR).  
947 Hydrological models (e.g., CaMa-Flood and MGB) are capable of accurately estimating  
948 inundation over river floodplains, and at high temporal resolution depending on the input rainfall  
949 data (e.g., hourly to daily). However, they are still limited over interfluvial wetlands with less

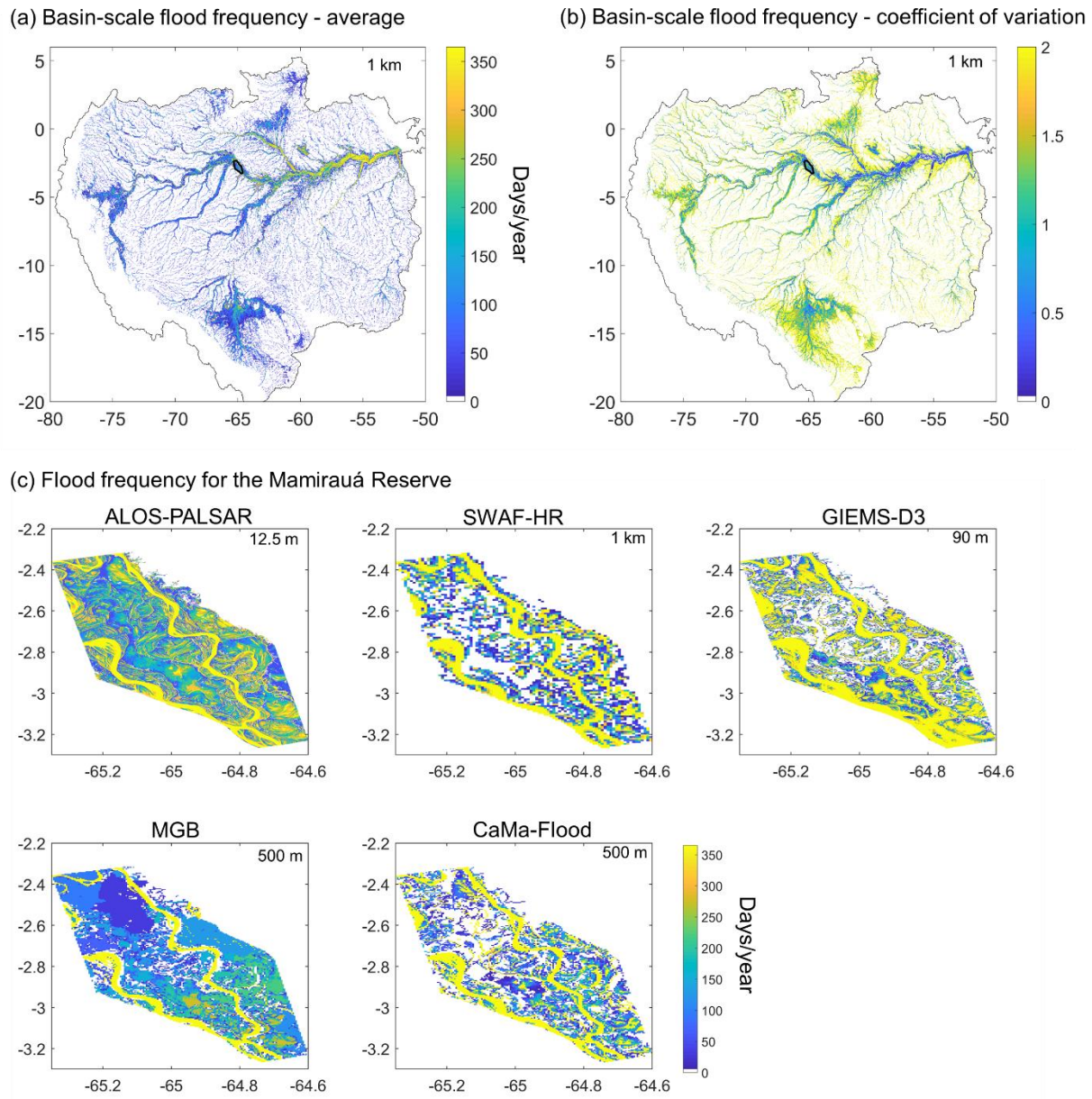
950 connection with rivers, unless they are upgraded for simulating 2D inundation processes and  
951 complex floodplain flow paths (Fleischmann et al., 2020; Yamazaki et al., 2014).

952

#### 953 ***4.2 What are the current capabilities of flood frequency mapping?***

954 At the basin scale, high-resolution, long-term average flood frequency can be estimated by four of  
955 the datasets analyzed here (GIEMS-D3, SWAF-HR, MGB and CaMa-Flood), with spatial  
956 resolutions ranging from 90 m to 1 km. Although multiple SAR data are currently available (e.g.,  
957 Sentinel-1, ALOS-PALSAR and ALOS-2 PALSAR-2), they have a limited temporal resolution,  
958 and we still do not have a flood frequency dataset of higher spatial resolution (i.e., better than 90  
959 m) for the whole basin based on SAR. The discrepancies among the available datasets are notable  
960 (Figure 12). The average of the basin-scale flood frequency shows a higher agreement for areas  
961 with high flood frequency along the lower Amazon River (Figure 12a). These are associated with  
962 a high proportion of open water areas, and have lower uncertainty (Figure 12b). Generally, there  
963 is a smaller variation along floodplains bordering the major rivers (except for their fringes) than in  
964 interfluvial areas, especially in the Negro and Roraima wetlands (Figure 12b). Detailed inundation  
965 mapping for the Mamirauá Sustainable Development Reserve in the Amazon mainstem floodplain  
966 (Figure 12c) reinforces the challenges for mapping local spatio-temporal inundation dynamics.  
967 The northern part of the Mamirauá reserve has a shorter flood frequency in all datasets, while three  
968 of them (SWAF-HR, GIEMS-D3, CaMa-Flood) estimate that large portions are never flooded. For  
969 the southern part, there is some convergence for areas that are frequently flooded.

970



971

972 Figure 12. Analysis of flood frequency for (a) basin-scale average and (b) coefficient of variation of the long-term  
 973 flood frequency estimated from four high-resolution dynamic datasets (GIEMS-D3, SWAF-HR, CaMa-Flood and  
 974 MGB). (c) The four basin-scale datasets are compared to a subregional validation dataset (i.e., the ALOS-PALSAR-  
 975 based classification by Ferreira-Ferreira et al. (2015), displayed in the top left panel) for the Mamirauá Sustainable  
 976 Development Reserve along the central Amazon River mainstem (location shown by black outline in figure a).

977



978 ***4.3 Implications for biogeochemistry, ecology and flood management***

979 The divergent estimates of Amazon inundation extent have major implications for the  
980 quantification of the role of wetlands in global biogeochemical cycles, ecosystem processes and  
981 natural disaster management.

982 First, different datasets have been used to quantify the role of Amazon wetlands in the carbon cycle  
983 (Guilhen et al., 2020; Melack et al., 2004; Richey et al., 2002; Saunois et al., 2020). An  
984 intercomparison assessment of global models forced with different inundation datasets for the  
985 Amazon could provide insights into their sensitivity to the estimated inundation. This would be  
986 particularly important for modeled estimates of methane flux, given the region's significant  
987 contribution to global methane emissions from natural wetlands (Basso et al., 2021). Furthermore,  
988 for a proper estimation of methane and carbon dioxide fluxes, dynamic inundation estimates are  
989 necessary; this study shows that most coarse-resolution dynamic datasets capture relatively well  
990 the seasonality (i.e., the timing of high and low water periods) of annual flooding at a large scale  
991 (but not at the local scales), but the magnitude of inundation area over time is still associated with  
992 significant errors (Fig. S6).

993 The understanding of the ecology of Amazon freshwaters has benefited from advances in remote  
994 sensing-based mapping of inundation. Hydrological variables of interest in relation to wildlife  
995 (Alvarenga et al., 2018; Bodmer et al., 2018) and vegetation distribution (Hess et al., 2015, 2003)  
996 include hydroperiod, floodplain water depth (Arantes et al., 2013; Fassoni-Andrade et al., 2020),  
997 and (lateral) surface water connectivity (Castello, 2008; Duponchelle et al., 2021; Reis et al.,  
998 2019a, 2019b), and should be better estimated by future datasets. In addition, many wetland  
999 ecosystem studies are performed at the tree stand level (e.g., floristic inventories) and require high

1000 spatial resolution inundation estimates to perform meaningful spatial analyses accounting for  
1001 spatial heterogeneity of wetland vegetation. Furthermore, besides a simple interfluvial/floodplain  
1002 categorization of wetlands as performed here (section 3.4), which is reasonable from a hydrologic  
1003 perspective, improving our understanding of the ecology of Amazon freshwater systems requires  
1004 accurate mapping of habitats and their diverse vegetation types (e.g., grasslands, particular  
1005 monodominant tree species, herbaceous plants). For instance, floodplain forest cover has been  
1006 positively correlated to fishery yields (Arantes et al., 2018) and fish abundance (Lobón-Cerviá et  
1007 al., 2015). While this wetland habitat mapping has already been done by some initiatives at the  
1008 basin (Hess et al., 2015, 2003) and subregional scales (Ferreira-Ferreira et al., 2015; Silva et al.,  
1009 2013), there is still a need for higher resolution and dynamic datasets.

1010 Regarding flood monitoring in the context of natural hazard management, the flood warning  
1011 systems of regional water authorities in the basin provide information based on river discharge and  
1012 water level at monitoring stations (e.g., Brazil's Geological Survey SACE system;  
1013 <<http://sace.cprm.gov.br/amazonas/#>>). In addition, there are other available monitoring and  
1014 forecasting services that have been developed for the global scale, such as the Global Flood  
1015 Detection System (<https://www.gdacs.org/flooddetection/>), based on remote sensing, and the  
1016 Global Flood Monitoring System (<http://flood.umd.edu/>) and the Global Flood Awareness System  
1017 (<https://www.globalfloods.eu/>), based on hydrological modeling. The currently available, basin-  
1018 scale inundation datasets are unable to map flood hazard at the detailed resolution required for  
1019 flood management applications, especially concerning urban areas (Almeida et al., 2018). High-  
1020 resolution flood mapping has been achieved using hydraulic modeling based on local surveys of  
1021 river bathymetry and floodplain LiDAR DTM, but only for a few specific sites such as the lower  
1022 Madeira River (Fleischmann et al., 2021).

1023

1024 *4.4 Future opportunities and recommendations*

1025 Future satellite missions will provide opportunities for improved inundation mapping in the  
1026 Amazon, especially the polarimetric and interferometric L-band SAR data from the upcoming  
1027 NASA/ISRO mission (NISAR), the P-Band BIOMASS mission from ESA, and the Ka-band Radar  
1028 Interferometer (KaRIn) swath observations from the forthcoming SWOT mission (Biancamaria et  
1029 al., 2016). New inundation detection technology under development with Global Navigation  
1030 Satellite System-Reflectometry (GNSS-R), such as the Cyclone GNSS (CYGNSS) constellation  
1031 of GNSS-R satellites, holds promise to provide higher frequency observations of water level  
1032 changes (Jensen et al., 2018; Ruf et al., 2018; Rodriguez-Alvarez et al., 2019). Further studies with  
1033 the ALOS-2 PALSAR-2 data also are promising, in order to achieve new dynamic inundation  
1034 detection, as well as ongoing assessments of the accuracy of the newly available high temporal  
1035 resolution inundation datasets (e.g., SWAF-HR with 3-day availability). Consistent and updated  
1036 validation products of Amazon inundation are required, which could be derived from airborne,  
1037 satellite, or UAV-based LiDAR surveys along multiple wetlands, in particular for overlooked  
1038 wetlands such as the Negro and Roraima floodable savannas where measured water levels in rivers  
1039 may not adequately predict inundation area. This is especially important for the minimum  
1040 inundation extent, which showed large uncertainties among the multiple datasets.

1041 Comprehensive comparisons among multiple inundation datasets are scarce in the literature, yet  
1042 are valuable ways to understand benefits and limitations of each of them. A few examples include  
1043 a continental-scale assessment of flood model hazard maps in Africa (Trigg et al., 2016) and  
1044 regional assessment of inundation in floodplains of Nigeria and Mozambique (Bernhofen et al.,  
1045 2018), both based on global hydrological models. Similar initiatives for other areas worldwide

1046 would be welcome, especially for those that lack consistent flood mapping, such as the Congo and  
1047 other large wetland systems in Africa (Papa et al., 2022). Furthermore, the combination and  
1048 integration of multiple inundation datasets present a promising and effective approach (Gumbrecht  
1049 et al., 2017; Hu et al., 2017). We recommend that future developments include optimal data  
1050 merging approaches, e.g., by integrating inundation extent into models accounting for water cycle  
1051 components with multiple constraints (Meyer Oliveira et al, 2020; Pellet et al., 2021), and by  
1052 considering new types of datasets (e.g., GNSS-R; Jensen et al., 2018). Bias of different datasets  
1053 could be corrected based on intercomparisons such as those we present here. For instance, recent  
1054 studies have performed inundation bias correction using the Hess dataset (Aires et al., 2013;  
1055 Sorribas et al., 2016). However, merging of different datasets must be performed with caution, in  
1056 a consistent way, avoiding double counting of surfaces, as well as missing others: its success  
1057 critically depends upon a good understanding of the limitations and assets of each individual  
1058 dataset. The optimal combination of hydrological-hydraulic models with satellite flood maps using  
1059 techniques such as data assimilation is also a promising alternative at the basin scale (Wongchuig  
1060 et al., 2020).

1061 There is a need for the development of more large-scale 2D hydrological model applications,  
1062 especially for large wetland complexes such as the Llanos de Moxos and Pacaya-Samiria, to better  
1063 represent inundation dynamics (Fleischmann et al., 2020). 2D models have been applied mainly  
1064 to some local-scale areas in the Amazon mainstem floodplain (Pinel et al., 2019; Rudorff et al.,  
1065 2014; Trigg et al., 2009; Wilson et al., 2007). Furthermore, inundation anomalies are still poorly  
1066 understood owing to the lack of ground-based inundation observations during extreme floods and  
1067 droughts. Therefore, validation of estimates for extreme years has usually been performed with  
1068 river water level data (in situ or from satellite altimetry) (Silva et al., 2018; Wongchuig et al.,

1069 2019). Future works should address which datasets and methodologies are the most suitable for  
1070 mapping extreme events. Furthermore, besides inundation extent, flood storage (Frappart et al.,  
1071 2005; Papa et al., 2008; Schumann et al., 2016; Papa and Frappart, 2021) and water velocity (Pinel  
1072 et al., 2019) are necessary hydraulic variables to properly address multiple environmental studies  
1073 (e.g., flood monitoring, flood attenuation by floodplains, fish floodplain habitats), but to date have  
1074 not been well studied in the Amazon.

1075 Finally, there is a need for better-informed usage of the currently available inundation datasets by  
1076 multiple local and regional stakeholders (e.g., local water authorities, national water agencies), as  
1077 well as research communities not close to remote sensing groups. This will only be achieved  
1078 through a two-way interaction with these actors and development of easy-to-access visualization  
1079 platforms (i.e., investment in hydroinformatics), as well as training of regional/local user  
1080 communities. To this end, we have developed a WebGIS platform ([https://amazon-  
1081 inundation.herokuapp.com/](https://amazon-inundation.herokuapp.com/)) to display and provide data acquisition links for the inundation  
1082 datasets assessed here, which will be continuously updated once new datasets are made available.  
1083 The interaction with local users would bring important feedback on the large-scale datasets as well,  
1084 for instance through citizen science initiatives that are ongoing in the Amazon  
1085 (<https://www.amazoniacienciaciudadana.org/>).

1086

1087

## 1088 **Acknowledgments**

1089 The authors thank Dr. Fernando Jaramillo, Dr. David Kaplan, Dr. David Marques and Dr. Naziano  
1090 Filizola for fruitful comments in an earlier version of this manuscript. The work was part of the  
1091 SABERES project financed by the BNPParibas Foundation as part of its "Climate & Biodiversity

1092 Initiative" program 2019. A.S.F. was supported by CNPq (Conselho Nacional de Desenvolvimento  
1093 Científico e Tecnológico, Brazil) [grant number 141161/2017-5]. F.P., J.F.F., M.P.B. and F.A.  
1094 received support from CNES (SWOT-ST project SWOT for SOUTH AMERICA, ID: 6018-  
1095 4500066497). F.P. and M.P.B. also received support from CNES (SWOT-ST project SWOT  
1096 Wetlands Hydrology Monitoring). F.P. is supported by the IRD Groupement De Recherche  
1097 International (GDRI) SCaHyLab. J.M.M. received support from NASA IDS grant NNX17AK49G  
1098 and the US National Science Foundation (Division of Environmental Biology, grant 1753856).  
1099 E.P. acknowledges Nanyang Technological University (SUG-NAP EP3/19) and Ministry of  
1100 Education of Singapore (AcRF Tier1 RT 06/19 and AcRF Tier2 RT 11/21). A.F.R. acknowledges  
1101 the Research Foundation of São Paulo (FAPESP, grant #2019/24049-5). S.W. has been supported  
1102 by the French AMANECER-MOPGA project funded by ANR and IRD (ref. ANR-18-MPGA-  
1103 0008). M.C. received funding from NASA IDS grant NNX17AK49G. The SWAF dataset  
1104 development was financed by the CATDS and the SWOT-AVAL programs by CNES.

1105

## 1106 **References**

- 1107 Abril, G., Martinez, J.M., Artigas, L.F., Moreira-Turcq, P., Benedetti, M.F., Vidal, L., Meziane,  
1108 T., Kim, J.-H., Bernardes, M.C., Savoye, N., Deborde, J., Souza, E.L., Albéric, P., Landim  
1109 de Souza, M.F., Roland, F., 2014. Amazon River carbon dioxide outgassing fuelled by  
1110 wetlands. *Nature* 505, 395–398. <https://doi.org/10.1038/nature12797>
- 1111 Aires, F., Miolane, L., Prigent, C., Pham, B., Fluet-Chouinard, E., Lehner, B., Papa, F., 2017. A  
1112 Global Dynamic Long-Term Inundation Extent Dataset at High Spatial Resolution Derived  
1113 through Downscaling of Satellite Observations. *J. Hydrometeorol.* 18, 1305–1325.

1114 <https://doi.org/10.1175/JHM-D-16-0155.1>

1115 Aires, F., Papa, F., Prigent, C., 2013. A Long-Term, High-Resolution Wetland Dataset over the  
1116 Amazon Basin, Downscaled from a Multiwavelength Retrieval Using SAR Data. *J.*  
1117 *Hydrometeorol.* 14, 594–607. <https://doi.org/10.1175/JHM-D-12-093.1>

1118 Aires, F., Prigent, C., Fluet-Chouinard, E., Yamazaki, D., Papa, F., Lehner, B., 2018.  
1119 Comparison of visible and multi-satellite global inundation datasets at high-spatial  
1120 resolution. *Remote Sens. Environ.* 216, 427–441. <https://doi.org/10.1016/j.rse.2018.06.015>

1121 Al Bitar, A., Parrens, M., Fatras, C., Luque, S. P., 2020. Global Weekly Inland Surface Water  
1122 Dynamics from L-Band Microwave. In *IGARSS 2020-2020 IEEE International Geoscience*  
1123 *and Remote Sensing Symposium*, 5089-5092.

1124 Alsdorf, D., Bates, P., Melack, J., Wilson, M., Dunne, T., 2007. Spatial and temporal complexity  
1125 of the Amazon flood measured from space. *Geophys. Res. Lett.* 34.  
1126 <https://doi.org/10.1029/2007GL029447>

1127 Alvarenga, G.C., Ramalho, E.E., Baccaro, F.B., da Rocha, D.G., Ferreira-Ferreira, J., Dineli  
1128 Bobrowiec, P.E., 2018. Spatial patterns of medium and large size mammal assemblages in  
1129 várzea and terra firme forests, Central Amazonia, Brazil. *PLoS One* 13, 1–19.  
1130 <https://doi.org/10.1371/journal.pone.0198120>

1131 Andrade, M.M.N. de, Bandeira, I.C.N., Fonseca, D.D.F., Bezerra, P.E.S., Andrade, Á. de S.,  
1132 Oliveira, R.S. de, 2017. Flood Risk Mapping in the Amazon, in: *Flood Risk Management.*  
1133 *InTech*, p. 13. <https://doi.org/10.5772/intechopen.68912>

- 1134 Arantes, C.C., Castello, L., Cetra, M., Schilling, A., 2013. Environmental influences on the  
1135 distribution of arapaima in Amazon floodplains. *Environ. Biol. Fishes* 96, 1257–1267.  
1136 <https://doi.org/10.1007/s10641-011-9917-9>
- 1137 Arantes, C.C., Winemiller, K.O., Petrere, M., Castello, L., Hess, L.L., Freitas, C.E.C., 2018.  
1138 Relationships between forest cover and fish diversity in the Amazon River floodplain. *J.*  
1139 *Appl. Ecol.* 55, 386–395. <https://doi.org/10.1111/1365-2664.12967>
- 1140 Armijos, E., Crave, A., Espinoza, J.C., Filizola, N., Espinoza-Villar, R., Ayes, Fonseca, P.,  
1141 Fraizy, P., Gutierrez, O., Vauchel, P., Camenen, B., Martinez, J.M., Dos Santos, A.,  
1142 Santini, W., Cochonneau, G., Guyot, J.L., 2020. Rainfall control on Amazon sediment flux:  
1143 synthesis from 20 years of monitoring. *Environ. Res. Commun.* 2, 051008.  
1144 <https://doi.org/10.1088/2515-7620/ab9003>
- 1145 Arnesen, A.S., Silva, T.S.F., Hess, L.L., Novo, E.M.L.M., Rudorff, C.M., Chapman, B.D.,  
1146 McDonald, K.C., 2013. Monitoring flood extent in the lower Amazon River floodplain  
1147 using ALOS/PALSAR ScanSAR images. *Remote Sens. Environ.* 130, 51–61.  
1148 <https://doi.org/10.1016/j.rse.2012.10.035>
- 1149 Asner, G.P., 2001. Cloud cover in Landsat observations of the Brazilian Amazon. *Int. J. Remote*  
1150 *Sens.* 22, 3855–3862. <https://doi.org/10.1080/01431160010006926>
- 1151 Balsamo, G., Beljaars, A., Scipal, K., Viterbo, P., van den Hurk, B., Hirschi, M., and Betts, A.  
1152 K.: A Revised Hydrology for the ECMWF Model: Verification from Field Site to  
1153 Terrestrial Water Storage and Impact in the Integrated Forecast System, *J. Hydrometeorol.*,  
1154 10, 623–643, <https://doi.org/10.1175/2008jhm1068.1>, 2009.



- 1155 Barichivich, J., Gloor, E., Peylin, P., Brienen, R.J.W., Schöngart, J., Espinoza, J.C., Pattnayak,  
1156 K.C., 2018. Recent intensification of Amazon flooding extremes driven by strengthened  
1157 Walker circulation. *Sci. Adv.* 4. <https://doi.org/10.1126/sciadv.aat8785>
- 1158 Basso, L.S., Marani, L., Gatti, L. V., Miller, J.B., Gloor, M., Melack, J., Cassol, H.L.G., Tejada,  
1159 G., Domingues, L.G., Arai, E., Sanchez, A.H., Corrêa, S.M., Anderson, L., Aragão,  
1160 L.E.O.C., Correia, C.S.C., Crispim, S.P., Neves, R.A.L., 2021. Amazon methane budget  
1161 derived from multi-year airborne observations highlights regional variations in emissions.  
1162 *Commun. Earth Environ.* 2, 1–14. <https://doi.org/10.1038/s43247-021-00314-4>
- 1163 Batalha, M.A., Cianciaruso, M. V., Silva, I.A., Delitti, W.B.C., 2005. Hyperseasonal cerrado, a  
1164 new brazilian vegetation form. *Brazilian J. Biol.* 65, 735–738.  
1165 <https://doi.org/10.1590/S1519-69842005000400021>
- 1166 Bates, P.D., De Roo, A.P.J., 2000. A simple raster-based model for flood inundation simulation.  
1167 *J. Hydrol.* [https://doi.org/10.1016/S0022-1694\(00\)00278-X](https://doi.org/10.1016/S0022-1694(00)00278-X)
- 1168 Beck, H.E., Van Dijk, A.I.J.M., Levizzani, V., Schellekens, J., Miralles, D.G., Martens, B., De  
1169 Roo, A., 2017. MSWEP: 3-hourly 0.25° global gridded precipitation (1979-2015) by  
1170 merging gauge, satellite, and reanalysis data. *Hydrol. Earth Syst. Sci.*  
1171 <https://doi.org/10.5194/hess-21-589-2017>
- 1172 Beighley, R.E., Eggert, K.G., Dunne, T., He, Y., Gummadi, V., Verdin, K.L., 2009. Simulating  
1173 hydrologic and hydraulic processes throughout the Amazon River Basin. *Hydrol. Process.*  
1174 23, 1221–1235. <https://doi.org/10.1002/hyp.7252>
- 1175 Belger, L., Forsberg, B. R. Melack, J. M., 2011. Carbon dioxide and methane emissions from

1176 interfluvial wetlands in the upper Negro River basin, Brazil. *Biogeochemistry* 105, 171–  
1177 183. <https://doi.org/10.1007/s10533-010-9536-0>

1178 Bernhofen, M. V, Whyman, C., Trigg, M.A., Sleigh, P.A., Smith, A.M., Sampson, C.C.,  
1179 Yamazaki, D., Ward, P.J., Rudari, R., Pappenberger, F., Dottori, F., Salamon, P.,  
1180 Winsemius, H.C., 2018. A first collective validation of global fluvial flood models for  
1181 major floods in Nigeria and Mozambique. *Environ. Res. Lett.* 13, 104007.  
1182 <https://doi.org/10.1088/1748-9326/aae014>

1183 Biancamaria, S., Lettenmaier, D. P., Pavelsky, T. M, 2016. The SWOT Mission and Its  
1184 Capabilities for Land Hydrology. *Surv. Geophys.* 37, 307–337.  
1185 <https://doi.org/10.1007/s10712-015-9346-y>

1186 Blatrix, R., Roux, B., Béarez, P., Prestes-Carneiro, G., Amaya, M., Aramayo, J.L., Rodrigues, L.,  
1187 Lombardo, U., Iriarte, J., De Souza, J.G., Robinson, M., Bernard, C., Pouilly, M., Durécu,  
1188 M., Huchzermeyer, C.F., Kalebe, M., Ovando, A., McKey, D., 2018. The unique  
1189 functioning of a pre-Columbian Amazonian floodplain fishery. *Sci. Rep.* 8.  
1190 <https://doi.org/10.1038/s41598-018-24454-4>

1191 Bodmer, R., Mayor, P., Antunez, M., Chota, K., Fang, T., Puertas, P., Pittet, M., Kirkland, M.,  
1192 Walkey, M., Rios, C., Perez-Peña, P., Henderson, P., Bodmer, W., Bicerra, A., Zegarra, J.,  
1193 Docherty, E., 2018. Major shifts in Amazon wildlife populations from recent intensification  
1194 of floods and drought. *Conserv. Biol.* 32, 333–344. <https://doi.org/10.1111/cobi.12993>

1195 Bonnet, M.P., Barroux, G., Martinez, J.M., Seyler, F., Moreira-Turcq, P., Cochonneau, G.,  
1196 Melack, J.M., Boaventura, G., Maurice-Bourgoin, L., León, J.G., Roux, E., Calmant, S.,

- 1197 Kosuth, P., Guyot, J.L., Seyler, P., 2008. Floodplain hydrology in an Amazon floodplain  
1198 lake (Lago Grande de Curuaí). *J. Hydrol.* 349, 18–30.  
1199 <https://doi.org/10.1016/j.jhydrol.2007.10.055>
- 1200 Bonnet, M.P., Pinel, S., Garnier, J., Bois, J., Resende Boaventura, G., Seyler, P., Motta Marques,  
1201 D., 2017. Amazonian floodplain water balance based on modelling and analyses of  
1202 hydrologic and electrical conductivity data. *Hydrol. Process.* 31, 1702–1718.  
1203 <https://doi.org/10.1002/hyp.11138>
- 1204 Bontemps, S., Defourny, P., Radoux, J., Van Bogaert, E. Lamarche, C., Achard, F., Mayaux, P.,  
1205 Boettcher, M., Brockmann, C., Kirches, G., 2013. Consistent global land cover maps for  
1206 climate modelling communities: current achievements of the ESA’s land cover CCI, in:  
1207 Proceedings of the ESA Living Planet Symposium. Edinburgh.
- 1208 Bourgoin, L.M., Bonnet, M.P., Martinez, J.M., Kosuth, P., Cochonneau, G., Moreira-Turcq, P.,  
1209 Guyot, J.L., Vauchel, P., Filizola, N., Seyler, P., 2007. Temporal dynamics of water and  
1210 sediment exchanges between the Curuaí floodplain and the Amazon River, Brazil. *J.*  
1211 *Hydrol.* 335, 140–156. <https://doi.org/10.1016/j.jhydrol.2006.11.023>
- 1212 Canisius, F., Brisco, B., Murnaghan, K., Van Der Kooij, M., Keizer, E., 2019. SAR backscatter  
1213 and InSAR coherence for monitoring wetland extent, flood pulse and vegetation: A study of  
1214 the Amazon lowland. *Remote Sens.* 11, 1–18. <https://doi.org/10.3390/RS11060720>
- 1215 Castello, L., 2008. Lateral migration of *Arapaima gigas* in floodplains of the Amazon. *Ecol.*  
1216 *Freshw. Fish* 17, 38–46. <https://doi.org/10.1111/j.1600-0633.2007.00255.x>
- 1217 Chapman, B., McDonald, K., Shimada, M., Rosenqvist, A., Schroeder, R., Hess, L., 2015.

- 1218 Mapping Regional Inundation with Spaceborne L-Band SAR. *Remote Sens.* 7, 5440–5470.  
1219 <https://doi.org/10.3390/rs70505440>
- 1220 Coe, M.T., Costa, M.H., Howard, E.A., 2008. Simulating the surface waters of the Amazon  
1221 River basin: impacts of new river geomorphic and flow parameterizations. *Hydrol. Process.*  
1222 22, 2542–2553. <https://doi.org/10.1002/hyp.6850>
- 1223 Coomes, O.T., Lapointe, M., Templeton, M., List, G., 2016. Amazon river flow regime and flood  
1224 recession agriculture: Flood stage reversals and risk of annual crop loss. *J. Hydrol.* 539,  
1225 214–222. <https://doi.org/10.1016/j.jhydrol.2016.05.027>
- 1226 Coomes, O.T., Takasaki, Y., Abizaid, C., Barham, B.L., 2010. Floodplain fisheries as natural  
1227 insurance for the rural poor in tropical forest environments: Evidence from Amazonia. *Fish.*  
1228 *Manag. Ecol.* 17, 513–521. <https://doi.org/10.1111/j.1365-2400.2010.00750.x>
- 1229 Dalmagro, H.J., de A. Lobo, F., Vourlitis, G.L., Dalmolin, Â.C., Antunes, M.Z., Ortíz, C.E.R.,  
1230 de S. Nogueira, J., 2016. Photosynthetic response of a wetland- and an upland-adapted tree  
1231 species to seasonal variations in hydrology in the Brazilian Cerrado and Pantanal. *Acta*  
1232 *Physiol. Plant.* 38, 107. <https://doi.org/10.1007/s11738-016-2125-7>
- 1233 de Almeida, G.A.M., Bates, P., Ozdemir, H., 2018. Modelling urban floods at submetre  
1234 resolution: challenges or opportunities for flood risk management? *J. Flood Risk Manag.*  
1235 11, S855–S865. <https://doi.org/10.1111/jfr3.12276>
- 1236 Denevan, W.M., 1996. A Bluff Model of Riverine Settlement in Prehistoric Amazonia. *Ann.*  
1237 *Assoc. Am. Geogr.* 86, 654–681. <https://doi.org/10.1111/j.1467-8306.1996.tb01771.x>

- 1238 Draper, F.C., Roucoux, K.H., Lawson, I.T., Mitchard, E.T.A., Honorio Coronado, E.N.,  
1239 Läfteenoja, O., Montenegro, L.T., Sandoval, E.V., Zaráte, R., Baker, T.R., 2014. The  
1240 distribution and amount of carbon in the largest peatland complex in Amazonia. *Environ.*  
1241 *Res. Lett.* 9. <https://doi.org/10.1088/1748-9326/9/12/124017>
- 1242 Dunne, T., Mertes, L.A.K., Meade, R.H., Richey, J.E., Forsberg, B.R., 1998. Exchanges of  
1243 sediment between the flood plain and channel of the Amazon River in Brazil. *Bull. Geol.*  
1244 *Soc. Am.* 110, 450–467. [https://doi.org/10.1130/0016-](https://doi.org/10.1130/0016-7606(1998)110<0450:EOSBTF>2.3.CO;2)  
1245 [7606\(1998\)110<0450:EOSBTF>2.3.CO;2](https://doi.org/10.1130/0016-7606(1998)110<0450:EOSBTF>2.3.CO;2)
- 1246 Duponchelle, F., Isaac, V.J., Doria, C., Van Damme, P.A., Herrera-R, G.A., Anderson, E.P.,  
1247 Cruz, R.E.A., Hauser, M., Hermann, T.W., Agudelo, E., Bonilla-Castillo, C., Barthem, R.,  
1248 Freitas, C.E.C., García-Dávila, C., García-Vasquez, A., Renno, J., Castello, L., 2021.  
1249 Conservation of migratory fishes in the Amazon basin. *Aquat. Conserv. Mar. Freshw.*  
1250 *Ecosyst. aqc.3550*. <https://doi.org/10.1002/aqc.3550>
- 1251 Espinoza Villar, J.C., Ronchail, J., Guyot, J.L., Cochonneau, G., Naziano, F., Lavado, W., De  
1252 Oliveira, E., Pombosa, R., Vauchel, P., 2009. Spatio-temporal rainfall variability in the  
1253 Amazon basin countries (Brazil, Peru, Bolivia, Colombia, and Ecuador). *Int. J. Climatol.*  
1254 29, 1574–1594. <https://doi.org/10.1002/joc.1791>
- 1255 Espinoza Villar, J.C., Ronchail, J., Marengo, J.A., Segura, H., 2019. Contrasting North–South  
1256 changes in Amazon wet-day and dry-day frequency and related atmospheric features (1981–  
1257 2017). *Clim. Dyn.* 52, 5413–5430. <https://doi.org/10.1007/s00382-018-4462-2>

1258 Farr, T.G., Rosen, P.A., Caro, E., Crippen, R., Duren, R., Hensley, S., Kobrick, M., Paller, M.,  
1259 Rodriguez, E., Roth, L., Seal, D., Shaffer, S., Shimada, J., Umland, J., Werner, M., Oskin,  
1260 M., Burbank, D., Alsdorf, D.E., 2007. The shuttle radar topography mission. *Rev. Geophys.*  
1261 45, 1–25. <https://doi.org/10.1029/2005RG000183>

1262 Fassoni-Andrade, 2020. PhD thesis. Mapeamento e caracterização do sistema rio-planície da  
1263 Amazônia central via sensoriamento remoto e modelagem hidráulica. Federal University of  
1264 Rio Grande do Sul. Available at <<https://lume.ufrgs.br/handle/10183/211269>>.

1265 Fassoni-Andrade, A.C., Fleischmann, A.S., Papa, F., Paiva, R.C.D. de, Wongchuig, S., Melack,  
1266 J.M., Moreira, A.A., Paris, A., Ruhoff, A., Barbosa, C., Maciel, D.A., Novo, E., Durand, F.,  
1267 Frappart, F., Aires, F., Abrahão, G.M., Ferreira-Ferreira, J., Espinoza, J.C., Laipelt, L.,  
1268 Costa, M.H., Espinoza-Villar, R., Calmant, S., Pellet, V., 2021. Amazon Hydrology From  
1269 Space: Scientific Advances and Future Challenges. *Rev. Geophys.* 59, 1–97.  
1270 <https://doi.org/10.1029/2020RG000728>

1271 Fassoni-Andrade, A.C., Paiva, R.C.D. de, 2019. Mapping spatial-temporal sediment dynamics of  
1272 river-floodplains in the Amazon. *Remote Sens. Environ.*  
1273 <https://doi.org/10.1016/j.rse.2018.10.038>

1274 Fassoni-Andrade, A.C., Paiva, R.C.D. de, Rudorff, C. de M., Barbosa, C.C.F., Novo, E.M.L. de  
1275 M., 2020. High-resolution mapping of floodplain topography from space: A case study in  
1276 the Amazon. *Remote Sens. Environ.* 251, 112065. <https://doi.org/10.1016/j.rse.2020.112065>

1277 Feng, D., Raoufi, R., Beighley, E., Melack, J.M., Goulding, M., Barthem, R.B., Venticinque, E.,  
1278 Cañas, C., Forsberg, B., Sorribas, M.V., 2020. Future climate impacts on the hydrology of

1279 headwater streams in the Amazon River Basin: Implications for migratory goliath catfishes.  
1280 Hydrol. Process. hyp.13952. <https://doi.org/10.1002/hyp.13952>

1281 Ferreira-Ferreira, J., Silva, T.S.F., Streher, A.S., Affonso, A.G., de Almeida Furtado, L.F.,  
1282 Forsberg, B.R., Valsecchi, J., Queiroz, H.L., de Moraes Novo, E.M.L., 2015. Combining  
1283 ALOS/PALSAR derived vegetation structure and inundation patterns to characterize major  
1284 vegetation types in the Mamirauá Sustainable Development Reserve, Central Amazon  
1285 floodplain, Brazil. *Wetl. Ecol. Manag.* 23, 41–59. [https://doi.org/10.1007/s11273-014-9359-](https://doi.org/10.1007/s11273-014-9359-1)  
1286 1

1287 Fleischmann, A.S., Fialho Brêda, J.P., Rudorff, C., Dias de Paiva, R.C., Collischonn, W., Papa,  
1288 F., Ravello, M.M., 2021. River Flood Modeling and Remote Sensing Across Scales:  
1289 Lessons from Brazil, in: Schumann, G.J.P. (Ed.), *Earth Observation for Flood Applications*.  
1290 Elsevier, pp. 61–103. <https://doi.org/10.1016/B978-0-12-819412-6.00004-3>

1291 Fleischmann, A.S., Paiva, R.C.D., Collischonn, W., Siqueira, V.A., Paris, A., Moreira, D.M.,  
1292 Papa, F., Bitar, A.A., Parrens, M., Aires, F., Garambois, P.A., 2020. Trade-Offs Between 1-  
1293 D and 2-D Regional River Hydrodynamic Models. *Water Resour. Res.* 56.  
1294 <https://doi.org/10.1029/2019WR026812>

1295 Flores, B.M., Holmgren, M., 2021. White-Sand Savannas Expand at the Core of the Amazon  
1296 After Forest Wildfires. *Ecosystems* 24, 1624–1637. [https://doi.org/10.1007/s10021-021-](https://doi.org/10.1007/s10021-021-00607-x)  
1297 00607-x

1298 Fluet-Chouinard, E., Lehner, B., Rebelo, L.M., Papa, F., Hamilton, S.K., 2015. Development of  
1299 a global inundation map at high spatial resolution from topographic downscaling of coarse-

1300 scale remote sensing data. *Remote Sens. Environ.* 158, 348–361.  
1301 <https://doi.org/10.1016/j.rse.2014.10.015>

1302 Frappart, F., Seyler, F., Martinez, J., León, J.G., Cazenave, A., 2005. Floodplain water storage in  
1303 the Negro River basin estimated from microwave remote sensing of inundation area and  
1304 water levels. *Remote Sens. Environ.* 99, 387–399. <https://doi.org/10.1016/j.rse.2005.08.016>

1305 Fu, R., Yin, L., Li, W., Arias, P.A., Dickinson, R.E., Huang, L., Chakraborty, S., Fernandes, K.,  
1306 Liebmann, B., Fisher, R., Myneni, R.B., 2013. Increased dry-season length over southern  
1307 Amazonia in recent decades and its implication for future climate projection. *Proc. Natl.*  
1308 *Acad. Sci. U. S. A.* 110, 18110–18115. <https://doi.org/10.1073/pnas.1302584110>

1309 Getirana, A., Boone, A., Yamazaki, D., Decharme, B., Papa, F., Mognard, N., 2012. The  
1310 Hydrological Modeling and Analysis Platform (HyMAP): Evaluation in the Amazon Basin.  
1311 *J. Hydrometeorol.* 13, 1641–1665. <https://doi.org/10.1175/JHM-D-12-021.1>

1312 Getirana, A., Peters-Lidard, C., Rodell, M., Bates, P.D., 2017. Trade-off between cost and  
1313 accuracy in large-scale surface water dynamic modeling. *Water Resour. Res.* 53, 4942–  
1314 4955. <https://doi.org/10.1002/2017WR020519>

1315 Gloor, M., Brienen, R.J.W., Galbraith, D., Feldpausch, T.R., Schöngart, J., Guyot, J.L.,  
1316 Espinoza, J.C., Lloyd, J., Phillips, O.L., 2013. Intensification of the Amazon hydrological  
1317 cycle over the last two decades. *Geophys. Res. Lett.* 40, 1729–1733.  
1318 <https://doi.org/10.1002/grl.50377>

1319 Guilhen, J., Al Bitar, A., Sauvage, S., Parrens, M., Martinez, J., Abril, G., Moreira-Turcq, P.,  
1320 Sánchez-Pérez, J.-M., 2020. Denitrification and associated nitrous oxide and carbon dioxide



1321 emissions from the Amazonian wetlands. *Biogeosciences* 17, 4297–4311.  
1322 <https://doi.org/10.5194/bg-17-4297-2020>

1323 Guimberteau, M., Drapeau, G., Ronchail, J., Sultan, B., Polcher, J., Martinez, J.-M., Prigent, C.,  
1324 Guyot, J.-L., Cochonneau, G., Espinoza, J.C., Filizola, N., Fraizy, P., Lavado, W., De  
1325 Oliveira, E., Pombosa, R., Noriega, L., Vauchel, P., 2012. Discharge simulation in the sub-  
1326 basins of the Amazon using ORCHIDEE forced by new datasets. *Hydrol. Earth Syst. Sci.*  
1327 16, 911–935. <https://doi.org/10.5194/hess-16-911-2012>

1328 Gumbrecht, T., Roman-Cuesta, R.M., Verchot, L., Herold, M., Wittmann, F., Householder, E.,  
1329 Herold, N., Murdiyarso, D., 2017. An expert system model for mapping tropical wetlands  
1330 and peatlands reveals South America as the largest contributor. *Glob. Chang. Biol.* 23,  
1331 3581–3599. <https://doi.org/10.1111/gcb.13689>

1332 Hamilton, S.K., Kellndorfer, J., Lehner, B., Tobler, M., 2007. Remote sensing of floodplain  
1333 geomorphology as a surrogate for biodiversity in a tropical river system (Madre de Dios,  
1334 Peru). *Geomorphology* 89, 23–38. <https://doi.org/10.1016/j.geomorph.2006.07.024>

1335 Hamilton, S.K., Sippel, S.J., Melack, J.M., 2002. Comparison of inundation patterns among  
1336 major South American floodplains. *Journal of Geophysical Research* 107 (D20): Art. No.  
1337 8038, 1–14. <https://doi.org/10.1029/2000JD000306>

1338 Hamilton, S.K., Sippel, S.J., Melack, J.M., 2004. Seasonal inundation patterns in two large  
1339 savanna floodplains of South America: the Llanos de Moxos(Bolivia) and the Llanos del  
1340 Orinoco(Venezuela and Colombia). *Hydrol. Process.* 18, 2103–2116.  
1341 <https://doi.org/10.1002/hyp.5559>

1342 Hansen, M.C., Potapov, P. V., Moore, R., Hancher, M., Turubanova, S.A., Tyukavina, A., Thau,  
1343 D., Stehman, S. V., Goetz, S.J., Loveland, T.R., Kommareddy, A., Egorov, A., Chini, L.,  
1344 Justice, C.O., Townshend, J.R.G., 2013. High-Resolution Global Maps of 21st-Century  
1345 Forest Cover Change. *Science* (80-. ). 342, 850–853.  
1346 <https://doi.org/10.1126/science.1244693>

1347 Harris, I., Jones, P.D., Osborn, T.J., Lister, D.H., 2014. Updated high-resolution grids of monthly  
1348 climatic observations - the CRU TS3.10 Dataset. *Int. J. Climatol.* 34, 623–642.  
1349 <https://doi.org/10.1002/joc.3711>

1350 Hawes, J.E., Peres, C.A., Riley, L.B., Hess, L.L., 2012. Landscape-scale variation in structure  
1351 and biomass of Amazonian seasonally flooded and unflooded forests. *For. Ecol. Manage.*  
1352 281, 163–176. <https://doi.org/10.1016/j.foreco.2012.06.023>

1353 Hess, L.L., Melack, J.M., Affonso, A.G., Barbosa, C., Gastil-Buhl, M., Novo, E.M.L.M., 2015.  
1354 Wetlands of the Lowland Amazon Basin: Extent, Vegetative Cover, and Dual-season  
1355 Inundated Area as Mapped with JERS-1 Synthetic Aperture Radar. *Wetlands* 35, 745–756.  
1356 <https://doi.org/10.1007/s13157-015-0666-y>

1357 Hess, L.L., Melack, J.M., Novo, E.M.L.M., Barbosa, C.C.F., Gastil, M., 2003. Dual-season  
1358 mapping of wetland inundation and vegetation for the central Amazon basin. *Remote Sens.*  
1359 *Environ.* 87, 404–428. <https://doi.org/10.1016/j.rse.2003.04.001>

1360 Hoch, J.M., Haag, A. V., Van Dam, A., Winsemius, H.C., Van Beek, L.P.H., Bierkens, M.F.P.,  
1361 2017. Assessing the impact of hydrodynamics on large-scale flood wave propagation: A  
1362 case study for the Amazon Basin. *Hydrol. Earth Syst. Sci.* 21, 117–132.

- 1363 <https://doi.org/10.5194/hess-21-117-2017>
- 1364 Hu, S., Niu, Z., Chen, Y., 2017. Global Wetland Datasets: a Review. *Wetlands* 37, 807–817.
- 1365 <https://doi.org/10.1007/s13157-017-0927-z>
- 1366 Jardim, C.M., Nardoto, G.B., de Lima, A.C.B., de Jesus Silva, R., Schor, T., de Oliveira, J.A.,  
1367 Martinelli, L.A., 2020. The influence of seasonal river flooding in food consumption of  
1368 riverine dwellers in the central Amazon region: an isotopic approach. *Archaeol. Anthropol.*  
1369 *Sci.* 12. <https://doi.org/10.1007/s12520-020-01172-5>
- 1370 Jensen, K., McDonald, K., 2019. Surface Water Microwave Product Series Version 3: A Near-  
1371 Real Time and 25-Year Historical Global Inundated Area Fraction Time Series From Active  
1372 and Passive Microwave Remote Sensing. *IEEE Geosci. Remote Sens. Lett.* 16, 1402–1406.  
1373 <https://doi.org/10.1109/lgrs.2019.2898779>
- 1374 Jensen, K., McDonald, K., Podest, E., Rodriguez-Alvarez, N., Horna, V., Steiner, N., 2018.  
1375 Assessing L-Band GNSS-Reflectometry and Imaging Radar for Detecting Sub-Canopy  
1376 Inundation Dynamics in a Tropical Wetlands Complex. *Remote Sens.* 10, 1431.  
1377 <https://doi.org/10.3390/rs10091431>
- 1378 Ji, X., Lesack, L.F.W., Melack, J.M., Wang, S., Riley, W.J., Shen, C., 2019. Seasonal and  
1379 Interannual Patterns and Controls of Hydrological Fluxes in an Amazon Floodplain Lake  
1380 With a Surface-Subsurface Process Model. *Water Resour. Res.* 55, 3056–3075.  
1381 <https://doi.org/10.1029/2018WR023897>
- 1382 Junk, W.J., Bayley, P.B., Sparks, R.E, 1989. The flood pulse concept in river-floodplain systems.  
1383 *Canadian special publication of fisheries and aquatic sciences*, 106.1, 110-127.

- 1384 Junk, W.J., Furch, K., Limnologie, M., Tropenökologie, A., Plon, W.-, 1993. A general review  
1385 of tropical South American floodplains. *Wetl. Ecol. Manag.* 2, 231–238.
- 1386 Junk, W.J., Piedade, M.T.F., Schöngart, J., Cohn-Haft, M., Adeney, J.M., Wittmann, F., 2011. A  
1387 classification of major naturally-occurring amazonian lowland wetlands. *Wetlands* 31, 623–  
1388 640. <https://doi.org/10.1007/s13157-011-0190-7>
- 1389 Lähteenoja, O., Reátegui, Y.R., Räsänen, M., Torres, D.D.C., Oinonen, M., Page, S., 2012. The  
1390 large Amazonian peatland carbon sink in the subsiding Pastaza-Marañón foreland basin,  
1391 Peru. *Glob. Chang. Biol.* 18, 164–178. <https://doi.org/10.1111/j.1365-2486.2011.02504.x>
- 1392 Langerwisch, F., Rost, S., Gerten, D., Poulter, B., Rammig, A., Cramer, W., 2013. Potential  
1393 effects of climate change on inundation patterns in the Amazon Basin. *Hydrol. Earth Syst.*  
1394 *Sci.* 17, 2247–2262. <https://doi.org/10.5194/hess-17-2247-2013>
- 1395 Langill, J.C., Abizaid, C., 2020. What is a bad flood? Local perspectives of extreme floods in the  
1396 Peruvian Amazon. *Ambio* 49, 1423–1436. <https://doi.org/10.1007/s13280-019-01278-8>
- 1397 Latrubesse, E.M., 2012. Amazon lakes, in: *Encyclopedia of Earth Sciences Series*.  
1398 [https://doi.org/10.1007/978-1-4020-4410-6\\_36](https://doi.org/10.1007/978-1-4020-4410-6_36)
- 1399 Lauerwald, R., Regnier, P., Camino-Serrano, M., Guenet, B., Guimberteau, M., Ducharne, A.,  
1400 Polcher, J., Ciais, P., 2017. ORCHILEAK (revision 3875): a new model branch to simulate  
1401 carbon transfers along the terrestrial–aquatic continuum of the Amazon basin. *Geosci.*  
1402 *Model Dev.* 10, 3821–3859. <https://doi.org/10.5194/gmd-10-3821-2017>
- 1403 Lehner, B., Döll, P., 2004. Development and validation of a global database of lakes, reservoirs

1404 and wetlands. *J. Hydrol.* 296, 1–22. <https://doi.org/10.1016/j.jhydrol.2004.03.028>

1405 Lehner, B., Grill, G., 2013. Global river hydrography and network routing: Baseline data and  
1406 new approaches to study the world’s large river systems. *Hydrol. Process.*  
1407 <https://doi.org/10.1002/hyp.9740>

1408 Lesack, L.F.W., Melack, J.M., 1995. Flooding Hydrology and Mixture Dynamics of Lake Water  
1409 Derived from Multiple Sources in an Amazon Floodplain Lake. *Water Resour. Res.* 31,  
1410 329–345. <https://doi.org/10.1029/94WR02271>

1411 Li, D., Lu, D., Moran, E., da Silva, R.F.B., 2020. Examining water area changes accompanying  
1412 dam construction in the Madeira River in the Brazilian Amazon. *Water (Switzerland)* 12.  
1413 <https://doi.org/10.3390/w12071921>

1414 Lobón-Cerviá, J., Hess, L.L., Melack, J.M., Araujo-Lima, C.A.R.M., 2015. The importance of  
1415 forest cover for fish richness and abundance on the Amazon floodplain. *Hydrobiologia* 750,  
1416 245–255. <https://doi.org/10.1007/s10750-014-2040-0>

1417 Luize, B.G., Silva, T.S.F., Wittmann, F., Assis, R.L., Venticinque, E.M., 2015. Effects of the  
1418 Flooding Gradient on Tree Community Diversity in Várzea Forests of the Purus River,  
1419 Central Amazon, Brazil. *Biotropica* 47, 137–142. <https://doi.org/10.1111/btp.12203>

1420 Luo, X., Li, H.-Y., Leung, L.R., Tesfa, T.K., Getirana, A., Papa, F., Hess, L.L., 2017. Modeling  
1421 surface water dynamics in the Amazon Basin using MOSART-Inundation v1.0: impacts of  
1422 geomorphological parameters and river flow representation. *Geosci. Model Dev.* 10, 1233–  
1423 1259. <https://doi.org/10.5194/gmd-10-1233-2017>

- 1424 Mansur, A. V., Brondízio, E.S., Roy, S., Hetrick, S., Vogt, N.D., Newton, A., 2016. An  
1425 assessment of urban vulnerability in the Amazon Delta and Estuary: a multi-criterion index  
1426 of flood exposure, socio-economic conditions and infrastructure. *Sustain. Sci.* 11, 625–643.  
1427 <https://doi.org/10.1007/s11625-016-0355-7>
- 1428 Martinez, J.M., Le Toan, T., 2007. Mapping of flood dynamics and spatial distribution of  
1429 vegetation in the Amazon floodplain using multitemporal SAR data. *Remote Sens. Environ.*  
1430 108, 209–223. <https://doi.org/10.1016/j.rse.2006.11.012>
- 1431 Martínez-Espinosa, C., Sauvage, S., Al Bitar, A., Green, P. A., Vörösmarty, C. J., Sánchez-  
1432 Pérez, J. M. (2020). Denitrification in wetlands: A review towards a quantification at global  
1433 scale. *Science of the total environment* 754, 142398.  
1434 <https://doi.org/10.1016/j.scitotenv.2020.142398>
- 1435 Matthews, E., Fung, I., 1987. Methane emission from natural wetlands: Global distribution, area,  
1436 and environmental characteristics of sources. *Global Biogeochem. Cycles* 1, 61–86.  
1437 <https://doi.org/10.1029/GB001i001p00061>
- 1438 Melack, J.M., 2016. Aquatic Ecosystems, in: *Ecological Studies*. pp. 119–148.  
1439 [https://doi.org/10.1007/978-3-662-49902-3\\_7](https://doi.org/10.1007/978-3-662-49902-3_7)
- 1440 Melack, J.M., Coe, M.T., 2021. Amazon floodplain hydrology and implications for aquatic  
1441 conservation. *Aquat. Conserv. Mar. Freshw. Ecosyst.* 1029–1040.  
1442 <https://doi.org/10.1002/aqc.3558>
- 1443 Melack, J.M., Forsberg, B.R., 2001. Biogeochemistry of Amazon Floodplain, in: McClain, M.E.,  
1444 Victoria, R., Richey, J.E. (Eds.), *The Biogeochemistry of the Amazon Basin*. Oxford

1445 University Press, New York, USA.

1446 Melack, J.M., Hess, L.L., 2010. Remote Sensing of the Distribution and Extent of Wetlands in  
1447 the Amazon Basin, in: Amazonian Floodplain Forests. pp. 43–59.  
1448 [https://doi.org/10.1007/978-90-481-8725-6\\_3](https://doi.org/10.1007/978-90-481-8725-6_3)

1449 Melack, J.M., Hess, L.L., Gastil, M., Forsberg, B.R., Hamilton, S.K., Lima, I.B.T., Novo,  
1450 E.M.L.M., 2004. Regionalization of methane emissions in the Amazon Basin with  
1451 microwave remote sensing. *Glob. Chang. Biol.* 10, 530–544. [https://doi.org/10.1111/j.1365-  
1452 2486.2004.00763.x](https://doi.org/10.1111/j.1365-2486.2004.00763.x)

1453 Meyer Oliveira, A., Fleischmann, A., Paiva, R., 2020. On the contribution of remote sensing-  
1454 based calibration to model multiple hydrological variables. *J. Hydrol.*  
1455 <https://doi.org/10.1016/j.jhydrol.2021.126184>

1456 Miguez-Macho, G., Fan, Y., 2012. The role of groundwater in the Amazon water cycle: 1.  
1457 Influence on seasonal streamflow, flooding and wetlands. *J. Geophys. Res. Atmos.* 117, 1–  
1458 30. <https://doi.org/10.1029/2012JD017539>

1459 Nardi, F., Annis, A., Di Baldassarre, G., Vivoni, E.R., Grimaldi, S., 2019. GFPLAIN250m, a  
1460 global high-resolution dataset of Earth’s floodplains. *Sci. Data* 6, 180309.  
1461 <https://doi.org/10.1038/sdata.2018.309>

1462 O’Loughlin, F.E., Paiva, R.C.D., Durand, M., Alsdorf, D.E., Bates, P.D., 2016. A multi-sensor  
1463 approach towards a global vegetation corrected SRTM DEM product. *Remote Sens.*  
1464 *Environ.* 182, 49–59. <https://doi.org/10.1016/j.rse.2016.04.018>

- 1465 Ovando, A., Martinez, J.M., Tomasella, J., Rodriguez, D.A., von Randow, C., 2018. Multi-  
1466 temporal flood mapping and satellite altimetry used to evaluate the flood dynamics of the  
1467 Bolivian Amazon wetlands. *Int. J. Appl. Earth Obs. Geoinf.* 69, 27–40.  
1468 <https://doi.org/10.1016/j.jag.2018.02.013>
- 1469 Ovando, A., Tomasella, J., Rodriguez, D.A., Martinez, J.M., Siqueira-Junior, J.L., Pinto, G.L.N.,  
1470 Passy, P., Vauchel, P., Noriega, L., von Randow, C., 2016. Extreme flood events in the  
1471 Bolivian Amazon wetlands. *J. Hydrol. Reg. Stud.* 5, 293–308.  
1472 <https://doi.org/10.1016/j.ejrh.2015.11.004>
- 1473 Paca, V.H. da M., Espinoza-Dávalos, G.E., Hessels, T.M., Moreira, D.M., Comair, G.F.,  
1474 Bastiaanssen, W.G.M., 2019. The spatial variability of actual evapotranspiration across the  
1475 Amazon River Basin based on remote sensing products validated with flux towers. *Ecol.*  
1476 *Process.* 8, 6. <https://doi.org/10.1186/s13717-019-0158-8>
- 1477 Paiva, R., Buarque, D.C., Collischonn, W., Bonnet, M.P., Frappart, F., Calmant, S., Bulhões  
1478 Mendes, C.A., 2013. Large-scale hydrologic and hydrodynamic modeling of the Amazon  
1479 River basin. *Water Resour. Res.* 49, 1226–1243. <https://doi.org/10.1002/wrcr.20067>
- 1480 Pangala, S.R., Enrich-Prast, A., Basso, L.S., Peixoto, R.B., Bastviken, D., Hornibrook, E.R.C.,  
1481 Gatti, L. V., Marotta, H., Calazans, L.S.B., Sakuragui, C.M., Bastos, W.R., Malm, O.,  
1482 Gloor, E., Miller, J.B., Gauci, V., 2017. Large emissions from floodplain trees close the  
1483 Amazon methane budget. *Nature* 552, 230–234. <https://doi.org/10.1038/nature24639>
- 1484 Papa, F., J.-F. Crétaux, M. Grippa, E. Robert, M. Trigg, R. Tshimanga, B. Kitambo, A. Paris, A.  
1485 Carr, A.S. Fleischmann, M. de Fleury, P.G. Gbetkom, B. Calmettes, Calmant, S., 2022.



1486 Water Resources in Africa under Global Change: Monitoring Surface Waters from Space.  
1487 Surveys in Geophysics. <https://doi.org/10.1007/s10712-022-09700-9>

1488 Papa, F., and F. Frappart (2021), Surface Water Storage in Rivers and Wetlands Derived from  
1489 Satellite Observations: A Review of Current Advances and Future Opportunities for  
1490 Hydrological Sciences, *Remote Sensing*, 13(20), 4162, doi:10.3390/rs13204162

1491 Papa, F., Güntner, A., Frappart, F., Prigent, C., Rossow, W.B., 2008. Variations of surface water  
1492 extent and water storage in large river basins: A comparison of different global data  
1493 sources. *Geophys. Res. Lett.* 35, L11401. <https://doi.org/10.1029/2008GL033857>

1494 Papa, F., Prigent, C., Aires, F., Jimenez, C., Rossow, W.B., Matthews, E., 2010. Interannual  
1495 variability of surface water extent at the global scale, 1993–2004. *J. Geophys. Res.* 115,  
1496 D12111. <https://doi.org/10.1029/2009JD012674>

1497 Park, E., Latrubesse, E.M., 2017. The hydro-geomorphologic complexity of the lower Amazon  
1498 River floodplain and hydrological connectivity assessed by remote sensing and field  
1499 control. *Remote Sens. Environ.* 198, 321–332. <https://doi.org/10.1016/j.rse.2017.06.021>

1500 Park, E., Latrubesse, E.M., 2019. A geomorphological assessment of wash-load sediment fluxes  
1501 and floodplain sediment sinks along the lower Amazon River. *Geology* 47, 403–406.  
1502 <https://doi.org/10.1130/G45769.1>

1503 Parrens, M., Al Bitar, A., Frappart, F., Papa, F., Calmant, S., Crétaux, J.-F., Wigneron, J.-P.,  
1504 Kerr, Y., 2017. Mapping Dynamic Water Fraction under the Tropical Rain Forests of the  
1505 Amazonian Basin from SMOS Brightness Temperatures. *Water* 9, 350.  
1506 <https://doi.org/10.3390/w9050350>

1507 Parrens, M., Bitar, A. Al, Frappart, F., Paiva, R., Wongchuig, S., Papa, F., Yamasaki, D., Kerr,  
1508 Y., 2019. High resolution mapping of inundation area in the Amazon basin from a  
1509 combination of L-band passive microwave, optical and radar datasets. *Int. J. Appl. Earth*  
1510 *Obs. Geoinf.* 81, 58–71. <https://doi.org/10.1016/j.jag.2019.04.011>

1511 Pekel, J., Cottam, A., Gorelick, N., Belward, A.S., 2016. High-resolution mapping of global  
1512 surface water and its long-term changes. *Nature* 540, 418–422.  
1513 <https://doi.org/10.1038/nature20584>

1514 Pellet, V., Aires, F., Yamazaki, D., Papa, F., 2021. Coherent Satellite Monitoring of the Water  
1515 Cycle Over the Amazon. Part 1: Methodology and Initial Evaluation. *Water Resour. Res.*  
1516 57, 1–21. <https://doi.org/10.1029/2020wr028647>

1517 Pham-Duc, B., Prigent, C., Aires, F., Papa, F., 2017. Comparisons of global terrestrial surface  
1518 water datasets over 15 years. *J. Hydrometeorol.* 18, 993–1007.  
1519 <https://doi.org/10.1175/JHM-D-16-0206.1>

1520 Pickens, A.H., Hansen, M.C., Hancher, M., Stehman, S. V., Tyukavina, A., Potapov, P.,  
1521 Marroquin, B., Sherani, Z., 2020. Mapping and sampling to characterize global inland water  
1522 dynamics from 1999 to 2018 with full Landsat time-series. *Remote Sens. Environ.* 243,  
1523 111792. <https://doi.org/10.1016/j.rse.2020.111792>

1524 Pinel, S., Bonnet, M., S. Da Silva, J., Sampaio, T.C., Garnier, J., Catry, T., Calmant, S., Fragoso,  
1525 C.R., Moreira, D., Motta Marques, D., Seyler, F., 2019. Flooding dynamics within an  
1526 Amazonian floodplain: water circulation patterns and inundation duration. *Water Resour.*  
1527 *Res.* 2019WR026081. <https://doi.org/10.1029/2019WR026081>

1528 Prigent, C., Jimenez, C., Bousquet, P., 2020. Satellite-Derived Global Surface Water Extent and  
1529 Dynamics Over the Last 25 Years (GIEMS-2). *J. Geophys. Res. Atmos.* 125, 1–18.  
1530 <https://doi.org/10.1029/2019JD030711>

1531 Prigent, C., Matthews, E., Aires, F., Rossow, W.B., 2001. Remote sensing of global wetland  
1532 dynamics with multiple satellite data sets. *Geophys. Res. Lett.* 28, 4631–4634.  
1533 <https://doi.org/10.1029/2001GL013263>

1534 Prigent, C., Papa, F., Aires, F., Rossow, W.B., Matthews, E., 2007. Global inundation dynamics  
1535 inferred from multiple satellite observations, 1993-2000. *J. Geophys. Res. Atmos.* 112,  
1536 1993–2000. <https://doi.org/10.1029/2006JD007847>

1537 Prigent, C., Rochetin, N., Aires, F., Defer, E., Grandpeix, J.-Y., Jimenez, C., Papa, F., 2011.  
1538 Impact of the inundation occurrence on the deep convection at continental scale from  
1539 satellite observations and modeling experiments. *J. Geophys. Res. Atmos.* 116, n/a-n/a.  
1540 <https://doi.org/10.1029/2011JD016311>

1541 Reis, V., Hermoso, V., Hamilton, S.K., Bunn, S.E., Fluet-Chouinard, E., Venables, B., Linke, S.,  
1542 2019. Characterizing seasonal dynamics of Amazonian wetlands for conservation and  
1543 decision making. *Aquat. Conserv. Mar. Freshw. Ecosyst.* 29, 1073–1082.  
1544 <https://doi.org/10.1002/aqc.3051>

1545 Reis, V., Hermoso, V., Hamilton, S.K., Bunn, S.E., Linke, S., 2019b. Conservation planning for  
1546 river-wetland mosaics: A flexible spatial approach to integrate floodplain and upstream  
1547 catchment connectivity. *Biol. Conserv.* 236, 356–365.  
1548 <https://doi.org/10.1016/j.biocon.2019.05.042>

1549 Rennó, C.D., Nobre, A.D., Cuartas, L.A., Soares, J.V., Hodnett, M.G., Tomasella, J., Waterloo,  
1550 M.J., 2008. HAND, a new terrain descriptor using SRTM-DEM: Mapping terra-firme  
1551 rainforest environments in Amazonia. *Remote Sens. Environ.* 112, 3469–3481.  
1552 <https://doi.org/10.1016/j.rse.2008.03.018>

1553 Renó, V.F., Novo, E.M.L.M., Suemitsu, C., Rennó, C.D., Silva, T.S.F., 2011. Assessment of  
1554 deforestation in the Lower Amazon floodplain using historical Landsat MSS/TM imagery.  
1555 *Remote Sens. Environ.* 115, 3446–3456. <https://doi.org/10.1016/j.rse.2011.08.008>

1556 Resende, A.F. de, Schöngart, J., Streher, A.S., Ferreira-Ferreira, J., Piedade, M.T.F., Silva,  
1557 T.S.F., 2019. Massive tree mortality from flood pulse disturbances in Amazonian floodplain  
1558 forests: The collateral effects of hydropower production. *Sci. Total Environ.* 659, 587–598.  
1559 <https://doi.org/10.1016/j.scitotenv.2018.12.208>

1560 Restrepo A, J.D., Kettner, A.J., Robert Brakenridge, G., 2020. Monitoring water discharge and  
1561 floodplain connectivity for the northern Andes utilizing satellite data: A tool for river  
1562 planning and science-based decision-making. *J. Hydrol.* 586, 124887.  
1563 <https://doi.org/10.1016/j.jhydrol.2020.124887>

1564 Richey, J.E., Hedges, J.I., Devol, A.H., Quay, P.D., Victoria, R., Martinelli, L., Forsberg, B.R.,  
1565 1990. Biogeochemistry of carbon in the Amazon River. *Limnol. Oceanogr.* 35, 352–371.  
1566 <https://doi.org/10.4319/lo.1990.35.2.0352>

1567 Richey, J.E., Melack, J.M., Aufdenkampe, A.K., Ballester, V.M., Hess, L.L., 2002. Outgassing  
1568 from Amazonian rivers and wetlands as a large tropical source of atmospheric CO<sub>2</sub>. *Nature*  
1569 416, 617–620. <https://doi.org/10.1038/416617a>

1570 Ringeval, B., Decharme, B., Piao, S.L., Ciais, P., Papa, F., de Noblet-Ducoudré, N., Prigent, C.,  
1571 Friedlingstein, P., Gouttevin, I., Koven, C., Ducharne, A., 2012. Modelling sub-grid  
1572 wetland in the ORCHIDEE global land surface model: evaluation against river discharges  
1573 and remotely sensed data. *Geosci. Model Dev.* 5, 941–962. [https://doi.org/10.5194/gmd-5-](https://doi.org/10.5194/gmd-5-941-2012)  
1574 941-2012

1575 Ringeval, B., Houweling, S., van Bodegom, P.M., Spahni, R., van Beek, R., Joos, F., Röckmann,  
1576 T., 2014. Methane emissions from floodplains in the Amazon Basin: challenges in  
1577 developing a process-based model for global applications. *Biogeosciences* 11, 1519–1558.  
1578 <https://doi.org/10.5194/bg-11-1519-2014>

1579 Rodriguez-Alvarez, N., Podest, E., Jensen, K., McDonald, K.C., 2019. Classifying Inundation in  
1580 a Tropical Wetlands Complex with GNSS-R. *Remote Sens.* 11, 1053.  
1581 <https://doi.org/10.3390/rs11091053>

1582 Rosenqvist, A., Forsberg, B.R., Pimentel, T., Rauste, Y.A., Richey, J.E., 2002. The use of  
1583 spaceborne radar data to model inundation patterns and trace gas emissions in the central  
1584 Amazon floodplain. *Int. J. Remote Sens.* 23, 1303–1328.  
1585 <https://doi.org/10.1080/01431160110092911>

1586 Rosenqvist, J., Rosenqvist, A., Jensen, K., McDonald, K., 2020. Mapping of Maximum and  
1587 Minimum Inundation Extents in the Amazon Basin 2014–2017 with ALOS-2 PALSAR-2  
1588 ScanSAR Time-Series Data. *Remote Sens.* 12, 1326. <https://doi.org/10.3390/rs12081326>

1589 Rosinger, A.Y., 2018. Household water insecurity after a historic flood: Diarrhea and  
1590 dehydration in the Bolivian Amazon. *Soc. Sci. Med.* 197, 192–202.

1591 <https://doi.org/10.1016/j.socscimed.2017.12.016>

1592 Rossetti, D.F., Gribel, R., Rennó, C.D., Cohen, M.C.L., Moulatlet, G.M., Cordeiro, C.L. de O.,  
1593 Rodrigues, E. do S.F., 2017a. Late Holocene tectonic influence on hydrology and vegetation  
1594 patterns in a northern Amazonian megafan. *Catena* 158, 121–130.  
1595 <https://doi.org/10.1016/j.catena.2017.06.022>

1596 Rossetti, D.F., Valeriano, M.M., Gribel, R., Cohen, M.C.L., Tatumi, S.H., Yee, M., 2017b. The  
1597 imprint of Late Holocene tectonic reactivation on a megafan landscape in the northern  
1598 Amazonian wetlands. *Geomorphology* 295, 406–418.  
1599 <https://doi.org/10.1016/j.geomorph.2017.07.026>

1600 Rudorff, C.M., Melack, J.M., Bates, P.D., 2014. Flooding dynamics on the lower Amazon  
1601 floodplain: 1. Hydraulic controls on water elevation, inundation extent, and river-floodplain  
1602 discharge. *Water Resour. Res.* 50, 619–634. <https://doi.org/10.1002/2013WR014091>

1603 Ruf, C.S., Chew, C., Lang, T. et al. A New Paradigm in Earth Environmental Monitoring with  
1604 the CYGNSS Small Satellite Constellation. *Sci Rep* 8, 8782 (2018).  
1605 <https://doi.org/10.1038/s41598-018-27127-4>

1606 Ruiz Agudelo, C.A., Mazzeo, N., Díaz, I., Barral, M.P., Piñeiro, G., Gadino, I., Roche, I., Acuña-  
1607 Posada, R.J., 2020. Land use planning in the amazon basin: Challenges from resilience  
1608 thinking. *Ecol. Soc.* 25. <https://doi.org/10.5751/ES-11352-250108>

1609 Santos, J.O.S., Nelson, B.W., Giovannini, C.A., 1993. Corpos de areia sob leitos abandonados de  
1610 grandes rios. *Ciência Hoje* 16, 22–25.

1611 Santos, L.B.L., Carvalho, T., Anderson, L.O., Rudorff, C.M., Marchezini, V., Londe, L.R., Saito,  
1612 S.M., 2017. An RS-GIS-Based Comprehensive Impact Assessment of Floods—A Case  
1613 Study in Madeira River, Western Brazilian Amazon. *IEEE Geosci. Remote Sens. Lett.* 14,  
1614 1614–1617. <https://doi.org/10.1109/LGRS.2017.2726524>

1615 Santos, M.J., Medvigy, D., Silva Dias, M.A.F., Freitas, E.D., Kim, H., 2019. Seasonal Flooding  
1616 Causes Intensification of the River Breeze in the Central Amazon. *J. Geophys. Res. Atmos.*  
1617 124, 5178–5197. <https://doi.org/10.1029/2018JD029439>

1618 Saunio, M., Stavert, A.R., Poulter, B., Bousquet, P., Canadell, J.G., Jackson, R.B., Raymond,  
1619 P.A., Dlugokencky, E.J., Houweling, S., Patra, P.K., Ciais, P., Arora, V.K., Bastviken, D.,  
1620 Bergamaschi, P., Blake, D.R., Brailsford, G., Bruhwiler, L., Carlson, K.M., Carrol, M.,  
1621 Castaldi, S., Chandra, N., Crevoisier, C., Crill, P.M., Covey, K., Curry, C.L., Etiope, G.,  
1622 Frankenberg, C., Gedney, N., Hegglin, M.I., Höglund-Isaksson, L., Hugelius, G., Ishizawa,  
1623 M., Ito, A., Janssens-Maenhout, G., Jensen, K.M., Joos, F., Kleinen, T., Krummel, P.B.,  
1624 Langenfelds, R.L., Laruelle, G.G., Liu, L., Machida, T., Maksyutov, S., McDonald, K.C.,  
1625 McNorton, J., Miller, P.A., Melton, J.R., Morino, I., Müller, J., Murguia-Flores, F., Naik,  
1626 V., Niwa, Y., Noce, S., O’Doherty, S., Parker, R.J., Peng, C., Peng, S., Peters, G.P., Prigent,  
1627 C., Prinn, R., Ramonet, M., Regnier, P., Riley, W.J., Rosentreter, J.A., Segers, A., Simpson,  
1628 I.J., Shi, H., Smith, S.J., Steele, L.P., Thornton, B.F., Tian, H., Tohjima, Y., Tubiello, F.N.,  
1629 Tsuruta, A., Viovy, N., Voulgarakis, A., Weber, T.S., van Weele, M., van der Werf, G.R.,  
1630 Weiss, R.F., Worthy, D., Wunch, D., Yin, Y., Yoshida, Y., Zhang, W., Zhang, Z., Zhao, Y.,  
1631 Zheng, B., Zhu, Qing, Zhu, Qian, Zhuang, Q., 2020. The Global Methane Budget 2000–  
1632 2017. *Earth Syst. Sci. Data* 12, 1561–1623. <https://doi.org/10.5194/essd-12-1561-2020>

1633 Schöngart, J., Wittmann, F., Faria de Resende, A., Assahira, C., Sousa Lobo, G., Rocha Duarte  
1634 Neves, J., Rocha, M., Biem Mori, G., Costa Quaresma, A., Oreste Demarchi, L., Weiss  
1635 Albuquerque, B., Oliveira Feitosa, Y., Silva Costa, G., Vieira Feitoza, G., Machado  
1636 Durgante, F., Lopes, A., Trumbore, S.E., Sanna Freire Silva, T., Steege, H., Val, A.L., Junk,  
1637 W.J., Piedade, M.T.F., 2021. The shadow of the Balbina dam: A synthesis of over 35 years  
1638 of downstream impacts on floodplain forests in Central Amazonia. *Aquat. Conserv. Mar.*  
1639 *Freshw. Ecosyst.* 31, 1117–1135. <https://doi.org/10.1002/aqc.3526>

1640 Schroeder, R., McDonald, K., Chapman, B., Jensen, K., Podest, E., Tessler, Z., Bohn, T.,  
1641 Zimmermann, R., 2015. Development and Evaluation of a Multi-Year Fractional Surface  
1642 Water Data Set Derived from Active/Passive Microwave Remote Sensing Data. *Remote*  
1643 *Sens.* 7, 16688–16732. <https://doi.org/10.3390/rs71215843>

1644 Schumann, G.J.P., Stampoulis, D., Smith, A.M., Sampson, C.C., Andreadis, K.M., Neal, J.C.,  
1645 Bates, P.D., 2016. Rethinking flood hazard at the global scale. *Geophys. Res. Lett.* 43,  
1646 10,249-10,256. <https://doi.org/10.1002/2016GL070260>

1647 Silva, M.V., Paris, A., Calmant, S., Cândido, L.A., Silva, J.S. da, 2018. Relationships between  
1648 Pacific and Atlantic ocean sea surface temperatures and water levels from satellite altimetry  
1649 data in the Amazon rivers. *Brazilian Journal of Water Resources* 23.  
1650 <https://doi.org/10.1590/2318-0331.231820170148>

1651 Silva, T.S.F., Melack, J.M., Novo, E.M.L.M., 2013. Responses of aquatic macrophyte cover and  
1652 productivity to flooding variability on the Amazon floodplain. *Glob. Chang. Biol.* 19, 3379-  
1653 3389. <https://doi.org/10.1111/gcb.12308>



- 1654 Sippel, S.J., Hamilton, S.K., Melack, J.M., 1992. Inundation area and morphometry of lakes on  
1655 the Amazon River floodplain, Brazil. *Arch. Hydrobiol* 123, 385–400.
- 1656 Sippel, S.J., Hamilton, S.K., Melack, J.M., Novo, E.M.M., 1998. Passive microwave  
1657 observations of inundation area and the area/stage relation in the amazon river floodplain.  
1658 *Int. J. Remote Sens.* 19, 3055–3074. <https://doi.org/10.1080/014311698214181>
- 1659 Siqueira, V.A., Paiva, R.C.D., Fleischmann, A.S., Fan, F.M., Ruhoff, A.L., Pontes, P.R.M.,  
1660 Paris, A., Calmant, S., Collischonn, W., 2018. Toward continental hydrologic–  
1661 hydrodynamic modeling in South America. *Hydrol. Earth Syst. Sci.* 22, 4815–4842.  
1662 <https://doi.org/10.5194/hess-22-4815-2018>
- 1663 Sorribas, M.V., Paiva, R.C.D., Melack, J.M., Bravo, J.M., Jones, C., Carvalho, L., Beighley, E.,  
1664 Forsberg, B., Costa, M.H., 2016. Projections of climate change effects on discharge and  
1665 inundation in the Amazon basin. *Clim. Change* 136, 555–570.  
1666 <https://doi.org/10.1007/s10584-016-1640-2>
- 1667 Souza, C.M., Kirchhoff, F.T., Oliveira, B.C., Ribeiro, J.G., Sales, M.H., 2019. Long-term annual  
1668 surface water change in the Brazilian Amazon Biome: Potential links with deforestation,  
1669 infrastructure development and climate change. *Water (Switzerland)* 11, 566.  
1670 <https://doi.org/10.3390/w11030566>
- 1671 Staver, A.C., Archibald, S., Levin, S.A., 2011. The Global Extent and Determinants of Savanna  
1672 and Forest as Alternative Biome States. *Science (80-. )*. 334, 230–232.  
1673 <https://doi.org/10.1126/science.1210465>
- 1674 Taylor, C.M., Prigent, C., Dadson, S.J., 2018. Mesoscale rainfall patterns observed around

1675 wetlands in sub-Saharan Africa. *Q. J. R. Meteorol. Soc.* 144, 2118–2132.  
1676 <https://doi.org/10.1002/qj.3311>

1677 Towner, J., Cloke, H.L., Zsoter, E., Flamig, Z., Hoch, J.M., Bazo, J., Coughlan de Perez, E.,  
1678 Stephens, E.M., 2019. Assessing the performance of global hydrological models for  
1679 capturing peak river flows in the Amazon basin. *Hydrol. Earth Syst. Sci.* 23, 3057–3080.  
1680 <https://doi.org/10.5194/hess-23-3057-2019>

1681 Trigg, M.A., Birch, C.E., Neal, J.C., Bates, P.D., Smith, A., Sampson, C.C., Yamazaki, D.,  
1682 Hirabayashi, Y., Pappenberger, F., Dutra, E., Ward, P.J., Winsemius, H.C., Salamon, P.,  
1683 Dottori, F., Rudari, R., Kappes, M.S., Simpson, A.L., Hadzilacos, G., Fewtrell, T.J., 2016.  
1684 The credibility challenge for global fluvial flood risk analysis. *Environ. Res. Lett.* 11,  
1685 094014. <https://doi.org/10.1088/1748-9326/11/9/094014>

1686 Trigg, M.A., Wilson, M.D., Bates, P.D., Horritt, M.S., Alsdorf, D.E., Forsberg, B.R., Vega,  
1687 M.C., 2009. Amazon flood wave hydraulics. *J. Hydrol.* 374, 92–105.  
1688 <https://doi.org/10.1016/j.jhydrol.2009.06.004>

1689 Ward, N.D., Bianchi, T.S., Medeiros, P.M., Seidel, M., Richey, J.E., Keil, R.G., Sawakuchi,  
1690 H.O., 2017. Where Carbon Goes When Water Flows: Carbon Cycling across the Aquatic  
1691 Continuum. *Front. Mar. Sci.* 4, 1–27. <https://doi.org/10.3389/fmars.2017.00007>

1692 Wilson, M.D., Bates, P., Alsdorf, D., Forsberg, B., Horritt, M., Melack, J., Frappart, F.,  
1693 Famiglietti, J., 2007. Modeling large-scale inundation of Amazonian seasonally flooded  
1694 wetlands. *Geophys. Res. Lett.* 34, 4–9. <https://doi.org/10.1029/2007GL030156>

1695 Wongchuig, S.C., Paiva, R.C.D. de, Espinoza, J.C., Collischonn, W., 2017. Multi-decadal

1696 Hydrological Retrospective: Case study of Amazon floods and droughts. *J. Hydrol.* 549,  
1697 667–684. <https://doi.org/10.1016/j.jhydrol.2017.04.019>

1698 Wongchuig, S.C., de Paiva, R.C.D., Siqueira, V., Collischonn, W., 2019. Hydrological reanalysis  
1699 across the 20th century: A case study of the Amazon Basin. *J. Hydrol.* 570, 755–773.  
1700 <https://doi.org/10.1016/j.jhydrol.2019.01.025>

1701 Wongchuig, S.C., Paiva, R.C.D., Biancamaria, S., Collischonn, W., 2020. Assimilation of future  
1702 SWOT-based river elevations, surface extent observations and discharge estimations into  
1703 uncertain global hydrological models. *J. Hydrol.* 590, 125473.  
1704 <https://doi.org/10.1016/j.jhydrol.2020.125473>

1705 Wu, J., Lakshmi, V., Wang, D., Lin, P., Pan, M., Cai, X., Wood, E.F., Zeng, Z., 2020. The  
1706 Reliability of Global Remote Sensing Evapotranspiration Products over Amazon. *Remote*  
1707 *Sens.* 12, 2211. <https://doi.org/10.3390/rs12142211>

1708 Yamazaki, D., Ikeshima, D., Tawatari, R., Yamaguchi, T., O’Loughlin, F., Neal, J.C., Sampson,  
1709 C.C., Kanae, S., Bates, P.D., 2017. A high-accuracy map of global terrain elevations.  
1710 *Geophys. Res. Lett.* <https://doi.org/10.1002/2017GL072874>

1711 Yamazaki, D., Kanae, S., Kim, H., Oki, T., 2011. A physically based description of floodplain  
1712 inundation dynamics in a global river routing model. *Water Resour. Res.* 47, 1–21.  
1713 <https://doi.org/10.1029/2010WR009726>

1714 Yamazaki, D., Sato, T., Kanae, S., Hirabayashi, Y., Bates, P.D., 2014. Regional flood dynamics  
1715 in a bifurcating mega delta simulated in a global river model. *Geophys. Res. Lett.* 41, 3127–  
1716 3135. <https://doi.org/10.1002/2014GL059744>

1717 Yamazaki, D., Trigg, M.A., Ikeshima, D., 2015. Development of a global ~90m water body map  
1718 using multi-temporal Landsat images. *Remote Sens. Environ.* 171, 337–351.  
1719 <https://doi.org/10.1016/j.rse.2015.10.014>

1720 Zhang, Z., Poulter, B., Fluet-Chouinard, E., Jensen, K., McDonald, K., Hugelius, G., Gumbrecht,  
1721 T., Carroll, M., Prigent, C., Bartsch, A., 2020. Development and evaluation of the global  
1722 Wetland Area and Dynamics for Methane Modeling dataset (WAD2M). *Earth Syst. Sci.*  
1723 Data in review, 1–50. <https://doi.org/10.5194/essd-2020-262>

1724 Zhou, X., Prigent, C., Yamazaki, D., 2021. Toward improved comparisons between land-  
1725 surface-water-area estimates from a global river model and satellite observations. *Water*  
1726 *Resour. Res.* 57, e2020WR029256. <https://doi.org/10.1029/2020WR029256>

1727 Zubieta, R., Getirana, A., Espinoza, J.C., Lavado, W., 2015. Impacts of satellite-based  
1728 precipitation datasets on rainfall-runoff modeling of the Western Amazon basin of Peru and  
1729 Ecuador. *J. Hydrol.* 528, 599–612. <https://doi.org/10.1016/j.jhydrol.2015.06.064>

1730 Zubieta, R., Getirana, A., Espinoza, J.C., Lavado-Casimiro, W., Aragon, L., 2017. Hydrological  
1731 modeling of the Peruvian-Ecuadorian Amazon Basin using GPM-IMERG satellite-based  
1732 precipitation dataset. *Hydrol. Earth Syst. Sci.* 21, 3543–3555. [https://doi.org/10.5194/hess-](https://doi.org/10.5194/hess-21-3543-2017)  
1733 [21-3543-2017](https://doi.org/10.5194/hess-21-3543-2017)

1734 Zubieta, R., Saavedra, M., Espinoza, J.C., Ronchail, J., Sulca, J., Drapeau, G., Martin-Vide, J.,  
1735 2019. Assessing precipitation concentration in the Amazon basin from different satellite-  
1736 based data sets. *Int. J. Climatol.* 39, 3171–3187. <https://doi.org/10.1002/joc.6009>

1737

1738

1739

1740

1741

1742 **Supplementary Material**

1743

1744 Table S1. List of additional studies that mapped inundation in the Amazon, which were not  
1745 included in the article analysis because of redundancy with the used datasets, or data unavailability.

	Reference	Dataset name / Type	Spatial. resolution	Temporal resolution	Time period	Region	Type of inundation captured
1	Aires et al. (2013)	GIEMS + downscaling with SAR	500 m	Monthly	1993-2007	Central Amazon	All
2	Belger et al. (2011)	Radarsat-1 / C-band SAR	25 m	Irregular	2004-2005	Cuini and Itu (Negro basin)	All
3	Bonnet et al. (2008)	Hydrological model		Daily	1997-2003	Curuai	All
4	Canisius et al., 2019)	Radarsat-2 / C-band SAR	2.5-2.6 m	Irregular	2014-2016	Lower Amazon river	All
5	Fleischman et al. (2020)	MGB / Hydrological-hydraulic model	4 km	Daily	1999-2015	Negro River basin	All
6	Frappart et al. (2005)	JERS-1 / L-band SAR	90 m	Static (high and low water)	1995-1996	Negro River basin	All

7	Getirana et al. (2012)	HYMAP / Hydrological model		Daily	1986–2006	Negro River basin	All
8	Guimberteau et al. (2012)	ORCHIDEE / Hydrological model	0.5 degrees	Daily	1980–2000	Basin	All
9	Hawes et al. (2012)	ALOS-PALSAR / L-band SAR	100 m	Irregular	2006–2009	Juruá floodplain	All
10	Hoch et al. (2017)	PCR-GLOBWB / Hydraulic model	30 arcmin	Daily	1985–1990	Central Amazon	All
11	Langerwisch et al. (2013)	LPJmL / Hydrological model	0.5 degrees	Monthly	1961–1990	Basin	All
12	Lauerwald et al. (2017)	ORCHIDEE-ORCHILEAK / Land surface model	0.5 degrees	Daily	1980–2000	Basin	All
13	Lesack and Melack (1995)	In situ data	-	-	-	Lake Calado	All
14	Li et al. (2020)	Landsat (Mapbiomas)	30 m	Annual	1985–2019	Madeira river close to Santo Antônio and Jirau dams	All
15	Luo et al. (2017)	MOSART / Hydraulic model	-	-	-	Basin	All
16	Martinez and Le Toan (2007)	JERS-1 / SAR	25 m	Irregular (21 images)	1993–1997	Curuai	All
17	Miguez-Macho and Fan (2012)	LEAF-Hydro-Flood / Hydrological-hydraulic model	~2 km	Daily	2000–2010	Basin	All

18	Meyer Oliveira et al. (2020)	ALOS-PALSAR / L-band SAR	100 m	Irregular	2006-2010	Purus River basin	All
19	Nardi et al. (2019)	GFPLAIN250m / geomorphic approach	250 m	Static	2002 (SRTM mission)	Basin	Floodplains
20	Paiva et al. (2013)	MGB / Hydrological-hydraulic model	500 m	Daily	1998-2010	Basin	All
21	Ringeval et al. (2012)	TOPMODEL - LSM / Hydrological model	1 degree	Monthly	1993-2004	Basin	All
22	Ringeval et al. (2014)	PCR-GLOBWB / Hydrological model	0.5 degrees	Daily	1979 - 2009	Basin	All
23	Rodriguez-Alvarez et al. (2019)	CYGNSS / GNSS-R	500 m - 7 km	Daily-14 days	2017	Pacaya-Samiria	All
24	Rosenqvist et al. (2002)	JERS-1 / L-band SAR	100 m	Irregular	1996-1997	Jau river basin	All
25	Silva et al. (2013)	Radarsat-1 / C-band SAR	25 m	Irregular	2003 - 2005	Amazon river (Juruti - Monte alegre)	All
26	Sippel et al. (1992)	RADAMBRASIL / Side-looking Airborne Radar	0.25 degrees	Monthly	1979-1987	Amazon river in Brazil	All
27	Souza et al. (2019)	Landsat	30 m	Annual	1985-2017	Brazilian Amazon	Open water
28	Trigg et al. (2009)	LISFLOOD-FP and HEC-RAS / Hydraulic models	180 m / irregular	Daily	1995-1997	Solimões River (Itapeua - Manaus)	All
29	Wilson et al. (2007)	LISFLOOD-FP / Hydraulic model	270 m	Daily	1995-1997	Solimões River (Itapeua - Manaus)	All
30	Fassoni-Andrade et al., 2019	MODIS	250 m	8-Days	2003-2017	Central Amazon	Open water

1747 Table S2. Main characteristics of the assessed wetlands.

	Name	Location	Characteristics
1	Curuai floodplain	Lower Amazon River	Shallow lakes with high suspended sediment concentrations
2	Janauacá floodplain	Middle Amazon River	Ria lake and “várzea” environments (white-water floodplains)
3	Uatumã floodplain	300-km reach between Balbina dam and the confluence with the Amazon River	Black-water floodplain
4	Mamirauá Reserve	Confluence between Solimões and Japurá rivers	Mosaic of chavascal, herbaceous, and low and high várzea vegetation
5	Purus floodplain	Purus River	Large floodplain to river width ratio
6	Pacaya-Samiria wetlands	Upper Solimões River	Flooded forests, palm swamps and peatlands
7	Llanos de Moxos floodable savannas	Upper Madeira River basin	Interfluvial areas among Beni, Mamoré and Madre de Dios rivers
8	Negro savannas	Negro-Branco interfluvial area	Regional neotectonic depressions
9	Roraima savannas	Smaller river floodplains interspersed with areas subject to flooding by local rainfall in the upper Branco River basin	Poorly drained interfluvial savannas

1748

1749 Table S3. Comparison metrics - Pearson correlation (R) and normalized root mean square error (nRMSD) for time

1750 series, and Fit metric for the spatial analysis of maximum observed inundation area for all datasets against the



1751 subregional estimates for individual wetland complexes: Curuai (Arnesen et al., 2013), Uatumã (Resende et al., 2019),  
 1752 Janauacá (Pinel et al., 2019), Mamirauá (Ferreira-Ferreira et al., 2015), Pacaya-Samiria (Jensen et al., 2020), Llanos  
 1753 de Moxos (Ovando et al., 2016) and Lower Amazon (Park et al., 2019). Four additional subregional datasets were  
 1754 compared to the local ones mentioned above: Curuai LISFLOOD-FP model (Rudorff et al., 2014), Janauacá  
 1755 hydrological model (Bonnet et al., 2017), Janauacá TELEMAC-2D model (Pinel et al., 2019), and Llanos de Moxos  
 1756 ALOS-PALSAR (Ovando et al., 2016). The Fit metric was applied by converting all maps to 1 km, considering a pixel  
 1757 with inundation fraction higher than 50% as inundated.

	Dataset	-	Curuai				Uatu mã	Janauacá			Mamira uá	Pacaya-Samiria			Llanos de Moxos			Lower Amaz on
	-	Period	2006-2010				2006- 2011	2007-2011			2007- 2010	2014-2018			2001-2014			2000- 2020
			R	nRM SD	Fit	Fit	R	nR M SD	Fit	Fit	R	nRM SD	Fit	R	nRM SD	Fit	Fit	
Other subregio nal datasets	Curuai- Model	1994- 2015	0.8 2	12%	0.8 6	-	-	-	-	-	-	-	-	-	-	-	-	
	Janauacá -Bonnet	2006- 2019	-	-	-	-	0.7 5	25 %	0.49	-	-	-	-	-	-	-	-	
	Janauacá -Pinel	2006- 2015	-	-	-	-	0.5 7	17 %	0.82	-	-	-	-	-	-	-	-	
	Llanos de Moxos - ALOS	2006- 2010	-	-	-	-	-	-	-	-	-	-	-	0.5 2	99%	0.3 3	-	
Multiple datasets at coarse resolutio n	GIEMS- 2	1992- 2015	0.9 6	21%	-	-	0.7 8	15 7%	-	-	0.8 8	68%	-	0.9 1	85%	-	-	
	SWAMP S	2000- 2020	0.9 1	2%	-	-	0.8	38 %	-	-	0.5 2	74%	-	0.9 2	171%	-	-	
	WAD2 M	2000- 2018	0.9	82%	-	-	0.7 9	63 %	-	-	0.4 6	2%	-	0.9	123%	-	-	
Multiple datasets at high	GIEMS- D3	1993- 2007	-	-	0.9 2	0.61	-	-	0.80	0.81	-	-	0.1 4	-	-	0.4 4	0.45	
	CIFOR	2011	-	-	0.9 1	0.39	-	-	0.24	0.33	-	-	0.5 5	-	-	0.3 0	0.69	

resolutio n	ESA- CCI	1992- 2015	-	-	0.7 6	0.40	-	-	0.40	0.70	-	-	0.3 6	-	-	0.1 4	0.69
	GIEMS- D15	1993- 2004	-	-	0.9 2	0.58	-	-	0.68	0.59	-	-	0.5 1	-	-	0.3 8	0.46
	GLWD	1992- 2004	-	-	0.8 8	0.45	-	-	0.79	0.93	-	-	0.6 3	-	-	0.0 8	0.51
	SWAF- HR	2010- 2019	-	-	0.9 5	0.64	-	-	0.63	0.71	0.6 6	73%	0.2 2	0.7 5	213%	0.3 9	0.57
Hydro- logical models	THMB	1961- 2013	0.7 2	62%	-	-	0.7 3	73 %	-	-	-	-	0.5 4	7%	-	-	-
	CaMa- Flood	1980- 2014	0.8 0	11%	0.9 7	0.73	0.6 8	11 1%	0.88	0.83	-	-	0.4 9	0.8 2	218%	0.2 8	0.58
	MGB	1980- 2014	0.8 3	7%	0.9 6	0.58	0.6 4	29 3%	0.82	0.93	-	-	0.5 2	0.9 1	26%	0.1 9	0.52
Optical sensors	G3WB M	1990- 2010	-	-	0.6 4	0.29	-	-	0.19	0.14	-	-	0.0 3	-	-	0.0 4	0.59
	GLAD	1999- 2018	-	-	0.8 4	0.39	-	-	0.30	0.20	-	-	0.0 4	-	-	0.1 6	0.78
	GSWO	1984- 2019	-	-	0.7 5	0.31	-	-	0.21	0.17	-	-	0.0 4	-	-	0.0 9	0.68
SAR	Hess	1995- 1996	-	-	0.9 6	0.47	-	-	0.28	0.98	-	-	0.4 8	-	-	0.4 7	0.69
	Chapma n	2006- 2011	-	-	0.6 5	0.27	-	-	0.22	0.68	-	-	0.2 8	-	-	0.2 4	0.50
	Rosenqv ist	2014- 2018	-	-	0.5 9	0.34	-	-	0.59	0.98	-	-	0.6 4	-	-	0.1 9	0.48

1758

1759 Table S4. Long-term minimum inundation areas (km<sup>2</sup>) for 11 wetland complexes (up to three datasets per complex)  
1760 and the 18 basin-scale datasets. The local-scale values refer to the following datasets, in this order (comma-separated  
1761 values relate to areas with more than one dataset available) : Curuai - ALOS (Arnesen et al., 2013) and LISFLOOD-  
1762 FP model (Rudorff et al., 2014); Uatumã - ALOS (Resende et al., 2019); Janauacá - ALOS (Pinel et al., 2019),  
1763 hydrologic model (Bonnet et al., 2017) and TELEMATAC-2D model (Pinel et al., 2019); Mamirauá - ALOS (Ferreira-  
1764 Ferreira et al., 2015); Pacaya-Samiria - ALOS-2 PALSAR-2 (Jensen et al., 2020); Llanos de Moxos - MODIS (Ovando  
1765 et al., 2016) and ALOS (Ovando et al., 2016); and lower Amazon - MODIS (Park et al., 2019). Average, standard  
1766 deviation (S.D.) and coefficient of variation (CV) are presented for each area in the last row.

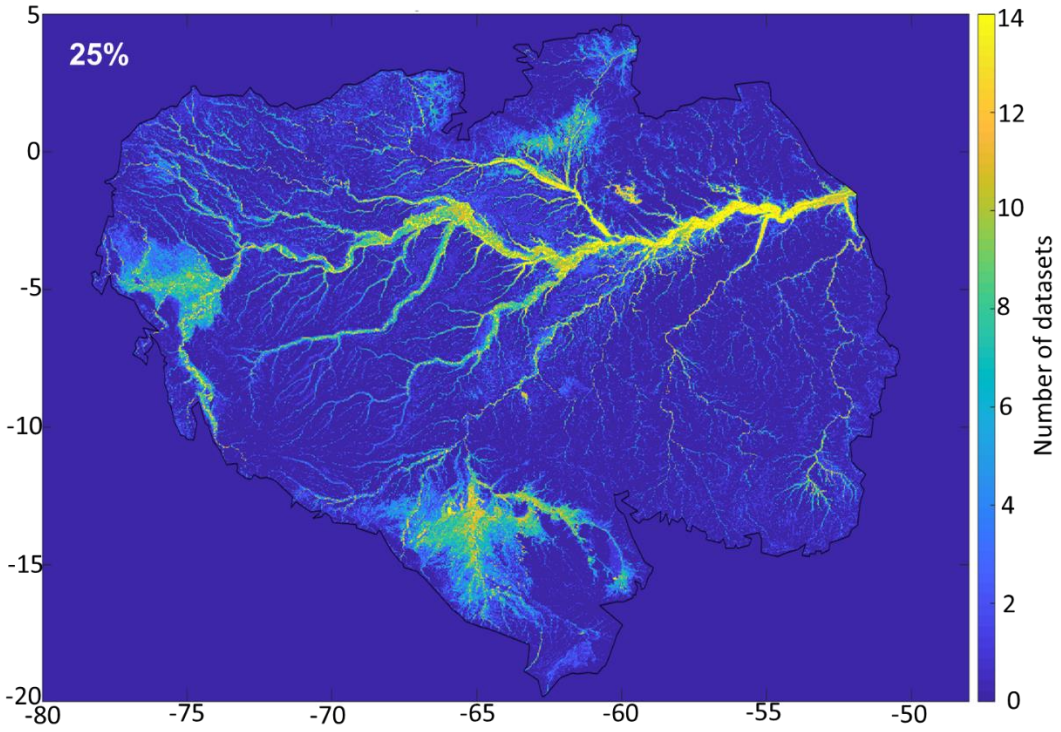
	Datas et	Curuai	Uatumã	Janauacá	Mamirauá	Pacaya-Samiria	Llanos de Moxos	Lower Amazon	Amazon mainstem	Purus	Roraima savannas	Negro savannas
	Local	1690, 1278	-	108, 38, 18	715	3824	1014, 3962	17797				
Multiple datasets at coarse resolution	GIEM S-2	995	263	183	1117	1578	500	19717	26807	349	0	0
	SWA MPS	2840	479	197	790	4433	24622	38345	53256	3492	309	6375
	WAD 2M	403	97	97	633	20421	31713	14728	29932	4240	258	10443
Multiple datasets at high resolution	GIEM S-D3	2712	861	151	1115	2731	8375	33253	44853	2696	383	146
	CIFOR	-	-	-	-	-	-	-	-	-	-	-
	ESA-CCI	-	-	-	-	-	-	-	-	-	-	-
	GIEM S-D15	3942	1265	116	1077	3409	15074	44277	59066	3401	2966	2622
	GLWD	-	-	-	-	-	-	-	-	-	-	-
	SWA F-HR	1502	544	69	469	215	8304	20944	30242	784	0	3
Hydrological model	THMB	487	38	1	266	5349	7172	6708	18099	5596	383	195
	CaMa - Flood	2741	861	184	1135	8269	17776	31569	45848	4128	1001	672
	MGB	3005	212	0	587	6101	4508	21333	32073	1769	226	35
Optical sensors	G3W BM	-	-	-	-	-	-	-	-	-	-	-
	GLAD	474	77	8	288	514	1513	6243	9857	335	13	20
	GSWO	736	345	10	314	401	2934	11908	16428	735	117	2
Synthetic Aperture Radar	Hess	2770	584	106	1756	32107	56337	28981	54493	7061	1217	6084
	Chapman	1894	385	68	866	6775	10090	18413	28539	2951	1025	2843
	Rosenqvist	1514	313	49	422	1077	4566	13413	19512	575	60	5
	Average	1858	452	89	774	6670	13820	22131	33500	2722	568	2103
	S.D.	1148	350	71	430	8978	15190	11637	15551	2094	801	3285
	CV	0.62	0.77	0.80	0.56	1.35	1.10	0.53	0.46	0.77	1.41	1.56

1768

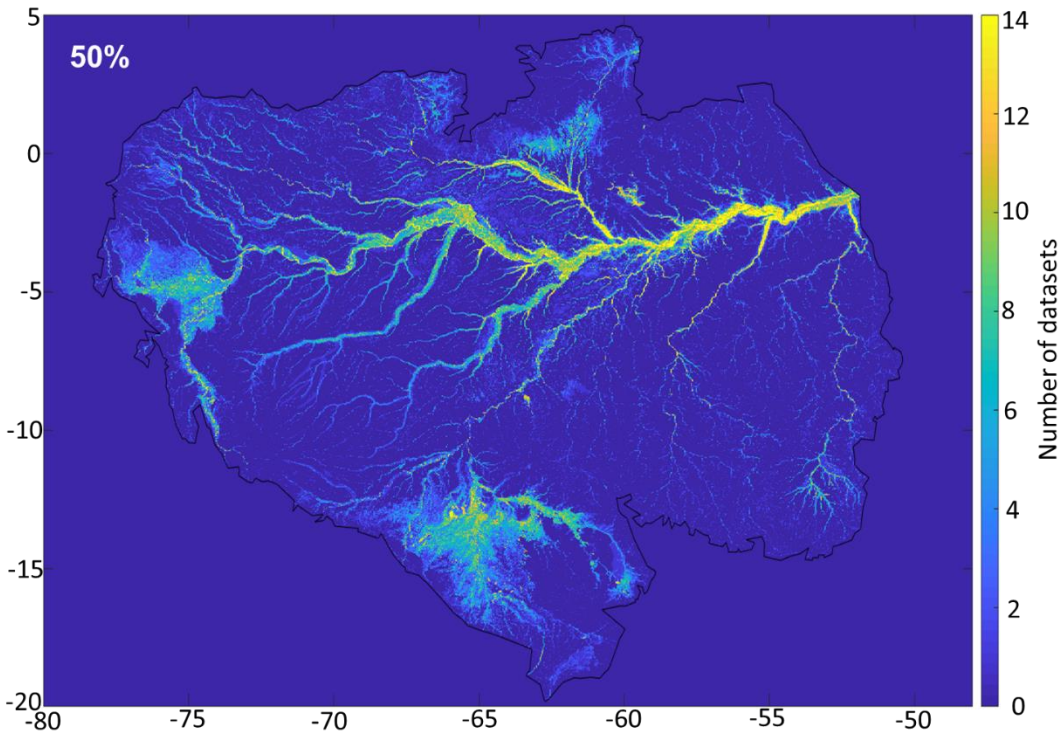
1769

1770

1771



1772

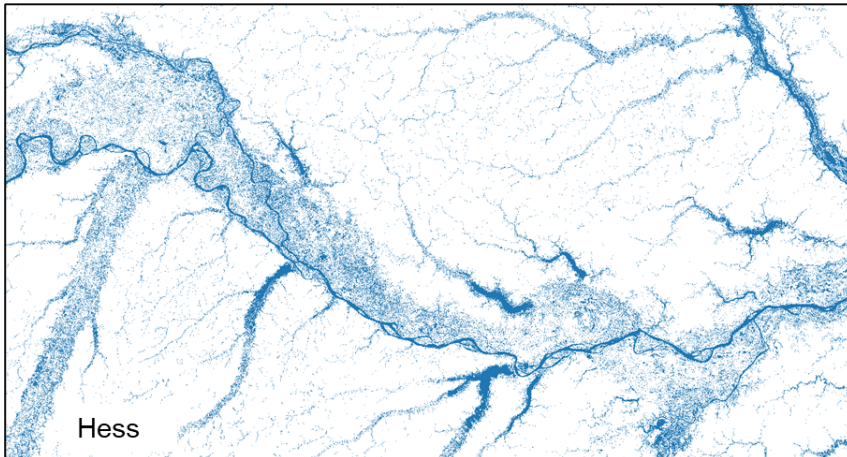
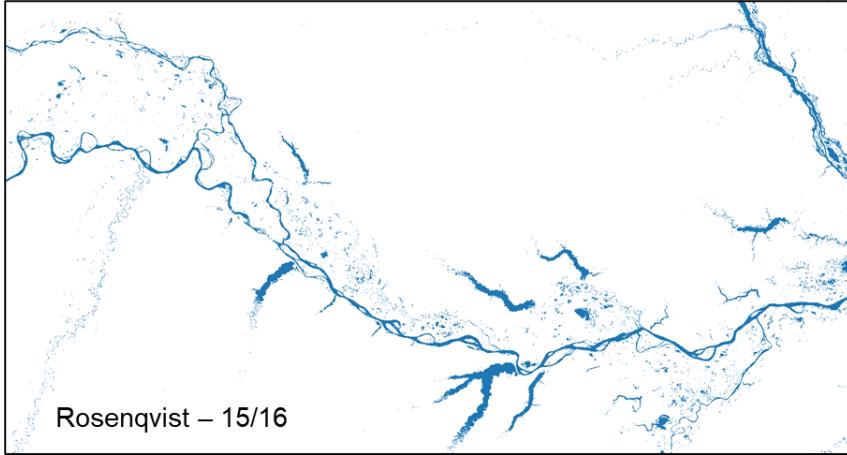


1773

1774 Figure S1. Sensitivity of the fraction used to define a flooded 1km pixel (25% and 50%).

1775

1776



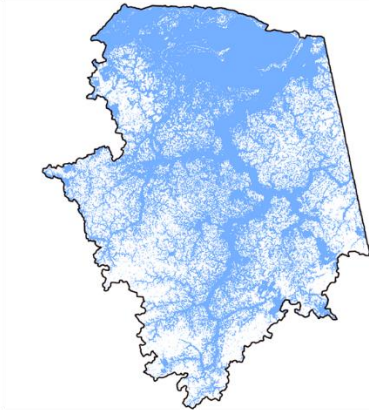
1777

1778 Figure S2. Minimum inundation extent for the central Amazon River, as estimated by the

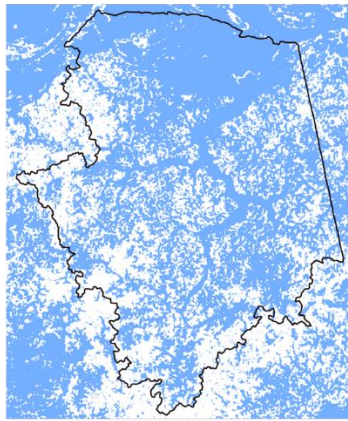
1779 Rosenqvist (years 2015-2016) and Hess (1995) datasets.

1780

(A) Janauacá



Pinel et al. (2019) – 30 m

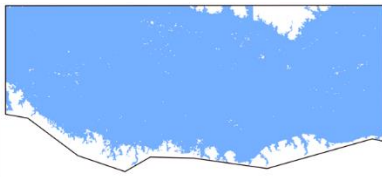


Rosenqvist et al. (2020) – 50 m

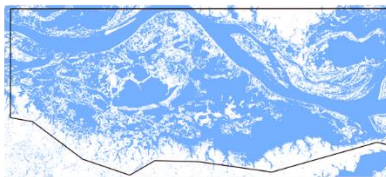


Hess et al. (2015) – 90 m

(B) Curuai



Arnesen et al. (2013) – 12.5 m



Rosenqvist et al. (2020) – 50 m



Hess et al. (2015) – 90 m

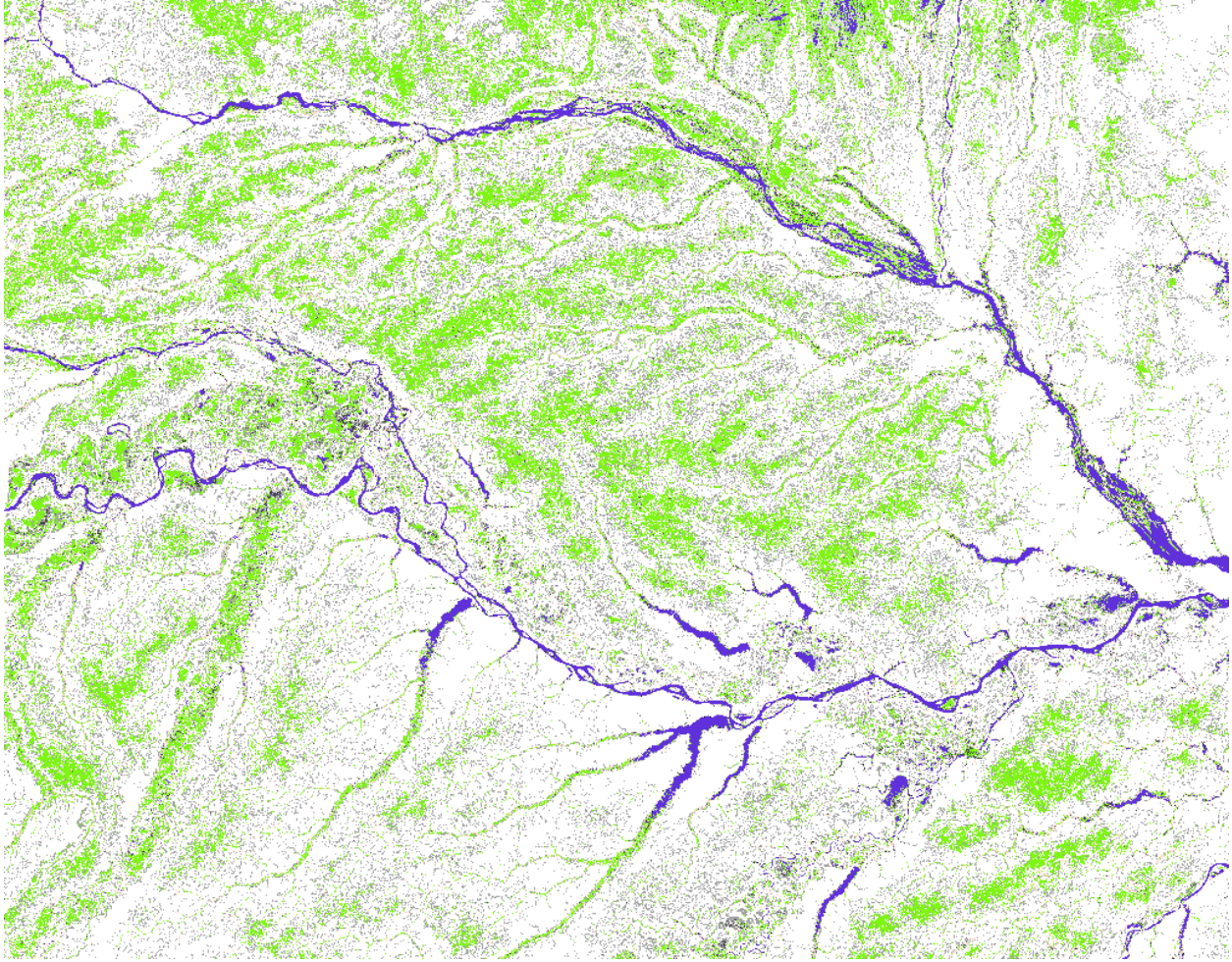
1781

1782 Figure S3. Comparison between the long-term maximum inundation for subregional validation

1783 locations (Pinel and Arnesen datasets) as well as the Rosenqvist and Hess datasets for the (a)

1784 Janauacá and (b) Curuai areas. The polygons refer to the area used to extract the values presented

1785 in Tables 3, S3 and S4. The spatial resolution of each dataset is noted.

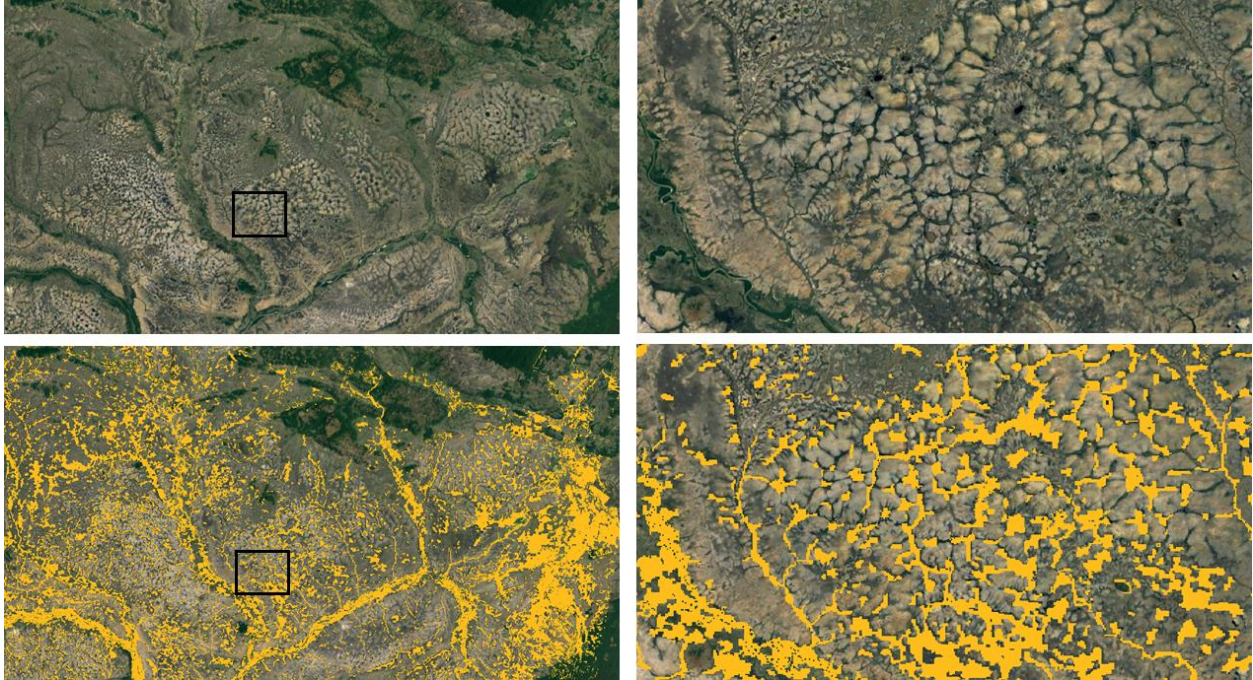


1786

1787 Figure S4. Estimation of wetland areas by Gumbrecht et al. (2017) across the central Amazon River  
1788 basin. Green pixels relate to the “swamps (incl. bogs)” category, which is defined as “Wet all year  
1789 around, but not necessarily inundated.”

1790

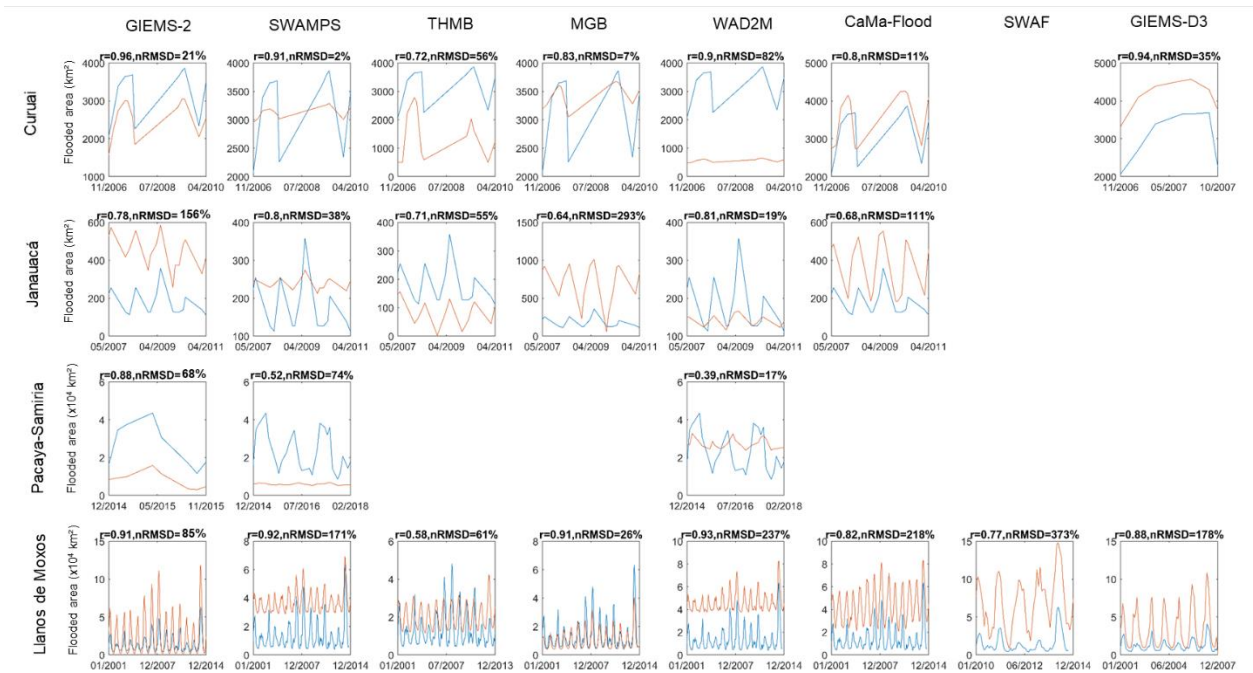




1791

1792 Fig S5. Roraima wetlands. Above: Google Earth imagery. Below: Hess SAR classification of  
 1793 floodable areas (at large scale in the left, and detailed scale in the right), displayed as orange areas.

1794



1795

1796 Fig S6. Inundation time series for the four wetlands with available datasets, and for the eight basin-  
1797 scale dynamic datasets (GIEMS-2, SWAMPS, THMB, MGB, WAD2M, CaMa-Flood, SWAF-HR  
1798 and GIEMS-D3). The subplots that are empty refer to areas where the basin-scale dataset time  
1799 spans did not overlap with the subregional dataset ones. The subregional dataset is displayed in  
1800 blue, and each of the basin-scale datasets in red.